2017

Numerical Study of the Periodic Anderson Model with Holstein Phonons for the Description of Cerium Volume Collapse

Enzhi Li
Louisiana State University and Agricultural and Mechanical College, enzhililsu@gmail.com

NUMERICAL STUDY OF THE PERIODIC ANDERSON MODEL WITH HOLSTEIN PHONONS FOR THE DESCRIPTION OF CERIUM VOLUME COLLAPSE

A Dissertation

Submitted to the Graduate Faculty of the
Louisiana State University and
Agricultural and Mechanical College
in partial fulfillment of the
requirements for the degree of
Doctor of Philosophy

in

The Department of Physics and Astronomy

by
Enzhi Li
B.Sc., Nanjing University of Aeronautics and Astronautics, 2009
August, 2017

Acknowledgements

I want to thank Professor Juana Moreno and Professor Mark Jarrell for their guidance during my study. Without their support and help, I cannot possibly finish my thesis. I also want to thank Ka-Ming Tam, Shuxiang Yang, Yi Zhang, and Peng Zhang for their help during my study. They are always there to help me whenever I encounter a problem, whether be it a problem in physics, in programming, or in computer. I especially thank Professor Rongying Jin and Professor Ilya Vekhter for kindly proofreading my thesis, and giving me several advices for modification. I also thank my friends here, which include but are not limited to Mengxi Wu, Liuli Huang, Jianping Lai, Zhenyu Diao, Yun Ding, Sheng Feng, Ye Fang and so on, for their help in both my curriculum and life. Last, but not least, I want to pay a special tribute to Mengxi Wu and Liuli Huang for their saving my life in a car accident.

This material is based upon work supported by the National Science Foundation under the NSF EPSCoR Cooperative Agreement No. EPS-1003897 with additional support from the Louisiana Board of Regents. Computer support is provided by the Louisiana Optical Network Initiative, and by HPC@LSU computing.

Table of Contents

Abstract

The volume collapse transition of Cerium has intrigued physicists since its discovery several decades ago. Various models and mechanisms have been proposed, the most prominent scenarios are based on the Mott transition and the Kondo volume collapse transition. In this study, we explore the volume collapse by a dynamical mean field theory (DMFT) study of the periodic Anderson model with electron-phonon coupling to the conduction band. This allows us to study the effect of the electron-phonon interaction on the volume collapse. In order to faithfully account for the volume collapse, we also include the effects due to the volume and temperature dependent bulk modulus. We find that as the electron-phonon interaction strength increases, the volume collapse effect is enhanced, which is consistent with the suggestion that the phonons have an important contribution in the volume collapse transition. Although we start with the canonical model for the Kondo volume collapse scenario, our results have some of the characteristics of the Mott scenario. For example, when we plot the conduction electron density of states, we find that when the electron-phonon interaction effect dominates over the Kondo effect in this system, the conduction band electron spectra develops a Mott gap at the Fermi energy. Moreover, the width of the gap is proportional to the effective electron-phonon interaction strength. Currently, we cannot determine the order of this Mott transition, however, we conjecture that the transition is continuous due to the fact that the phonon frequency in our model is pretty small, and the fact that the conduction electron is doped away from half filling, both of which tend to suppress a first order phase transition. The study of the two-particle quantities, such as the charge susceptibility and the magnetic susceptibility also reveals several interesting features of the system. From the behavior of the charge and magnetic susceptibilities and the electronic spectral functions, we can clearly see the competition between the electron-phonon interaction and the Kondo effect due to the hybridization between conduction electrons and localized impurity electrons.

Chapter 1

Introduction

1.1 A brief history of the strong correlation puzzle

Since the discovery of the static electricity in the 18th century, people already noticed the existence of metals and insulators, a topic that is still intriguing condensed matter physicists today. In the early 19th century, Pierre-Louis Dulong and Alexis-Thrse Petit discovered that the specific heats of various solids seem to have the same constant value. By invoking the classical statistical mechanics that he created, Boltzmann gave a theoretical explanation of this universal behavior in the late 19th century[1]. All of these are attempts to understand the properties of solids from a classical perspective. Nowadays, we know that the solids are intrinsically quantum, and thus a quantum theory of solids is required to fully understand the electronic properties of materials.

The study of condensed matter systems with the employment of the principles of quantum mechanics starts from Sommerfeld's electron gas theory[2] in the early 20th century. Using the newly developed theory of quantum mechanics and Fermi-Dirac statistics, Sommerfeld was able to derive the properties of solids that are consistent with the wave-particle duality and Pauli's exclusion principle. Although this theory was cited as the first attempt to study the solids from the quantum perspective and generated some surprisingly good theoretical results that are in agreement with experiments, it still made the unphysical prediction that all solids are metals due to its ignorance of the crystal structures.

The influence of the crystal structure on the electronic properties of solids was captured by Bloch's theory[2, 3]. Using the periodic boundary condition and the assumption of the translational symmetry of the solids, Bloch was able to derive the Bloch wave function from which the band structure of the solids can be calculated. Compared to Sommerfeld's theory which predicts that all solids are metals, Bloch's theory makes a remarkable progress in the study of solids in that it can explain the existence of the metals and insulators. Bloch originally wished to use his theory to understand the mechanism of superconductivity which was discovered in 1911 by Onnes[4]. With

hindsight, we know that this theory is not enough for an explanation of superconductivity since it did not take into account the correlations between electrons and the interactions between electrons and the lattice vibrations, which were later proved to be the critical components for the emergence of superconductivity.

The discovery of the superconductivity is a groundbreaking feat in the history of physics. Its existence puzzled the community of the physics for decades. The most prominent minds in the field of physics dedicated their attention to an explanation of this esoteric phenomenon, and no significant progress was made since its discovery in 1911 until Fröhlich[5] proposed a model that considers the electron-phonon interaction as the driving mechanism for superconductivity. A mean field theory of superconductivity was given by Bardeen, Cooper, and Schrieffer in 1957[6], and a complete microscopic theory that takes fully into account the many body effects was proposed by the Russian physicists such as Migdal, Eliashberg, etc[7]. The theoretical study of superconductivity is a milestone in the field of condensed matter physics and marks a sharp departure from the old quantum solid theory in that it signifies to the physics community the importance of the electron correlations in the study of condensed matter systems. Both Sommerfeld's theory and Bloch's theory are single particle approximations, and they are far from complete for the description of the real systems. It is the strong correlations between the electrons that give rise to the interesting physics that we observe in the world.

Another equally important line of thought that emphasizes the importance of electronic correlations is the Mott metal-insulator transition[8]. Mott insulator is a special kind of insulator that should have been a metal according to the non-interacting Bloch's theory. A theoretical model for understanding the Mott metal-insulator transition was given by Hubbard in 1963[9] which we now call the Hubbard model. Hubbard model is the simplest model that captures the essence of the competition between the delocalization of band electrons due to hopping from one site to its nearest neighbors and the Coulomb repulsion of electrons of opposite spins that reside on the same lattice site. This model, although simple, resists all possible theoretical attacks except in one dimensional case[10, 11]. The desire to understand the details of this model in a non-trivial limit has triggered the development of the dynamical mean field theory[12–15], a topic to which we will return later.

Since the end of the WWII, perturbation theory and Feynman diagrams have been widely used to study the electromagnetic interactions. Later, physicists introduced this powerful technique into the regime of condensed matter[7], and applied this theory successfully to the study of the low temperature superconductivity. The widely celebrated Migdal-Eliashberg theory is a notable

achievement in this field. However, it turned out that when the correlations are strong enough, the perturbation theory proved to be inapplicable due to the absence of a small expansion parameter. For example, Kondo's explanation of the resistance minimum of a metal with dilute magnetic impurities as a function of temperature depends on the calculation of perturbation series to third order[16], which is a *tour de force* in the history of physics. However, this theory also made the unphysical prediction that the resistance will grow to a logarithmic infinity when the temperature approaches 0. The reason for this unphysical prediction is that the perturbation theory fails when the temperature drops below the Kondo temperature T_K[17], and in the low temperature regime, non-perturbative schemes are required to understand the physical behavior of the electrons. The first attempt to understand the low temperature physics of the Kondo model was taken in 1970 by Anderson[18] whose formulation of the scaling theory for the Kondo problem predates the work on numerical renormalization group by Wilson[19]. Wilson later developed the idea of the scaling theory to its full extent and formulated a thorough theory of numerical renormalization group that completely solved the Kondo problem[20]. The numerical renormalization group method was later applied to the Anderson model[21], and became a standard technique for solving the strong correlation puzzle (especially the single impurity problem) in condensed matter physics. The extension of this method to one dimensional case is accomplished by the density matrix renormalization group method[22] which is still seeing strident progress up to now.

The dynamical mean field theory (DMFT)[12–15] is another non-perturbative method that provides us with exact solutions of strongly interacting models in a non-trivial limit. The DMFT is a quantum extension of the classical mean field theory which ignores the spatial correlations and becomes exact in the infinite dimensional limit. In spite of the restriction that the DMFT is exact only at infinite dimensions which seems to be far away from the real world, the DMFT made remarkably accurate predictions for even two and three dimensional systems. With the help of the DMFT, we now have numerically exact solutions of the Hubbard model[15, 23–25], the Falicov-Kimball model[26], the Holstein model[27], the periodic Anderson model[28, 29], etc. The existence of the exact solutions to these models is unthinkable before the invention of the DMFT which can thus be acclaimed as a great victory over the strong correlation puzzle in recent decades. An extension of the DMFT that incorporates the short range spatial correlations is given by the dynamical cluster approximation. For a review of this extended theory and its comparison with DMFT, see Ref. [30].

In the DMFT, we map the original lattice model into a single impurity Anderson model and then use the iteration cycle that was first proposed in Ref. [15] to obtain a convergent solution.

The application of the iteration cycle depends critically on the impurity solver that solves the single impurity problem to which our original model is mapped. There are many kinds of impurity solvers, such as the numerical renormalization group as discussed above, the exact diagonalization technique[31], and the quantum Monte Carlo(QMC) method. The advantage of the numerical renormalization group method is that it gives results of high accuracy and works at zero temperature, a temperature that is not reachable using QMC. Numerical renormalization group can also deal with finite temperature physics, however, the temperatures in this method can only take some discrete values[32]. Thus, for the finite temperature case, we will generally use the QMC method. The exact diagonalization method works for both zero temperature and finite temperature, but the exponential growth of the complexity restricts its use in many systems. In our work, we have used the QMC as our impurity solver.

There are several versions of the QMC, of which the most widely used ones are the Hirsch-Fye algorithm[33], the hybridization expansion QMC[34], and the weak coupling expansion QMC[35, 36]. What we use in our program is the weak coupling continuous time quantum Monte Carlo, a brief review of which is given in Chapter 3. The details of this method can be found in Ref. [36] and will not be reproduced here.

In the QMC simulation, we can only obtain numerical data in imaginary time space. With a Fourier transformation, we can further obtain the imaginary frequency results. However, in real world experiments, we can only measure the real frequency quantities, such as the spectral function. One of the reasons that people prefer to use the numerical renormalization group method is that they can directly obtain the real frequency information with this method. Fortunately, with the help of the maximum entropy (maxEnt) method [37], we can equally well extract the real frequency information from Monte Carlo simulation data. The maxEnt method is a powerful technique that was initially used in image processing in astronomy, and was later introduced into the realm of condensed matter physics to extract the real frequency information from imaginary frequency data that are invariably contaminated by all kinds of numerical noises. Based on the Bayesian inference, the maxEnt method can yield the best possible guess from incomplete information. This is a very ingenious method that has some spirit of the artificial intelligence in it. Because of this, the maxEnt method is also widely used in such areas as computer graphics, finance, big data science, and the natural langue processing. A brief review of the maxEnt method is given in Chapter 3 and in the Appendix B. For a detailed review of this method, see Ref. [37].

All the numerical methods mentioned above are nowadays indispensable tools to study the strongly correlated transition metals and the heavy-fermion materials, and have already constituted the basic arsenals of any condensed matter physicist. For example, it is known that the electronic properties of V_2O_3 can be well described by the Hubbard model[38]. Another example is the rare-earth or actinide elements that can be qualitatively and sometimes even quantitatively described by the periodic Anderson model[29]. Generally, interesting physics, such as the metal-insulator transition and heavy-fermion behavior, occurs in the parameter regime where the electron-electron interaction strength is comparable to or larger than the conduction band hopping amplitude, thus rendering the conventional perturbation schemes inapplicable. In this case, the non-perturbative methods developed in the last few decades came to our rescue. One example of these interesting physical phenomena that requires these advanced numerical techniques is the volume collapse as observed in the transition metals. Among the transition metals that display a volume collapse under pressure, cerium proves to be an outstanding example in two aspects. One is that the volume collapse of cerium is unexpectedly large, and another is that the cerium has only one $4f$ electron which makes it a paradigm for the successful explanation of esoteric physical phenomena using a simplified strong correlation model. The explanation of the cerium volume collapse is the major focus of this thesis work, and in the next section, I will give a brief summary of its history.

1.2 Brief summary of the experimental results of the Cerium volume collapse

The Cerium volume collapse has been a long standing puzzle. It was observed experimentally long time ago that Cerium under pressure can experience a sharp drop in the volume. A detailed phase diagram of Cerium is shown in Fig. 2.1. From the phase diagram, we see the separation of the two

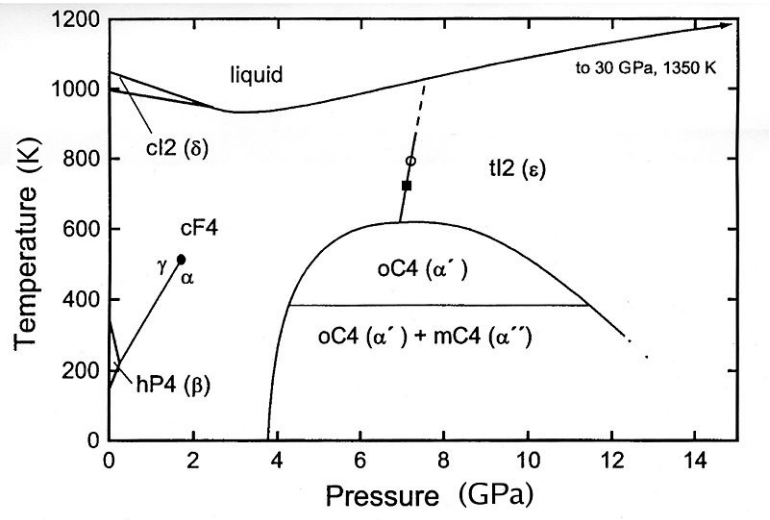

Figure 1.1: Cerium phase diagram. Picture taken from Ref. [39]. The first order transition line between γ phase and the α phase has a terminus at high pressure and high temperature.

phases, γ and α, at the lower-left corner. For a fixed temperature T that lies between approximately 180K and 500K, as the external pressure increases, Cerium metal experiences a transition from γ phase to α phase. On the other hand, when the pressure lies between 0 and 2 GPa, as we lower the temperature, the Cerium metal also experiences a transition from γ to α phase. This phase transition, called the $\gamma \rightarrow \alpha$ phase transition, is interesting in that there is a sharp volume difference between the large volume γ phase and the small volume α phase. Moreover, as can be seen from the phase diagram, the first order phase transition line that separates the γ phase from the α phase ends at a critical point, making it a solid-solid transition that exhibits a critical behavior, in analogy to the vapor-liquid transition in water.

In 1931 in the book *Physics of high pressures* , P. W. Bridgman described quantitatively the amazingly 16.5% volume collapse of Cerium at 15,000 atmospheres. In 1949, A.W. Lawson and Ting-Yuan Tang made further investigation of this phenomenon, and discovered that before and after the volume collapse, the crystal structure of Cerium remains invariant, being always face-center cubic[40]. In 1951, Parkinson *et al* measured the atomic heats of the rare-earth elements including Cerium[41], and found that the atomic heats of Cerium metal exhibit anomalous behavior. The authors conjectured that this anomaly is due to the transition of the $4f$ electron to the $5d$ state. Obviously, the authors made this deduction based on the then prevalent explanation of the Cerium volume collapse, an explanation that we now call the promotional model. According to this model, the $4f$ electrons of Cerium gets promoted to the $5d$ state under pressure, and this promotion is the origin of the volume collapse observed in Cerium. Although this model was later

refuted experimentally due to the absence of significant change in the $4f$ electron filling number, it motivated people to focus their attention on the behavior of the $4f$ electrons, which are now widely believed to be responsible for the volume collapse transition.

The $4f$ electrons, which have a significant influence on the Cerium volume collapse, are closely associated with the magnetic properties of Cerium. Thus, if the behavior of the $4f$ electrons changes across the volume collapse transition, then the magnetic susceptibility of Cerium should change accordingly. Trombe and Foex found that the magnetic susceptibility decreases when the Cerium volume collapses[42]. In 1957, J.M. Lock measured the magnetic susceptibilities of various metals, including Cerium, as a function of temperature from room temperature down to 1.5K at atmospherical pressure[43]. With these thermodynamic parameters, we know from the previous experimental results that Cerium is in the γ phase. Lock found that the magnetic susceptibility of the γ phase Cerium obeys the Curie-Weiss law, which, combined with the fact that $4f$ electrons are responsible for the magnetic behavior of Cerium, indicates the existence of local moments due to $4f$ electrons in this phase[44].

The measurement of the magnetic susceptibility of the α phase Cerium is more difficult due to the fact that we need to be able to measure small paramagnetic susceptibility under tremendous external pressure to obtain data in this phase. In 1971, M. R. MacPherson *et al* managed to measure the magnetic susceptibility of α Cerium, and showed definitely that there are no local moments in the α phase based on the observation that the magnetic susceptibility in this phase staturates to a constant as $T \to 0$, which is a hallmark of the Pauli paramagnet[45]. The authors also obtained the susceptibility versus pressure curve for Cerium at room temperature, which is reproduced in Fig. 1.2. From the figure, we see that when the external pressure increases, the magnetic susceptibility χ decreases. A sharp drop in χ is clearly seen around $p = 7.6 \times 10^3$ bar, which is the critical pressure for the $\gamma \to \alpha$ transition of Cerium at room temperature. The hysteresis loop in the $\chi - p$ plane means that the transition is first order at room temperature, which is consistent with the previous experiments. The magnetic susceptibility of the γ phase (low pressure) is much larger than that in the α phase (high pressure).

The existence of local moments in the γ phase and its absence in the α phase can be interpreted either through the Mott transition scenario[46] or the Kondo volume collapse (KVC) scenario[47]. In the Mott transition scenario, the $4f$ electrons are localized in the γ phase, giving rise to the local moments. As the volume collapses, the decrease in the lattice constant induces increase in the $4f$ electron hopping amplitude t. Furthermore, the on-site Coulomb repulsion U between $4f$ electrons

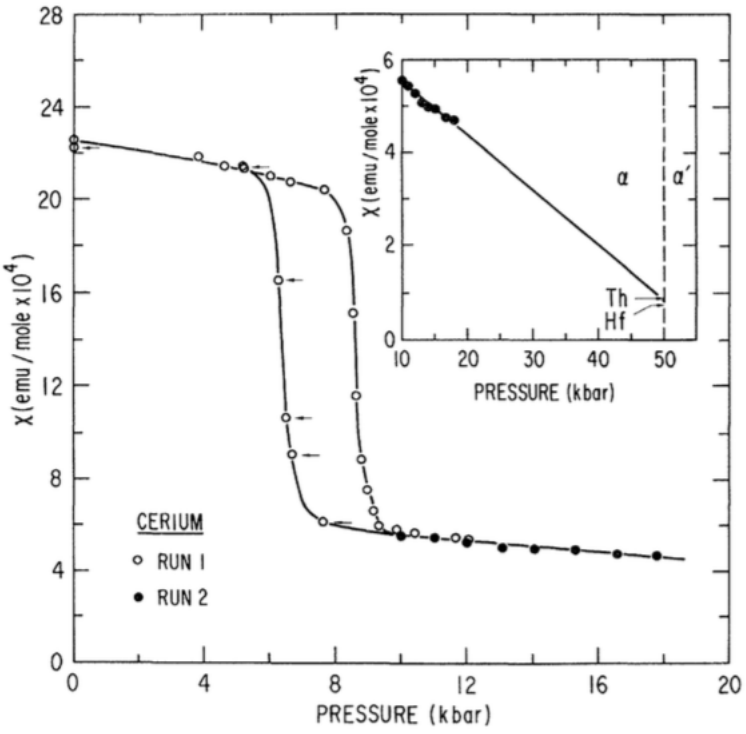

Figure 1.2: Picture from Ref. [45]. Main panel: Magnetic susceptibility χ versus pressure p for Cerium at room temperature. From the figure, we see that the susceptibility drops sharply around $p = 7.6$ K bar, which is the critical pressure for the $\gamma \to \alpha$ transition at room temperature. The hysteresis loop indicates that the transition is first order. Inset: the $\chi - p$ diagram in the α phase extrapolated to $p = 50$K bar.

of opposite spins is assumed to be constant. Thus, the net increase in the ratio t/U drives the localized $4f$ electrons in the γ phase to become delocalized in the α phase. This picture is identical to the one that was proposed by Mott in 1949[8] for the explanation of the metal-insulator transition in some materials, and thus this scenario is called the Mott transition scenario. In the KVC scenario, it is assumed that there is a Kondo coupling between the $5d$ and $6s$ conduction electrons and the localized $4f$ electrons in the Cerium. The Kondo exchange constant J between the localized $4f$ electrons and the conduction electrons is weak in the large volume γ phase, and becomes strong in the small volume α phase. This variation of the Kondo exchange constant with respect to the volume causes change in the electronic free energy which can provide the energy gain that is required for the emergence of the volume collapse in Cerium. Both scenarios can explain some aspects of the experimental results, such as the magnetic susceptibility behavior and the spectral data, and thus we have no strong preference to either scenario.

As noted above, the $\gamma \rightarrow \alpha$ transition is established to be a first order phase transition at room temperature. This first order nature of the phase transition can also be seen from the hysteresis loop in the resistivity versus temperature plane as shown in Ref. [48]. In 1958, Ponyatovskii discovered that the latent heat of the $\gamma \rightarrow \alpha$ transition decreases as the temperature increases, indicating the suppression of the first order phase transition by temperature[49]. Later, in 1960, R.I. Beecroft and C.A. Swenson measured the iso-thermal volume-pressure curves for Cerium, as reproduced in Fig. 1.3[49]. From the figure, we can see that the slope of the volume-pressure curve around the transition region becomes less steep as the temperature increases, indicating the gradual disappearance of the first order $\gamma \rightarrow \alpha$ transition. The gradual evolution of the volume-pressure curves is analogous to the iso-thermal pressure-volume diagrams of the real gas. In the case of real gas, we know that the first order vapor-liquid transition at low temperature ends at a critical point where the difference between water and vapor disappears. Thus, we may also conjecture from Fig. 1.3 that the first order $\gamma \rightarrow \alpha$ transition may disappear when the temperature is above some critical value T_c.

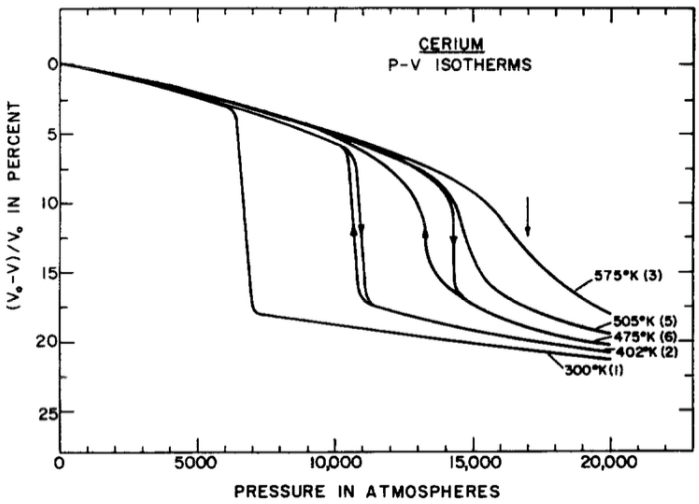

Figure 1.3: Picture from Ref. [49]. The volume versus pressure diagrams of Cerium at different temperatures. When the temperature is low (300K), the volume drops sharply at the critical pressure. As the temperature increases, the slope at the transition region becomes less steep. When the temperature is high enough, the volume-pressure curve becomes smooth, and the first order phase transition observed at low temperature may disappear.

In the 1980s, people were able to obtain material electron spectra data with unprecedented accuracy, and significant insight was gained in the nature of the $\gamma \rightarrow \alpha$ transition. Spectral techniques, such as Bremsstrahlung Isochromat Spectroscopy (BIS), and X-ray photoelectron spectroscopy (XPS) render it possible to make direct measurements of the $4f$ electron occupation n_f

and the f-conduction coupling in γ and α Cerium[50]. These two spectral techniques depend on the photo-electric effect, and can only measure the surface properties of the bulk materials(within approximately 20Å of the surface). In BIS, the material is exposed to a beam of incident electrons, which would occupy the empty high-energy states in the material and then experience a decay to low-energy states while emitting photons of various frequencies. By measuring the intensity of the emitted photons of certain frequency as a function of the incident electron energy, we can get a spectral curve which reflects the shape of the surface electron density of states (DOS) of the material. Therefore, the BIS is an electron-in-photon-out technique that measures the material surface DOS above the Fermi energy. On the other hand, the XPS is a photon-in-electron-out technique that measures the surface electron DOS below the Fermi energy, making it a complement to the BIS. In the XPS, a beam of X-ray of well defined frequency is irradiated toward the material surface, ejecting photoelectrons the energies of which depend on the difference between the incident X-ray photon energy and the binding energy of the material. Through this technique, the unknown binding energy of the surface electrons can be calculated by subtracting the photoelectron energy from the X-ray photon energy, with a possibly constant adjustment parameter. By plotting the counting of the photoelectrons as a function of the binding energy, we can obtain a spectral curve that reflects the DOS of the surface electrons below the Fermi energy. Combination of these two techniques yields an overview of the electron DOS in materials, and enables E. Wuilloud *et al* to conclude that the Cerium $\gamma \rightarrow \alpha$ transition is driven by the abrupt change in the f-conduction coupling parameter, rather than by the promotion of the $4f$ electrons to the $5d$ band[50]. The promotional model is refuted by this experiment because of the smallness of the variation ($\approx$15%) in the $4f$ filling number across the transition. This result consigns to obliteration the promotional model, and establishes the Mott transition scenario and the Kondo volume collapse scenario as the standard models for understanding the Cerium volume collapse.

The electron-phonon interaction is believed to have played an important role in the $\gamma \rightarrow \alpha$ transition. In 2003, Manley *et al* employed the inelastic neutron scattering to measure the phonon density of states (DOS) of Cerium[51], and found that in the α phase, the phonon DOS has a strong temperature dependence. However, the phonon DOS does not change noticeably across the $\gamma \rightarrow \alpha$ transition. With hindsight, we know that this is probably because the authors are actually measuring the properties of $Ce_{0.9}Th_{0.1}$ samples rather than pure Cerium. In 2004, Jeong *et al* measured the Debye temperatures of the γ and α phase Cerium using the neutron diffraction method. The Debye temperature is obtained from the slope of the thermal displacement versus temperature curve, as

shown in Fig. 1.4. Using this method, the authors found that the Debye temperature in the γ phase

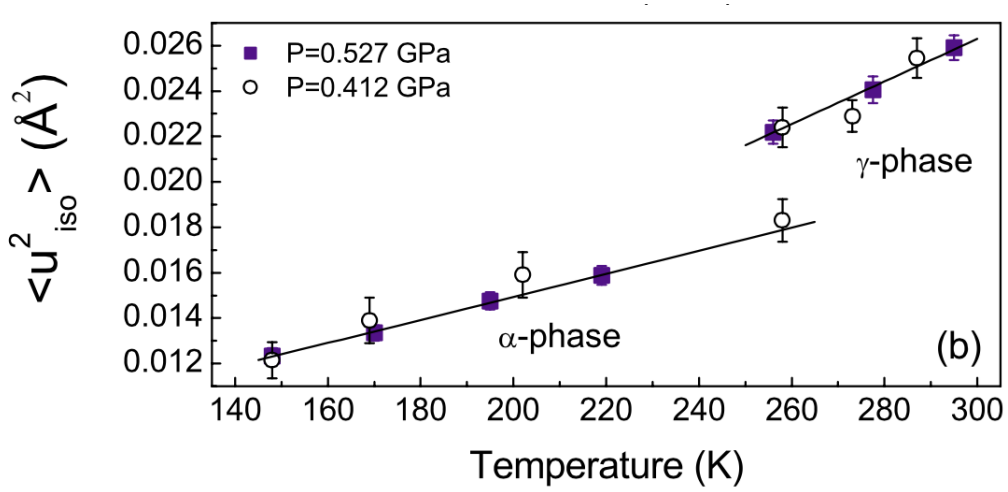

Figure 1.4: Picture from Ref. [52]. The squared thermal displacements versus temperature at constant pressure. The Debye temperature is obtained from the slope of the curve. According to Ref. [52], the Debye temperature in the γ phase is 104K, and is 133K in the α phase.

(104K) is smaller than that in the α phase (133K). With the employment of the Debye model for the evaluation of the entropy, the authors were able to estimate that the phonon entropy accounts for approximately 1/2 of the total entropy change in the volume collapse[52]. In Ref. [53], the authors measured the Debye temperatures of the γ and α Cerium using the ultrasonic method, and obtained different results(132.8 K in the γ phase and 142.9K in the α phase). Although the exact values of the phonon entropy vary between different measurements, the authors have a consensus about the importance of the electron-phonon interaction. In 2011, Krisch *et al* measured the phonon dispersion across the $\gamma \rightarrow \alpha$ transition, and found significant modification of the shapes of the phonon dispersion relations[54]. All of these results provide compelling evidence for the critical role played by phonons in the Cerium volume collapse transition, and motivate us to introduce the electron-phonon correlations in our model Hamiltonian.

Chapter 2

Cerium Volume Collapse

The experimental observation of the iso-structural cerium volume collapse in 1949 by Lawson and Tang[40] is remarkable in that it is a first-order transition from one solid phase to another. Moreover, both the solid phases possess face-center cubic (fcc) structure. This phase transition, called the $\gamma \rightarrow \alpha$ transition, is the transition from the large-volume γ phase to the small-volume α phase. The volume difference between the γ and the α is approximately 17% at room temperature, and thus this transition is called the "volume collapse". This phenomenon has puzzled the physicists for decades, and several models have been proposed to explain its occurrence. Up to now, two widely accepted scenarios survive, which are the Mott transition scenario and the Kondo volume collapse (KVC) scenario. Recently, the role of the lattice vibrations has been noted by several groups. In this chapter, we are going to present the experimental results of the cerium phase diagram, explain in detail two widely accepted and studied scenarios for the volume collapse, and review the importance of the lattice degrees of freedom during the volume collapse process. Finally, we will give a tabular form for the experimental values of the parameters that will be used throughout our work.

2.1 Experimental results of cerium volume collapse

A complete phase diagram of cerium is given in Ref. [39]. The phase diagram is shown in Fig. 2.1. From the lower-left corner of the figure, we see that there is a γ phase and an α phase that are separated from each other by a first order phase transition line which ends at a critical point. This is the $\gamma \rightarrow \alpha$ to which we will dedicate our effort throughout this thesis. The pressure-volume $(p - \mathcal{V})$ relation is given in Fig. 2.2. The picture is taken from cerium_pressure_volume_diagram. We will show in later chapters that using our model, we can reproduce the qualitative features of the cerium $p - \mathcal{V}$ diagram. The hallmark feature of the $p - \mathcal{V}$ diagram is the kink structure that indicates the existence of a first order phase transition.

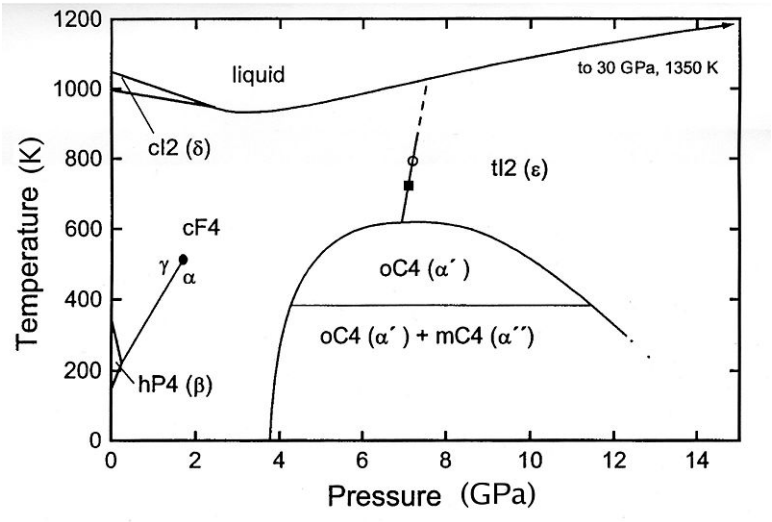

Figure 2.1: Cerium phase diagram. Picture taken from Ref. [39].

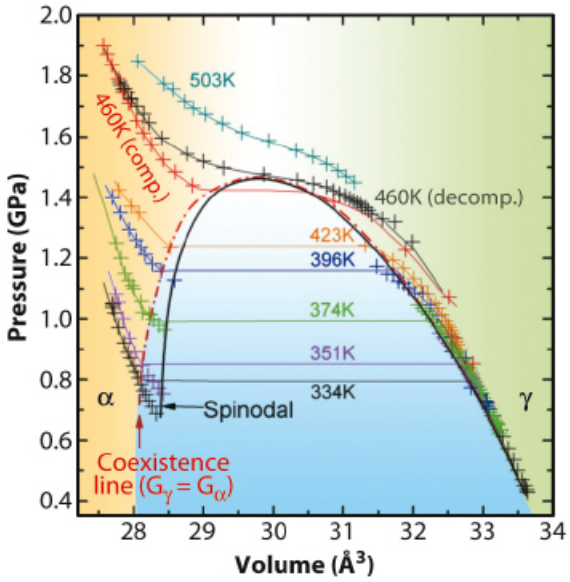

Figure 2.2: Isothermal $p - \mathcal{V}$ diagrams of cerium. The volume collapse is clearly seen when T is lower than the critical temperature, which is approximately $460K$.

2.2 Mott transition scenario

In order to explain the volume collapse of cerium, Johassan in 1974 proposed the Mott transition scenario[46]. In this scenario, the outer shell electrons of the cerium are divided into two groups, the *spd* electrons which form the conduction band and are just spectators of the volume collapse transition, and the $4f$ electron which plays the central role in the $\gamma \to \alpha$ transition. In this scenario,

we assume that electronic properties of cerium can be captured by the Hubbard model[9], which is

$$\hat{H} = -t \sum_{\langle i,j \rangle, \sigma} \left(\hat{c}^{\dagger}_{i,\sigma} \hat{c}_{j,\sigma} + h.c. \right) + U \sum_{i} \hat{n}_{i,\uparrow} \hat{n}_{i,\downarrow} \tag{2.1}$$

Here, $\hat{c}^{\dagger}_{i,\sigma}, \hat{c}_{i,\sigma}$ creates and destroys an electron with spin σ on lattice site i, $\langle i,j \rangle$ means only nearest neighbor lattice sites i,j are taken into account, t is the hopping amplitude of the conduction, $\hat{n}_{i,\sigma}$ is the number operator of the electron with spin σ on site i, and U is the repulsive Coulomb interaction between two electrons of opposite spins on the same lattice. This is simplest possible model that captures the competition between the hopping and the Coulomb repulsion between electrons. This model can describe the Mott metal-insulator transition (MIT)[23, 24, 55, 56], and is employed in the formulation of the Mott transition scenario. In the large volume γ phase, where the lattice constant is large, and the hopping of the $4f$ from one site to its neighbor is prohibitively energy consuming, the $4f$ electrons are assumed to be essentially localized. When the volume collapses, the lattice constant becomes smaller, which renders the hopping of the $4f$ possible. Therefore, in the small volume α phase, we expect the $4f$ electrons to become delocalized. This localization-delocalization transition of the $4f$ electrons is reminiscent of the Mott MIT in the Hubbard model, and prompts Johanssan to propose the Mott transition scenario to explain the cerium volume collapse. This model captures some key aspects of the cerium volume collapse, and can reproduce the spectrum features of the cerium in the γ and α phase. For example, in the γ phase, the $4f$ are localized, and the quasi-particle peak at the Fermi energy, if it exists, is extremely small. Whereas in the α phase, the delocalized $4f$ electrons form a Fermi liquid, which exhibits a pronounced quasi-particle peak at the Fermi energy[56].

2.3 Kondo volume collpase scenario

In 1982, Allen and Martin proposed the Kondo volume collapse (KVC)[47] scenario based on the newly found exact solution of the Kondo problem using the Bethe ansatz[57–59]. From the exact solution of the Kondo problem, the authors are able to obtain the explicit expression of the electronic free energy $F_K(T, J)$ as a function of the temperature T and the Kondo exchange interaction J. The Kondo temperature varies significantly across the $\gamma \rightarrow \alpha$ transition. The Kondo temperature T_K in the α phase is much higher than that in the γ phase. This may be attributed to the variation of the Kondo exchange energy J across the volume collapse transition. When the volume is large,

the Kondo interaction is small, and when the volume is small, the Kondo interaction is large. This is consistent with our intuition and with the experimental results. For a review of the experimental results, see the last section of this chapter.

From the explicit dependence of the electronic free energy on the Kondo exchange constant J, the authors can obtain the volume dependence of the free energy by invoking the empirical relation between J and the volume $\mathcal{V}$, $J \propto \frac{1}{\mathcal{V}^6}$. The authors argue that inclusion of the electronic free energy at finite temperature is not enough to the explain the volume collapse, and they further incorporate the ground state energy $E_G(J)$ at zero temperature. The sum of the electronic free energy $F_K(T, J)$ and the ground state energy $E_G(J)$ gives the electronic part of the total free energy. Another almost equally significant contribution to the total free energy comes from the bulk modulus. The authors assume that Hook's law holds when describing the elastic properties of the cerium, and introduces the mechanical energy $E_M = \frac{1}{2} B_N V_V (V/V_N - 1)^2$ into the total free energy. Here, B_N, V_N are both constant. With the electronic free energy, the electronic ground state energy, and the mechanical energy, the authors are able to obtain the iso-thermal pressure-volume curves by taking the partial derivative of the free energy with respect to the volume at constant temperatures, and show that when the temperature is below some critical value T_c, the pressure-volume curves can develop a kink structure which is an indicator of the emergence of a first order phase transition. And this first order phase transition can be identified as the $\gamma \to \alpha$ phase transition in cerium.

2.4 The role of lattice vibrations in the volume collapse transition

In recent years, several groups have taken the task of either measuring the variation of the Debye temperature [52] or the phonon dispersion[54] across the $\gamma \to \alpha$ transition, and they have obtained sort-of consistent results emphasizing the role of the lattice vibrations during the volume collapse process.

In Ref. [52], the authors used the X-ray diffraction and neutron powder diffraction to measure the variation of the Debye temperature across the $\gamma \to \alpha$ transition. Using the relation

$$\Delta S_{vib}^{\gamma-\alpha} = 3k_B \log \Theta_D^{\gamma} / \Theta_D^{\alpha}, \tag{2.2}$$

where k_B is the Boltzmann constant, Θ_D^{γ} is the Debye temperature in the γ phase, and Θ_D^{α} is the Debye temperature in the α phase, the authors estimated that phonons account for approximately

half of the total entropy change during the volume collapse transition. In Ref. [54], the authors measured the phonon dispersion across the volume collapse process, and found that the phonon contribution accounts for about 1/4 of the total entropy change. Although the precise value of the phonon entropy contribution varies between different measurement methods, many authors hold the belief that the phonons should play an important, if not critical, role in the cerium volume collapse transition. It is because of these observations that we have decided to introduce the electron-phonon correlation in our model, and study the effect of the electron-phonon interaction on the system. Generally, we expect that the electron-phonon interaction should be able to enhance the first order phase transition, and our numerical results are consistent with our expectation.

2.5 Important material parameters for the description of cerium volume collapse

The parameters that are of interest for the PAM + Holstein model are $\omega, U_{eff}, J, B, \alpha, \rho$. Here, Ω_0 is the bare phonon frequency, U_{eff} is the effective electron-phonon coupling, J is the Kondo exchange interaction, B is the bulk modulus, α is the parameter that describes the exponential dependence of bulk modulus on volume change, and ρ is the density of states at the Fermi energy.

Up to now, I have not yet found a paper that directly measures that Kondo exchange interaction. Although in Ref. [60], there is a direct measurement of parameters in the Anderson model, the parameter values do not fit well into the formula that relates the Kondo temperature with the parameters in the Anderson model. Therefore, I have chosen to calculate the Kondo exchange interaction from the density of states and Kondo temperatures.

2.5.1 Calculation of Ω_0

In Ref. [61, 62], the authors calculate the phonon properties of Cerium using DFT. They have assumed that phonon frequencies is proportional to Debye temperature, with the proportionality being 0.69. According to these results, the phonon frequencies are different in the γ and α phases of Cerium. That is,

$$\Omega_0 = \begin{cases} 119K, \alpha \\ 81K, \gamma \end{cases} \tag{2.3}$$

We know that the band width of Cerium is approximately 0.52 eV, which corresponds to 6000K. Therefore, it is approximately true that phonon frequency is one percent of the band width.

2.5.2 Calculation of electron-phonon coupling constant

Still in Ref. [61, 62], the authors also calculate the dimensionless electron-phonon coupling constant. The dimensionless electron-phonon coupling constant λ, originally defined in Ref. [63], is approximately equal to $N(E_f) * U_{eff}$. Here, $N(E_f)$ is the density of states near Fermi energy. Therefore, the effective electron-phonon coupling constant is $U_{eff} = \frac{\lambda}{N(E_f)}$. In Ref. [62], the authors calculate the dimensionless electron-phonon coupling constant using DFT for two different assumptions. When they assume that the $5p$ electrons are core electrons, they obtain one set of electron-phonon coupling constants; when they assume that the $5p$ electrons are band electrons, then they obtain another set of electron-phonon coupling constants. However, the two set of values for λ do not differ from each other significantly. Since we are making the assumption that the $5p$ electrons are band electrons, we will adopt the second set of values for λ. They are

$$\lambda = \begin{cases} 0.32, \alpha \\ 0.47, \gamma \end{cases} \tag{2.4}$$

In order to obtain the effective electron-phonon coupling constant, we also need to know the value of density of states at Fermi energy. In Ref. [62], $N(E_f)$ is also calculated in DFT. However, different DFT methods give different $N(E_f)$. When full-potential linearized augmented plane wave (FLAPW) method is used, the DOS at Fermi energy is (Ry = 13.6 eV)

$$N(E_f) = \begin{cases} 37.58/Ry, \alpha \\ 57/Ry, \gamma \end{cases} \tag{2.5}$$

On the other hand, when linear Muffin-tin orbital (LMTO) method is used, the DOS at Fermi

energy is

$$N(E_f) = \begin{cases} 32.7/Ry, \alpha \\ 63.3/Ry, \gamma \end{cases} \tag{2.6}$$

Thus, the effective electron-phonon coupling constant U_{eff} is (FLAPW)

$$U_{eff} = \begin{cases} 0.12eV, \alpha \\ 0.11eV, \gamma \end{cases} \tag{2.7}$$

or (LMTO)

$$U_{eff} = \begin{cases} 0.13eV, \alpha \\ 0.1eV, \gamma \end{cases} \tag{2.8}$$

We can see that the electron-phonon coupling constant is approximately 1/5 of the band width.

2.5.3 Values of Kondo exchange interaction J and DOS ρ

Due to the lack of direct measurement of Kondo exchange interaction J, we need to calculate the value of Kondo exchange interaction J from band width and DOS through this formula $T_K = De^{-\frac{1}{\rho J}}$. The experimental values of Kondo temperature are available in many papers. However, different papers give different Kondo temperatures, and the difference can be pretty significant sometimes. Generally, the Kondo temperature in α phase is much larger than the Kondo temperature in γ phase. According to Ref. [61], Kondo temperature lies between 50K and 100K in γ phase, and lies between 1000K and 2000K in the α phase. This means the Kondo temperature in α phase is about 20 to 40 times higher than the Kondo temperature in γ phase. Therefore, it is natural to expect that the Kondo exchange interaction J is larger in α phase than it is in γ phase. In Ref. [60, 64], the Kondo temperature is given as $T_K = 945K$ in α phase and 95K in γ phase. in Ref. [64, 65], the Kondo temperature is 1800-2000K in α phase and 60K in γ phase. From the band width D, the Kondo temperature T_K, and the DOS ρ, we can calculate the value of Kondo exchange interaction as $J = -\frac{1}{\rho \log \frac{T_K}{D}}$.

If we take the DOS at Fermi level to be 37.58/Ry in the α phase[62], then the value of J ranges between 0.196 eV and 0.33 eV, with the larger value of J corresponding to higher Kondo temperature. Similarly, if we take the DOS to be 57/Ry in the γ phase, then the value of J ranges

between 0.049 eV and 0.058 eV. In table form, this would be

$$T_K = \begin{cases} 945K - 2000K, \alpha \\ 50K - 100K, \gamma \end{cases} \tag{2.9}$$

$$J = \begin{cases} 0.196eV - 0.33eV, \alpha \\ 0.049eV - 0.058eV, \gamma \end{cases} \tag{2.10}$$

It is clear that $J_\alpha \gg J_\gamma$.

In the above analysis, we have used the DOS from Ref. [62] that is calculated using FLAPW method. Even if we use some other data for DOS, for example, the results that are calculated using LMTO, the value of J does not change much.

2.5.4 Bulk modulus properties of Cerium

Because of the presence of the phase transitions between different phases for Cerium, its bulk moduli depend on the external pressure and the temperature. According to Ref. [66], there is a softening behavior in bulk modulus when Cerium makes a transition from γ phase to α phase. This is expected since the electronic contribution to the volume collapse has already been taken into account when we measure the volume dependence of Cerium bulk modulus. In order to see how the bulk modulus depends upon volume without the electronic contribution, we need to resort to the metals that do not display such kind of phase transitions. The bulk moduli of many metals are measured in Ref. [67], in which the author proposed this formula to describe the volume dependence of bulk modulus for the metals he measured:

$$B_T = B_0 e^{\alpha \Delta V / V_0}. \tag{2.11}$$

Here, B_0 is the bulk modulus without external pressure, α is a dimensionless parameter whose values depend on the materials, V_0 is the normal volume, $\Delta V = V_0 - V$ represents the volume change, and B_T means the bulk moduli are measured at constant temperature. The value of α changes from material to material, but the difference between materials is not quite large. According to the data provided by the author, we conclude that the value of α varies approximately between 2 and 5. Given that the bulk modulus of Cerium is strongly renormalized by the iso-structural $\gamma \to \alpha$

transition, we cannot directly read off the value of α for Cerium. What we can do is to see how the metals that are adjacent to Cerium behave under external pressure. Praseodymium just follows Cerium in the periodic table, and its equation of state is measured in Ref. [68]. Using the $P-V$ relationship in this paper, we can extract the α value of Praseodymium to be 2.49, which lies within the range 2-5 for the metals measured in Ref. [67]. This value can also be used to estimate the volume dependence of Cerium bulk modulus since both elements belong to the Lanthanide series.

For the values of B_0 and V_0, the authors of Ref. [47] have adopted the average bulk moduli and atomic volumes of La and Pr, and set $B_0 = 28GPa, V_0 = 36\mathring{A}^3$.

2.5.5 Parameters in table form

ω	U_{eff}	J	B_0	α	ρ
81K - 119K	0.1eV - 0.13 eV	$0.196eV - 0.33eV, \alpha$ $0.049eV - 0.058eV, \gamma$	28GPa	2-5	$2.4/eV - 2.76/eV, \alpha$ $4.12/eV - 4.65/eV, \gamma$

Chapter 3

Numerical Methods

In this chapter, I will discuss the methods that we employed for the solution of our model. We have mainly used three methods to solve our model, which are the dynamical mean field theory (DMFT), the continuous time quantum Monte Carlo method (CTQMC), and the maximum entropy method (maxEnt). We first map the original lattice model into a single impurity model that is the embedded in a medium. The medium itself needs to be determined self-consistently. We then use an iteration cycle to solve this self-consistently embedded single impurity model. The most difficult part of the iteration cycle consists of solving the impurity problem. For this, we use the CTQMC as our impurity solver. The CTQMC is a newly developed diagrammatic method for generating the interaction Green function from the bath Green function. We use the weak coupling expansion version of the CTQMC in our program. The time complexity of the program is $O(\beta^3)$, and thus we cannot go to very low temperatures. Once we have the Matsubara Green function, we can use the maximum entropy method to extract the spectral functions. We can extract the spectral function either from the imaginary time Green function $G(\tau)$ or from the imaginary frequency Green function $G(i\omega_n)$. These two methods should give identical results. In practice, the result obtained from $G(i\omega_n)$ is generally better than the result obtained from $G(\tau)$, and thus throughout our work, we only use the spectral functions that are extracted from $G(i\omega_n)$.

3.1 Dynamical mean field theory

Dynamical mean field theory (DMFT) is an approximation that ignores the spatial correlations while preserving all the temporal correlations[69]. The idea of DMFT was proposed in 1989 by Metzner and Vollhardt [12], and was later widely used to study the Hubbard model [15], the Holstein model [27], the periodic Anderson model[29], etc. The precursor of DMFT is the mean field theory (MFT) which is widely used to simplify some complicated Hamiltonians, such as the ones describing superconductivity, magnetism, and charge density wave. Considering the similarity of DMFT and MFT, it is worthwhile to give a brief introduction to the MFT first.

3.1.1 Classical mean field theory

Mean field theory was first invented by Van der Waals to study the phase transition in real gas in the late 19th century. In 1907, Weiss re-invented the mean field theory to elucidate the mechanism for the emergence of magnetism. In the language of modern physics, Weiss's method for dealing with magnetism is equivalent to a mean-field solution to the Ising model, which is $\hat{H} = -J\sum_{\langle i,j\rangle} s_i s_j$, where J is the exchange integral between neighboring spins, $s_i = \pm 1$ corresponds to either up or down spin, and $\langle i, j\rangle$ means only nearest neighbor interaction is taken into account. In the mean field approach to this Hamiltonian, we single out one spin and assume that this electron is immersed in an effective magnetic field H_{eff} that is created by all the other spins in the system. The effective magnetic field is proportional to the expectation value of s_i, which is itself the magnetization of this system. This means that $H_{eff} = \tilde{J}m$, where $m = \langle s_i\rangle$, and by the translational invariance of our system, the expectation value of s_i is independent of the lattice index. By this approximation, the original Hamiltonian can be rewritten as $\hat{H} = -\sum_i H_{eff} s_i$, which is now easily solvable. The expectation value of s_i can now be obtained as

$$\begin{aligned} m &= \langle s_i\rangle \\ &= \frac{1}{Z}\mathrm{Tr}\Big(s_i e^{-\beta\hat{H}}\Big) \\ &= \tanh\beta H_{eff}. \end{aligned} \tag{3.1}$$

Here, in this equation, $\beta = \frac{1}{k_B T}$, and k_B is the Boltzmann constant. Note that the effective field H_{eff} depends on the value of m. Thus here we have obtained a self-consistent equation for the magnetization m, and the solution of this equation yields a mean-field description of the spontaneous magnetization caused by the exchange integral J.

3.1.2 Mean field theory with temporal correlations included

Dynamical mean field theory (DMFT) is a quantum analogue of the classical mean field theory. Similar to the classical mean field theory, in DMFT, the spatial degrees of freedom are frozen, and only the temporal fluctuations are considered. Assume we have a real lattice model, where the electrons can hop between neighboring lattice sites, and the electrons experience Coulomb repulsive interactions when two electrons with opposite spins reside on the same lattice site. This is actually the Hubbard model. In order to solve this model, we can single out one electron, and assume that

the real interactions of this electron with all the other electrons can be described by a simplified scenario, where the electron we have singled out has an infinite number of neighbors. All of these neighboring electrons in synergy create an effective medium, within which the electron we have singled out is immersed. Up to now, the scenario is the same as that in the classical mean field theory. What is different in DMFT is that the electron not only experiences the effects from the medium, but can also hop to and then hop back from the bath medium. By taking this hopping process into account, we have fully incorporated the temporal fluctuations. Thus, the original mean field theory has adopted a temporal degree of freedom, from which the *dynamical* comes.

In DMFT, the bath medium is described by the bath Green function G_0, and the self-consistently embedded impurity is described by the fully interacting Green function G. Initially, we do not know either G_0 or G. We need to find them self-consistently using an iteration cycle. The first step in the cycle is to start with an arbitrary bath Green function, which we generally take to be the coarse-grained non-interacting lattice Green function, that is,

$$G_0(i\omega_n) = \sum_{\boldsymbol{k}} \frac{1}{i\omega_n - \epsilon_{\boldsymbol{k}}}. \tag{3.2}$$

From the initial bath Green function, we can use the impurity solver to obtain the fully interacting impurity Green function $G(i\omega_n)$. With the impurity Green function, we can use the Dyson's equation to obtain the self energy as

$$\Sigma(i\omega_n) = G_0^{-1}(i\omega_n) - G^{-1}(i\omega_n). \tag{3.3}$$

Once we have the self energy, we can calculate the coarse-grained lattice Green function as

$$G_{cg}(i\omega_n) = \sum_{\boldsymbol{k}} \frac{1}{i\omega_n - \epsilon_{\boldsymbol{k}} - \Sigma(i\omega_n)}. \tag{3.4}$$

From the coarse-grained Green function and the self energy, we can use the Dyson's equation to

obtain the updated bath Green function as

$$G_0^{new}(i\omega_n) = \Big(G_{cg}^{-1}(i\omega_n) - \Sigma(i\omega_n)\Big)^{-1}. \tag{3.5}$$

Now that we have an updated bath Green function, we can start the cycle all over again until the impurity Green function $G(i\omega_n)$ is equal to the coarse-grained Green function $G_{cg}(i\omega_n)$ within numerical error tolerance.

The above is a sketch of the DMFT cycle that we used to solve our model. However, there is no mathematical theorem that guarantees the convergence of this iteration cycle. During the iteration cycle, we may get solutions that oscillate between tow limits, and we may also get solutions that vary depending on the initial input. If the iteration cycle converges, then the final result should be independent of the initial input. When the final result does depend on the initial input, there is probably a coexistence of more than on solution, and interesting physics may be lurking.

The DMFT approximation is exact in the infinite dimension limit. When the dimension is infinite, we need to scale the hopping parameter as $t \to \frac{t}{\sqrt{D}}$, where D is the dimension. Moreover, we can use the density of states (DOS) to convert the summation over the momentum to an integral over energy. The DOS depends on the dispersion relation $\epsilon_{\boldsymbol{k}}$ and the shape of the lattice. It was shown in Ref. [13] that the DOS of the hyper-cubic lattice is always Gaussian as long as only hopping along the axis directions are considered. For a review of the DOS's for different lattices, see Ref. [69]. One remarkable thing of the DMFT is that the final results are essentially independent of the detailed shape of the lattice.

3.1.3 DMFT equations for the PAM+Holstein model

Our model is the PAM + Holstein model, where we have two species of electrons, the conduction c electrons and the localized f electrons. Because of this, the Green function and the self energy are both 2×2 matrices. In order to solve this model, we need to generalize the DMFT formulae in the previous section.

For the two-band model, the lattice single-particle Green function in our model with self energy taken into account is

$$G_{\boldsymbol{k}}^{-1}(i\omega_n) = \begin{pmatrix} i\omega_n - \epsilon_{\boldsymbol{k}} + \mu - \Sigma^{cc} & -V - \Sigma^{cf} \\ -V - \Sigma^{fc} & i\omega_n - (\epsilon_f - \mu) - \Sigma^{ff} \end{pmatrix} \tag{3.6}$$

Now define

$$\begin{aligned}
\alpha_n &= i\omega_n - (\epsilon_f - \mu) - \Sigma^{ff} \\
\beta_n &= i\omega_n + \mu - \Sigma^{cc} \\
\gamma_n &= \beta_n - \frac{(V + \Sigma^{cf})(V + \Sigma^{fc})}{\alpha_n}
\end{aligned} \tag{3.7}$$

Then, Green functions can be written as

$$\begin{aligned}
G^{cc}_{\boldsymbol{k}}(i\omega_n) &= \frac{1}{\gamma_n - \epsilon_{\boldsymbol{k}}} \\
G^{cf}_{\boldsymbol{k}}(i\omega_n) &= \frac{V + \Sigma^{cf}}{\alpha_n}\frac{1}{\gamma_n - \epsilon_{\boldsymbol{k}}} \\
G^{fc}_{\boldsymbol{k}}(i\omega_n) &= \frac{V + \Sigma^{fc}}{\alpha_n}\frac{1}{\gamma_n - \epsilon_{\boldsymbol{k}}} \\
G^{ff}_{\boldsymbol{k}}(i\omega_n) &= \frac{1}{\alpha_n}\frac{\beta_n - \epsilon_{\boldsymbol{k}}}{\gamma_n - \epsilon_{\boldsymbol{k}}}
\end{aligned} \tag{3.8}$$

The coarse grained Green function is $G(i\omega_n) = \sum_{\boldsymbol{k}} G_{\boldsymbol{k}}(i\omega_n)$. Now we define the one particle density of states (DOS) as $\rho(\epsilon) = \langle \delta(\epsilon - \epsilon_{\boldsymbol{k}}) \rangle_{\boldsymbol{k}}$. For the hyper-cubic lattice, it can be shown that the one particle DOS is $\rho(\epsilon) = \frac{1}{\sqrt{2\pi}t} e^{-\frac{\epsilon^2}{2t^2}}$. Therefore, the coarse-grained Green function can be rewritten as

$$\begin{aligned}
G^{cc}(i\omega_n) &= \int d\epsilon \frac{1}{\gamma_n - \epsilon}\frac{1}{\sqrt{2\pi}t} e^{-\frac{\epsilon^2}{2t^2}} \\
&= w(\gamma_n) \\
G^{cf}(i\omega_n) &= \frac{V + \Sigma^{cf}}{\alpha_n} w(\gamma_n) \\
G^{fc}(i\omega_n) &= \frac{V + \Sigma^{fc}}{\alpha_n} w(\gamma_n) \\
G^{ff}(i\omega_n) &= \frac{1}{\alpha_n}\frac{1}{N}\sum_{\boldsymbol{k}} \frac{\beta_n - \epsilon_{\boldsymbol{k}}}{\gamma_n - \epsilon_{\boldsymbol{k}}} \\
&= \frac{1}{\alpha_n}\frac{1}{N}\sum_{\boldsymbol{k}} \left(1 + \frac{(V + \Sigma^{cf})(V + \Sigma^{fc})}{\alpha_n}\frac{1}{\gamma_n - \epsilon_{\boldsymbol{k}}} \right) \\
&= \frac{1}{\alpha_n}\left(1 + \frac{(V + \Sigma^{cf})(V + \Sigma^{fc})}{\alpha_n} w(\gamma_n) \right)
\end{aligned} \tag{3.9}$$

These are the formulae that we used in our program to calculate the single-particle Green function.

3.2 Continuous time quantum Monte Carlo

As noted in the previous section, we need an impurity solver to obtain the impurity Green function from the bath Green function. This is the most difficult part of the DMFT iteration cycle. In this thesis work, we have used the continuous time quantum Monte Carlo (CTQMC) as the impurity solver. There are two widely used CTQMC versions, one is the hybridization expansion and the other is the weak coupling expansion. Here, we are going to use the weak coupling expansion CTQMC as our impurity solver.

The weak coupling expansion CTQMC depends on the decomposition of the Hamiltonian into two parts, the bare Hamiltonian $\hat{H}_0$, and the interacting part of the Hamiltonian $\hat{H}_I$, that is, $\hat{H} = \hat{H}_0 + \hat{H}_I$. With this decomposition, we can write the partition function as

$$Z = \mathrm{Tr} e^{-\beta\hat{H}_0 - \beta\hat{H}_I}. \tag{3.10}$$

Now define the operator $\hat{U}(\tau) = e^{-\tau\hat{H}} e^{\tau\hat{H}_0}$. The differential of this operator is

$$\frac{d\hat{U}(\tau)}{d\tau} = -\hat{H}(\tau)\hat{U}(\tau), \tag{3.11}$$

where $\hat{H}(\tau) = e^{-\tau\hat{H}}\hat{H}_0 e^{\tau\hat{H}}$ is the interaction Hamiltonian in the Heisenberg picture. Integration of the above operator differential equation gives us an iterative integral equation. With the boundary condition that $\hat{U}(0) = \hat{I}$, we have

$$\begin{aligned}
\hat{U}(\beta) &= \hat{I} - \int_0^\beta \hat{H}_I(\tau)\hat{U}(\tau)d\tau \\
&= \hat{I} - \int_0^\beta \hat{H}_I(\tau_1)d\tau_1 + (-1)^2 \int_0^\beta \hat{H}_I(\tau_1) \int_0^{\tau_1} \hat{H}_I(\tau_2)d\tau_2 d\tau_1 + ... \\
&= \hat{I} - \int_0^\beta \hat{H}_I(\tau_1)d\tau_1 + \frac{(-1)^2}{2!} \int_0^\beta d\tau_1 \int_0^\beta d\tau_2 T_\tau \hat{H}_I(\tau_1)\hat{H}_I(\tau_2) + ... \\
&= T_\tau e^{-\int_0^\beta \hat{H}_I(\tau)d\tau}
\end{aligned} \tag{3.12}$$

With the operator $\hat{U}(\tau)$, the partition function can be re-written as

$$\begin{aligned}
Z &= \mathrm{Tr} e^{-\beta\hat{H}} e^{\beta\hat{H}_0} e^{-\beta\hat{H}_0} \\
&= \mathrm{Tr}\hat{U}(\beta) e^{-\beta\hat{H}_0} \\
&= \mathrm{Tr} T_\tau e^{-\int_0^\beta \hat{H}_I(\tau)d\tau} e^{-\beta\hat{H}_0}
\end{aligned} \tag{3.13}$$

Expanding the exponential function, we have

$$Z = \mathrm{Tr} \sum_{n=0}^{\infty} \frac{(-1)^n}{n!} \int_0^\beta d\tau_1 \int_0^\beta d\tau_2 ... \int_0^\beta d\tau_n T_\tau \hat{H}_I(\tau_1)\hat{H}_I(\tau_2)...\hat{H}_I(\tau_n) e^{-\beta \hat{H}_0} \tag{3.14}$$

With the notation $Z_0 = \mathrm{Tr} e^{-\beta \hat{H}_0}$, $\langle \hat{O} \rangle_0 = \frac{1}{Z_0} \mathrm{Tr} e^{-\beta \hat{H}_0} \hat{O}$, we can rewrite the above expression as

$$\frac{Z}{Z_0} = \sum_{n=0}^{\infty} \frac{(-1)^n}{n!} \int_0^\beta d\tau_1 \int_0^\beta d\tau_2 ... \int_0^\beta d\tau_n \langle T_\tau \hat{H}_I(\tau_1)\hat{H}_I(\tau_2)...\hat{H}_I(\tau_n) \rangle_0 \tag{3.15}$$

This is our basic equation of the weak coupling expansion CTQMC[35]. The above derivation is independent of the detailed form of the Hamiltonian, and thus is applicable to any Hamiltonian that can be decomposed into the non-interacting part and the interacting part. Generally, we call the non-interacting Hamiltonian the kinetic energy, and the interacting Hamiltonian the potential energy. By doing this, we are expanding the partition function using the interacting Hamiltonian as the expansion element, and we call each interacting Hamiltonian element a vertex. In the Monte Carlo process, we add or delete a vertex with certain probability, the value of which is calculated using the Metropolis algorithm[36]. During the application of the Monte Carlo algorithm, we generally introduce auxiliary spins either to avoid the negative sign problem in Fermions or to implement the Hubbard-Stratonovich transformation. The auxiliary spins are Ising spins that may either point to the up direction or the down direction. Thus, in the Monte Carlo process, besides adding or deleting a vertex, we can also flip these spins.

When we run the Monte Carlo simulation, we generally start with 0 vertices. Using the Metropolis algorithm, in each Monte Carlo step, we either add a vertex or delete a vertex, or flip one auxiliary spin. After a long time of Monte Carlo process, the number of vertices will fluctuate around a mean value $\langle n \rangle$, which related to the original Hamiltonian by the integration

$$\langle n \rangle = -\int_0^\beta d\tau \langle \hat{H}_I(\tau) \rangle_0. \tag{3.16}$$

Thus, the larger the ratio of potential energy with respect to the kinetic energy, the more vertices there are when the Monte Carlo process has reached the thermal equilibrium. When the system is already in thermal equilibrium, we can start to measure the quantity we are interested in. In order to avoid correlations between successive measurements, we will skip several Monte Carlo updates between two consecutive measurements. We can determine the length of the skip by calculating the autocorrelation time of the Monte Carlo measurements, and choose the number of skips in such

a way that the autocorrelation time is no larger than 2, thus reducing the correlations among the Monte Carlo measurements.

Our model Hamiltonian contains phonons, which can be integrated out to yield a retarded interaction between electron densities. The integration of the phonons was shown in the Appendix A. It can also be found in Ref. [36]. After integrating out the phonons, we are left with a purely electronic model, and CTQMC described above is still applicable in our model. The time complexity of the CTQMC is $O(\beta^3)$, and thus when the temperature is pretty low, the program does not work very well. This restricts our exploration of the model Hamiltonian to the relatively high temperature regime. Especially, we cannot study the model at zero temperature using our method. When people need to know the zero temperature properties of a system, they will generally use the numerical renormalization group method[20, 70].

This section does not discuss in detail the CTQMC algorithm, and leaves many topics untouched, such as the Wick's theorem and its relationship to the determinantal algorithm, the auxiliary spin, the avoidance of the negative sign problem, the Metropolis algorithm, the fast update algorithm, etc. Since the Monte Carlo part of the program we are using is already well established and fully tested, the CTQMC does not constitute the main focus of the thesis. Ref. [35] and [36] are good sources of details about this algorithm.

One thing that is noteworthy is that the Monte Carlo simulation can only be done in the imaginary time space, and then we use the Fourier transform to convert the imaginary time Green function into the imaginary frequency Green function. In order to extract the real-frequency information from the Monte Carlo simulation data, we shall resort to the maximum entropy method to which the next section is dedicated.

3.3 Maximum entropy method

In the previous section, we have discussed how to measure the Green function in imaginary frequency space. However, in real experiments, we can only measure the physical quantities as a function of real frequency. For example, the angle-resolved photoemission spectroscopy (ARPES) measures the density of single particle in reciprocal space, thereby enabling people to study the surface states of materials. The measurement of the electronic density of states is done in real frequency space. Because of this, it is not enough to only have the imaginary frequency information. Fortunately, the imaginary frequency Matsubara Green function is related to the the real frequency Green function

through a simple replacement. From the Lehmann representation[71, 72], we know that the imaginary frequency Green function is related with the retarded real frequency Green function through the replacement $i\omega_n \to \omega + i\delta$, where δ is an infinitesimal positive number. Therefore, if we know the analytical formula for the imaginary time Green function $G(i\omega_n)$, then it is a trivial task to get the real frequency Green function. For example, for the non-interacting Fermion, the Matsubara Green function is $G(i\omega_n) = \frac{1}{i\omega_n - \epsilon}$, and thus the real frequency Green function is $G(\omega) = \frac{1}{\omega + i\delta - \epsilon}$. However, our numerical methods can only yield numerical results for the Matsubara Green function, and these numerical results are invariably associated with all kinds of numerical noises. Even worse, there are (not necessarily weak and short-ranged) correlations between different Matsubara frequencies. Given these numerical data with errors and correlations, we need to find an ingenious method to extract the spectral function from the Green function. Maximum entropy (maxEnt) method [73] as detailed in the review article [37] was just devised to solve this tricky problem. A brief sketch of the method is given below.

The spectral representation of the Green function is

$$\begin{aligned} G(i\omega_n) &= \int_{-\infty}^{\infty} d\omega \frac{A(\omega)}{i\omega_n - \omega} \\ &:= KA \end{aligned} \tag{3.17}$$

Here, $A(\omega)$ is the spectral function that we want to extract. For Fermions, the spectral function is always positive. The calculation of the $A(\omega)$ initially seems not to be especially difficult, since we know that this is actually a Hilbert transformation, and thus we can apply the inverse Hilbert transformation to solve the $A(\omega)$ from $G(i\omega_n)$. However, it turns out that this equation is hardly invertible. There are infinitely many and significantly distinct spectral functions that can reproduce the Green function within numerical error bars. Our job now is to choose the best spectral function from these infinitely many possible solutions. The criterion of choosing the best spectral function is to select a spectral function that can maximize the functional $Q[A(\omega)]$, which is defined as

$$Q = \alpha S - \frac{1}{2}\chi^2. \tag{3.18}$$

Here, $S = -\int d\omega A(\omega) \log \frac{A(\omega)}{M(\omega)}$ is the entropy, and $\chi^2 = (G - KA)C^{-1}(G - KA)$, with C being the covariance matrix. $M(\omega)$ in the entropy is a featureless model function which we generally take to be Gaussian. We can see from the definition of Q that it is a functional of the spectral function. In order to find the $A(\omega)$ that can maximize Q, we take the functional derivative of Q with respect

to $A(\omega)$ and set the derivative to 0. That is, we define $f[A(\omega)] = \frac{\delta Q}{\delta A(\omega)}$, and try to find the root of the equation $f[A(\omega)] = 0$. Newton's method is widely used to find the root of this equation. For each specific value of α, we can find a solution $A_\alpha(\omega)$ that depends on the value of α. If we plug the $A_\alpha(\omega)$ back into the functional Q, we can obtain a function $Q(\alpha)$. The determination of the best value of α is also a tricky task. Some people choose the α that maximizes that the Q (classical method), and some people choose to integrate over the α, with the integration weight being e^{Q_α}(Bryan's method)[74]. It is generally believed that Bryan's method gives better results, and thus in our work, we choose to use Bryan's method to extract the spectral functions.

Here, I have only given a brief sketch of the maxEnt method, leaving many details untouched. The details are shown in the Appendix B. Even more details about this method can be found in the review article [37].

3.4 Calculation of the free energy

We study our model in order to explain the volume collapse phenomenon in Cerium. We know that the volume collapse is a first order phase transition. According to the laws of statistical mechanics, when there is a first-order phase transition, the isothermal pressure-volume ($p - \mathcal{V}$) graph should develop a kink, while at the same time, the free energy versus volume curve should be tangent to a line with two touching points, as shown in Fig. 3.1[75]. In order to obtain the equation of state (EOS) of cerium, we need to find the free energy as a function of volume and temperature, and then take the partial derivative of the free energy with respect to the volume at different temperatures to obtain the isothermal $p-\mathcal{V}$ diagrams. In our model, the volume $\mathcal{V}$ is related with the hybridization parameter V through the relation $V = \frac{b}{\mathcal{V}^2}$. Thus, once we have the free energy as a function of the hybridization parameter V, we can obtain the electronic contribution to the $p-\mathcal{V}$ relation. We will see in the next chapter that only taking into account of the electronic contribution to the pressure is not enough to have a first order phase transition. But for now, we will only focus on the calculation of the pressure due to the electrons.

3.4.1 Calculation of the free energy using the Green function method

It is shown in Appendix A that we can calculate the total energy of the system once we know the Green function. The total energy is equal to the kinetic energy plus the potential energy,

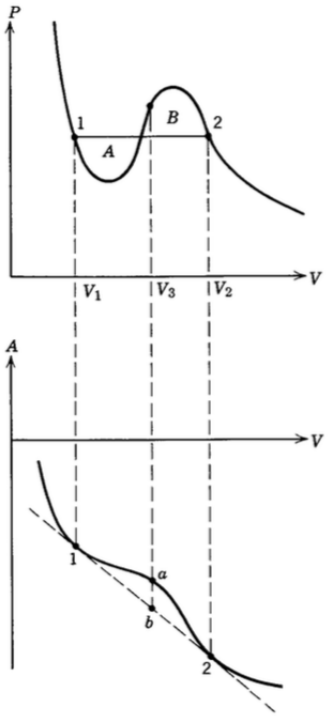

Figure 3.1: Upper panel: pressure versus volume; lower panel: free energy versus volume. Picture from Ref. [75]. The two hallmarks of the first order phase transition, that is, the kink structure in the $p - \mathcal{V}$ diagram and the existence of negative curvature region in the free energy versus volume curve, are concomitant with each other.

$E_{total} = E_{kinetic} + E_V$. The kinetic energy is calculated as

$$E_{kinetic} = \frac{1}{\beta}\mathrm{Tr}\sum_{\boldsymbol{k},\sigma,i\omega_n}\begin{pmatrix} \epsilon_{\boldsymbol{k}} & V \\ V & \epsilon_f \end{pmatrix}\begin{pmatrix} G^{cc}_{\boldsymbol{k},\sigma}(i\omega_n) & G^{cf}_{\boldsymbol{k},\sigma}(i\omega_n) \\ G^{fc}_{\boldsymbol{k},\sigma}(i\omega_n) & G^{ff}_{\boldsymbol{k},\sigma}(i\omega_n) \end{pmatrix}, \tag{3.19}$$

and the potential energy is calculated as

$$E_V = \frac{1}{\beta}\sum_k\sum_{n=-\infty}^{\infty}\mathrm{Tr}\Big[\tilde{\Sigma}_k(i\omega_n)\tilde{G}_k(i\omega_n)\Big]e^{i\omega_n 0^+}. \tag{3.20}$$

Combination of the two terms gives us the total energy. Once we know the total energy as a function of the inverse temperature β for fixed hybridization parameter V, we can integrate the β to obtain the free energy using the formula [76]

$$\begin{aligned} &F = E - TS, \\ &S(\beta) = S(\beta = 0) + \beta E(\beta) - \int_0^\beta E(\beta)d\beta. \end{aligned} \tag{3.21}$$

This is a viable method to calculate the free energy. However, as we used this method to calculate the free energy, we encountered a problem. Since we are using the weak coupling expansion CTQMC as our impurity solver, and according to the Ref. [77], the average expansion order, or the number of vertices at thermal equilibrium, is

$$\langle n \rangle = -\int_0^\beta d\tau \langle \hat{H}_I(\tau) \rangle. \tag{3.22}$$

Here, $\hat{H}_I$ is the interacting part of the Hamiltonian. From the Eq. [3.22], we see that when $\beta \to 0$, the expansion order approaches 0, which means we are having zero vertices when we try to make a Monte Carlo measurement of the Green function. The absence of vertices renders the measurement impossible, and thus we cannot make any meaningful measurements when $\beta \to 0$. Because of this limitation, we have no knowledge of the energy as a function of β when β is infinitesimally small. However, the implementation of the formula [3.22] requires the detailed knowledge of the energy as a function of β near $\beta = 0$ in order to numerically calculate the integral $\int_0^\beta d\beta E(\beta)$. For this reason, we choose not to use the formula [3.22] to calculate the free energy. Instead, we have adopted another formula for the calculation of the free energy using the thermodynamical laws, which will be detailed in the next sub-section.

3.4.2 Calculation of the free energy from the chemical potential

Note that in this section, the Roman V is the hybridization parameter in our model Hamiltonian, and the calligraphic $\mathcal{V}$ is the volume. Empirically, the hybridization is a single-valued function of the volume. However, currently, we do not need to know this empirical relationship. We will need to use this relationship in the next chapter when we try to obtain the pressure versus volume curves for our model. That said, we now continue to derive the formula for the calculation of the free energy from the thermodynamical laws. From the first law of thermodynamics, we know that

$$dE = TdS - pd\mathcal{V} + \mu dN. \tag{3.23}$$

Thus, the differential of the free energy is

$$dF = -pd\mathcal{V} + \mu dN - SdT. \tag{3.24}$$

Once we take the $(T, \mathcal{V}, N)$ as the set of independent variables, we have the relation $\frac{\partial F}{\partial N}\Big|_{T,\mathcal{V}} = \mu$. Therefore, we can set the $T, \mathcal{V}$ to be constant and scan the chemical potential to obtain the corresponding particle number, and integrate the chemical potential over particle number to get the free energy. With this method to calculate the free energy, we do not have to solve the model near $\beta = 0$. This is the method that we employed in this thesis work for the calculation of the free energy.

The free energy is calculated as $F(T, V, N) = \int_0^N \mu dN$, for fixed values of T, V. In order to obtain the $\mu - N$ curve, we scan the values of μ, and for each μ, we obtain the total filling number N. One example of the $\mu - N$ curve is shown in Fig. 3.2. During the application of this method, we need to make sure that we can reach the parameter regime where the total filling number is 0. In order to obtain a zero filling number, sometimes, we need to scan to a very large range of chemical potential. This is especially obvious when β is small. As shown in Fig. 3.2, when $\beta = 10$, the total filling number is already zero when $\mu = -3.2$. However, for $\beta = 1$, the total filing number decays much slower, and we need to scan to $\mu = -12$ have a negligible filling number. Note that in the $\mu - N$ curves, there is a jump when filling number $N = 1$. This is because when $-U/2 < \mu < U/2$, where U is the Hubbard repulsion between the f electrons, the f electron filling number is almost a constant ($n_f = 1$). The f filling number begins to drop down noticeably only when $\mu < -U/2$, which gives rise to the jump in the $\mu - N$ curve. This jump is clearer when the temperature is low than it when the temperature is high, since the thermal fluctuations at high temperature reduce the Hubbard repulsion effect on the filling number. The free energy for each value of V and β can be calculated by numerically evaluating the integral $\int_0^N \mu dN$. As an example, in the inset of the figure, we plot the free energy as a function of β for fixed value of V. Similarly, we can also calculate the free energy as a function of V for fixed values of β. In the next chapter, we will use these $F - V$ data to calculate the pressure versus volume curves.

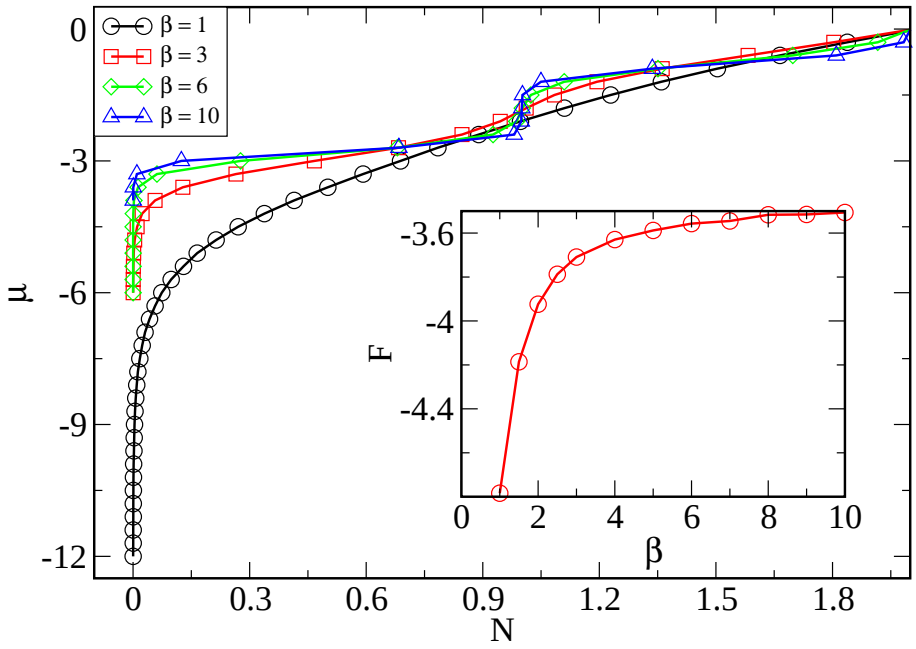

Figure 3.2: Main panel: $\mu - N$ diagrams for different values of β at $U_{eff} = 1, V = 1.6$. The corresponding free energy for a certain temperature is the area enclosed by the curve and the x-axis. Inset: The free energy F versus β calculated by integrating μ versus N.

Chapter 4

PAM+Holstein Model for the Description of Ce Volume Collapse

4.1 Introduction

The isostructural volume collapse of Cerium is a long-standing puzzle [40]. When a crystal of Cerium is under a pressure of 15,000 atmospheres, it undergoes a volume collapse of approximately 17% while preserving the face-centered cubic crystal structure. This transformation, called the $\gamma \rightarrow \alpha$ transition, has baffled physicists since its discovery, and several leading theories have been proposed for its explanation, the most prominent of which are the Mott transition scenario [46] and the Kondo volume collapse (KVC) scenario [47]. The Mott and KVC scenarios are competing paradigms, although perhaps not as different and distinct as previously thought [56, 78].

In the KVC scenario, the $4f$ electrons of Cerium are assumed to be localized in both phases. In the small volume α phase, the *spd* electrons strongly screen the local moments of the f electrons, thus rendering the α phase a Pauli paramagnet. While in the large volume γ phase, the local moments of the f electrons persist to much lower temperatures than in the α phase, indicating that the Kondo scale T_K in the γ phase is much smaller than that of the α phase, which is consistent with the experimental observations [60, 64, 65, 79].

In the Mott transition scenario, for which the Hubbard model is a good description, the density of states (DOS) of the f electrons changes from being metallic (no gap at the Fermi level) in the α phase to insulating (with a gap at the Fermi level) in the γ phase [23, 24, 55, 56]. This localization-delocalization of the $4f$ electrons, which is a metal-insulator Mott transition, is driven by the increase of the intersite hopping amplitudes of the f electrons when the unit cell volume of Cerium decreases.

Recent experimental and theoretical results have indicated that the electron-phonon interaction may also play an important role in the $\gamma \rightarrow \alpha$ transition [52, 54, 80, 81]. Jeong *et al.* estimated that about one half of the entropy change during the transition is due to lattice vibrations. Later, Krisch *et al.* showed that the significant changes in the phonon dispersion across the $\gamma \rightarrow \alpha$ transition

provide strong evidences for the importance of the lattice degrees of freedom. Although the precise value of the lattice vibrational entropy varies between experiments, they do agree that a significant fraction of the total entropy change during the transition is due to lattice vibrations.

Most of the previous works focus exclusively on the electronic part of the Cerium volume collapse transition. Some recent study has further refined the calculations by using the electronic dispersion from the density functional theory (DFT) and combined it with the DMFT (DFT + DMFT) [56, 82–85]. Unfortunately, there is no well developed method to incorporate the electron-phonon interaction into this framework. Moreover phonons with non-trivial dispersions cannot be included in the DMFT.

As a first step to understand the contribution of phonons in the cerium within the Kondo volume collapse scenario, we follow the original approach by Allen and Martin using a single band impurity model. In this work, we use the periodic Anderson model with Holstein phonons coupled to the conduction band as our starting point [86]. Our model Hamiltonian is

$$\begin{aligned} \hat{H} &= \hat{H}_0 + \hat{H}_I \qquad (4.1) \\ \hat{H}_0 &= -t \sum_{\langle i,j\rangle,\sigma} (c^\dagger_{i,\sigma} c_{j,\sigma} + c^\dagger_{j,\sigma} c_{i,\sigma}) + \epsilon_f \sum_{j,\sigma} f^\dagger_{j,\sigma} f_{j,\sigma} \\ &\quad + V \sum_{i,\sigma} (c^\dagger_{i,\sigma} f_{i,\sigma} + f^\dagger_{i,\sigma} c_{i,\sigma}) + \sum_i \left(\frac{P_i^2}{2m} + \frac{1}{2} k X_i^2 \right) \\ \hat{H}_I &= U \sum_i n^f_{i,\uparrow} n^f_{i,\downarrow} + g \sum_{i,\sigma} n^c_{i,\sigma} X_i \,. \end{aligned}$$

Here, $c^\dagger_{i,\sigma}, c_{i,\sigma} (f^\dagger_{i,\sigma}, f_{i,\sigma})$ creates and destroys a $c(f)$ electron of spin σ at lattice site i, respectively. P_i and X_i are the phonon momentum and displacement operators. Here, we have used dispersionless Einstein phonons with frequency $\Omega_0 = \sqrt{k/m}$. The parameter g measures the electron-phonon interaction strength, U is the Hubbard repulsion between localized f-electrons, and V characterizes the hybridization between c- and f-electrons. From the parameters g, k, we construct the effective electron-phonon interaction strength, $U_{eff} = \frac{g^2}{2k}$. Throughout this paper and to be consistent with the experimental results, we have set $\Omega_0 = 0.01$ [86] unless otherwise specified. We also set $U = 4$, the c-electron filling number to 0.8, and the f-electron filling number to 1.0. We propose this simplified model as our first attempt to incorporate the electron-phonon interaction into the study of the Cerium volume collapse.

We solve this model using the dynamical mean field theory [69], with the continuous time quantum Monte Carlo [77] as our impurity solver. We use a hypercubic lattice with Gaussian bare

DOS, and consider its bandwidth as our unit of energy. We set this unit to be the Fermi energy ϵ_F of Cerium, which is 0.52eV [61, 87]. Finally, we use the maximum entropy method [37] to extract the spectral functions from the Monte Carlo simulation data.

4.2 Pressure-volume diagrams

Here, in this section, we are going to show the pressure-volume ($p - \mathcal{V}$) diagrams that we obtained for different parameter regimes. Since the $\gamma \rightarrow \alpha$ transition is first order, the $p - \mathcal{V}$ curve develops a kink as the temperature drops below the transition point. To properly account for the static lattice contribution, we introduce a volume and temperature dependent bulk modulus term into our pressure-volume ($p - \mathcal{V}$) relation [47]. Therefore, the total pressure contains two parts, the pressure due to the electrons which we denote as p_e, and the pressure due to the bulk modulus term which we denote as p_B.

We calculate p_e from the electronic free energy by the relation $p_e = -\frac{\partial F}{\partial \mathcal{V}}$, and p_B by integrating the bulk modulus $B = -\mathcal{V}\frac{\partial p_B}{\partial \mathcal{V}}$. We calculate the electronic free energy using the formula $F_e(T = T_0, V = V_0, N) = \int_0^N \mu dN + F(T_0, V_0, N = 0)$. Here, we choose not to use the entropy formula employed in Ref. [76] because the statistical errors in our results become large at high temperatures. When we plot the free energy versus V, we notice that the curve continuously evolves from a nearly flat plateau at small V to a nearly straight line with a negative slope at large V, as shown in Fig. 4.1. Therefore, the derivative of the free energy with respect to V is almost 0 for small V and approaches a negative constant for large V. One simple function that satisfies this condition is the shifted and stretched tanh, which is

$$\frac{dF_e}{dV} = -k\Big(1 + \tanh a(V - c)\Big). \tag{4.2}$$

Integration of the Eq. [4.2] gives us the function

$$F(V) = -k\Big(V - c + \frac{1}{a}\log 2\cosh a(V - c)\Big) + d. \tag{4.3}$$

We can thus fit the numerical results of the F_e to the above function. Once we have an analytical expression for the F_e, it would be much easier to calculate its derivative to obtain the pressure.

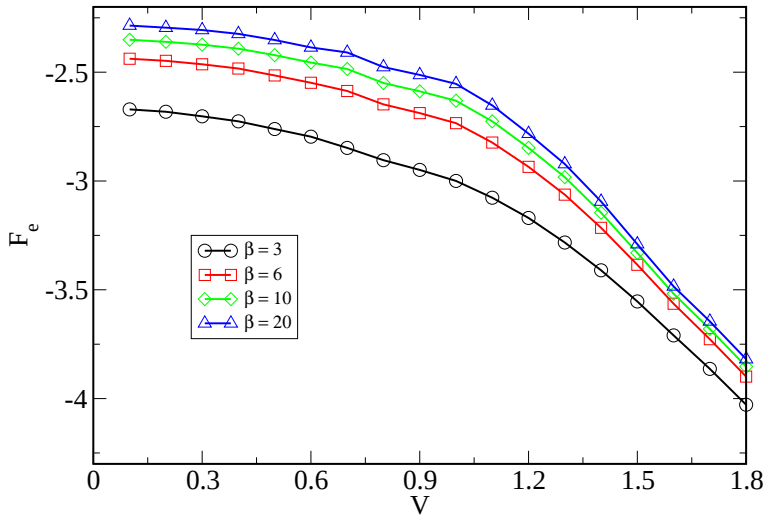

Figure 4.1: The electronic free energy F_e versus V for different values of β with $U_{eff} = 1$. They all share similar shapes, that is, a flat region at small V and a straight line of negative slop at large V.

By fitting our numerical data to Eq. [4.3], we obtain the values of the parameters k, a, c, d. Since the free energy depends on the temperature, these parameters also depend on it. Now, we can obtain the volume dependence of the free energy using the empirical relationship between hybridization V and volume $\mathcal{V}$, $V = \frac{b}{\mathcal{V}^2}$ [88]. Taking the partial derivative of the free energy with respect to volume, we obtain the electronic iso-thermal pressure as

$$p_e = -\frac{2kb}{\mathcal{V}^3}\left(1 + \tanh a\Big(\frac{b}{\mathcal{V}^2} - c\Big)\right). \tag{4.4}$$

The experimental value of b can be estimated from the relation $V = \frac{b}{\mathcal{V}^2}$, and $J \propto \frac{V^2}{U}$[89], where J is the Kondo exchange. The experimental values of J range between $0.2eV - 0.3eV$ in the α phase and $0.05eV - 0.06eV$ in the γ phase[60, 61, 64, 65]. From the values of J and the relation between J and volume, we can estimate the value of b to be between 0.89 and 1.55 in our unit system.

The second contribution to the total pressure comes from the bulk modulus. From the experimental results of Ref. [67, 90], we assume that the bulk modulus depends upon the volume as

$$B = B_0(T)e^{\alpha(1-\mathcal{V}/\mathcal{V}_0)}, \tag{4.5}$$

and upon the temperature through the relation[91]

$$B_0(T) = B_0(1 + e^{-\frac{T_0}{T}}), \tag{4.6}$$

where, $B_0, T_0, \mathcal{V}_0$ and α are material-dependent parameters.

Integration of the bulk modulus gives us the pressure p_B as

$$p_B(\mathcal{V}) = p_0 - B_0(T) \int_1^{\mathcal{V}/\mathcal{V}_0} dx \frac{e^{\alpha(1-x)}}{x}, \tag{4.7}$$

where p_0 is an arbitrary constant.

Adding the bulk modulus and the electronic pressures yields a $p - \mathcal{V}$ graph which exhibits a kink structure. Fig. 4.2 shows the pressure versus volume diagrams for different values of U_{eff}. When $U_{eff} = 1$, as we lower the temperature, a kink structure begins to develop. We identify $\beta = 6$ as the critical temperature where the kink structure begins to emerge. Experimentally, the ratio between the $\gamma \to \alpha$ transition critical temperature T_c and the temperature T_0 where the volume collapse of 17% occurs is $T_c/T_0 = 460/334$[92]. Using the same ratio, we can identify the T_0 in our model to be approximately 1/8. From the iso-thermal $p - \mathcal{V}$ diagrams, we find that the volume collapse in our model at $\beta = 8$ is about 30%, a result that is in reasonable agreement with the experiments, considering that we are using a simplified model to study the real Cerium. From the Maxwell construction, we can read off from the $\beta = 8$ iso-thermal line the volumes for the γ and α phases, with $\mathcal{V}_\alpha = 0.78$, and $\mathcal{V}_\gamma = 1.13$. We further estimate the corresponding hybridization value for these two phases to be $V_\alpha = 1.93$, and $V_\alpha = 0.92$.

The crossing of the $p - \mathcal{V}$ diagrams at different temperatures may be removed once we retain the temperature dependence of the integration constants p_0. Even if we set all the p_0 to 0, as we did in this paper, the crossing could still be a numerical artifact of our approximation, since the introduction of the volume dependence of the hopping amplitude t will make the $p - \mathcal{V}$ diagrams drop faster in the large volume regime, thus possibly eliminating this crossing feature.

On the other hand, when $U_{eff} = 0$ (inset on Fig. 4.2), even though we have used the same set of parameters, the kink structure that is the indicator for the emergence of a first order phase transition is absent. Note that the small upturn in the $p - \mathcal{V}$ diagram at large volume can also be eliminated once we consider the volume dependence for the hopping term t in the conduction band. The different behavior of the $p - \mathcal{V}$ diagram for $U_{eff} = 0$ and $U_{eff} = 1$ implies that the electron-phonon interaction enhances the $\gamma \to \alpha$ volume collapse transition.

Similar results can be obtained with many different combinations of parameters. In the data displayed in Fig. 4.2 we set $b = 1.18, p_0 = 0, T_0 = 0.1, B_0 = 12.47$, and $\alpha = 4.225$. The value of b is within our estimated range. A value of $T_0 = 0.1$ is approximately 600 K within our units, a value comparable to the critical point temperature of the transition. Following Ref. [47], we use $B_0 = 28GPa, \mathcal{V}_0 = 36\text{Å}^3$ as the bulk modulus and unit cell volume for Cerium in the γ phase. Once we use the Fermi scale as our unit of energy and set $\mathcal{V}_0$ as our unit of volume, the unit of pressure becomes $\epsilon_F/\mathcal{V}_0 = 2.3GPa$. This justifies our usage of the value $B_0 = 12.47$ as our bare bulk modulus. And, finally, the experimental values of α range between 2 and 5 for most bulk pure metals [67].

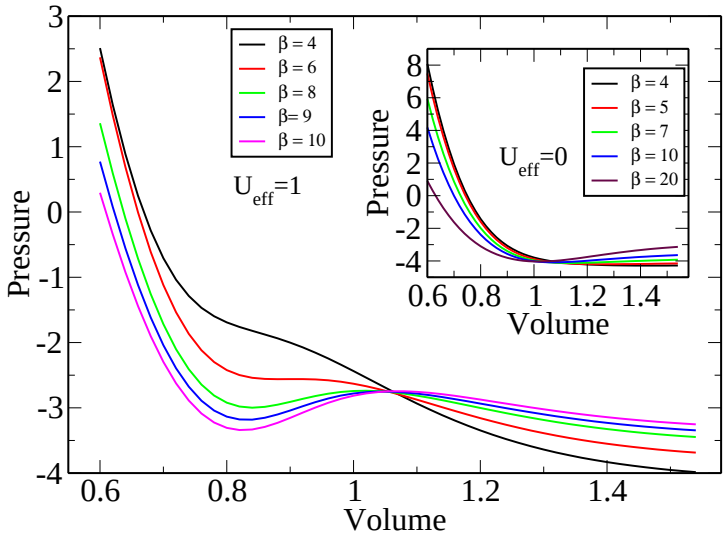

Figure 4.2: Main panel: $p - \mathcal{V}$ diagram for $U_{eff} = 1, \Omega_0 = 0.01$. As the temperature decreases, a kink structure develops in the $p - \mathcal{V}$ graph, indicating the emergence of a first oder phase transition. Inset: $p - \mathcal{V}$ diagram for $U_{eff} = 0$. Here, with the same bulk modulus pressure, the kink structure does not show up.

4.3 Density of states in various parameter regimes

This phonon-enhanced first order phase transition is actually a Mott metal-insulator transition (MIT) which can be better understood by studying the evolution of the spectral functions with respect to the variation of the relative strengths of V and U_{eff}. Depending on the relative strengths of V and U_{eff}, we can divide the parameter regimes into two parts, the small hybridization regime

and the large hybridization regime. The electron-phonon interaction effect, e.g., the opening of a Mott gap at the Fermi energy in the conduction electron spectra, is pretty strong in the small hybridization regime. However, in the large hybridization regime, the electron-phonon interaction effect is strongly suppressed. We shall study these two regimes separately.

4.3.1 Small hybridization regime

When the hybridization is small, the electron-phonon interaction can significantly modify the DOS of the conduction electrons. For $V = 0.1$, as U_{eff} increases from 0 to 1.1, the DOS changes from a nearly Gaussian to a DOS gapped at the Fermi energy, as shown in Fig. 5.1. We can also see the effect of U_{eff} on the gap at the Fermi energy by observing the behavior of the c-electron Green function $G_c(\tau)$. When there is no gap, the value of $G_c(\tau = \beta/2)$ is finite. However, when there is a gap at $\omega = 0$, the value of $G_c(\tau = \beta/2)$ decays to zero exponentially. Moreover, the wider the gap, the more rapid the decay. When we plot the $G_c(\tau)$ for different values of U_{eff}, we see clearly that with increasing U_{eff}, $G_c(\tau)$ decreases increasingly rapidly when τ approaches $\beta/2$.

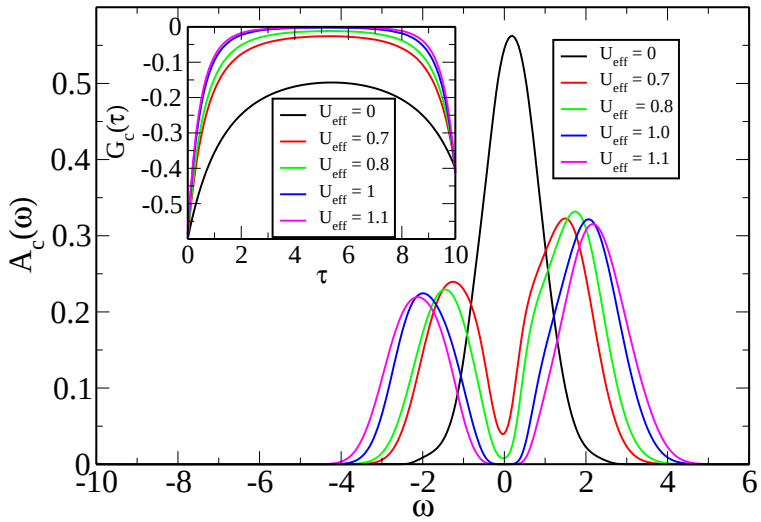

Figure 4.3: Main panel: The conduction electron spectral functions for $V = 0.1, \beta = 10, \Omega_0 = 0.01$. As U_{eff} increases from 0.0 to 1.1, the gap in the DOS becomes increasingly wider. Inset: The evolution of $G_c(\tau)$ with U_{eff}. The increasingly rapid decay of $G_c(\tau = \beta/2)$ also indicates the existence of an energy gap at $\omega = 0$ as U_{eff} grows.

The magnitude of the bare phonon frequency Ω_0 and the c-electron doping level have profound influences on the nature of the MIT due to the U_{eff}. When Ω_0 is small, which is the case we are studying, the transition seems to be continuous or at most extremely weakly discontinuous [93]. The reason is that when $\Omega_0 = 0$, we can integrate out the Holstein phonons to obtain the Falicov-Kimball model in which the conduction electrons always exhibit a non-Fermi liquid behavior for any non-trivial filling number [26, 94]. The MIT from a non-Fermi liquid metal to an insulator is continuous due to the absence of the quasi-particle peak at the Fermi energy in the conduction electron DOS [14]. On the other hand, when $\Omega_0 \to \infty$, the Holstein model can be mapped to an attractive Hubbard model, for which the discontinuous MIT is strongly suppressed by doping away from half filling[95, 96]. Thus, we do not anticipate a first order phase transition for a finite Ω_0 that lies between these two limiting cases. The hitherto absence of a stable hysteresis loop in the $-\frac{1}{\pi}\mathrm{Im}G_c(i\pi T)$ versus U_{eff} plane for varying values of Ω_0 at finite temperature may provide support for this viewpoint. However, if we introduce a phonon-frequency-dependent bulk modulus contribution to our system, we would likely see a first order phase transition as we tune the phonon frequency.

4.3.2 Large hybridization regime

The opening of the Mott gap at the Fermi level is present only when the hybridization between the conduction band and localized electrons is weak compared with the electron-phonon coupling. Fig. 4.4 shows that when the hybridization is strong, the opening of the Mott gap is prohibited. In this parameter regime, the introduction of the electron-phonon interaction has little effect on the behavior of the conduction electron DOS. Since the filling number of the c-electrons is set to 0.8, the hybridization cannot induce a gap at the Fermi energy [97], and thus the DOS is always finite irrespective whether there is electron-phonon interaction or not. Consequently, the c-electrons are always metallic in the large V regime.

The absence of the Mott gap in the large V regime signals that the electron-phonon interaction effect is suppressed by the hybridization. Since the electron charge susceptibility is positively correlated with the U_{eff}, the suppression of the electron-phonon coupling effect is also reflected in the decrease of the charge susceptibility as V increases for fixed β (not shown). As V increases from 0.1 to 1.8, the localized f electron moments that are present at small V get screened by the conduction electrons when V is large [86]. At the same time, the conduction electrons make a transition from insulator to metal. The c-electron spectral functions for $\beta = 10$ and $U_{eff} = 1$ with varying values

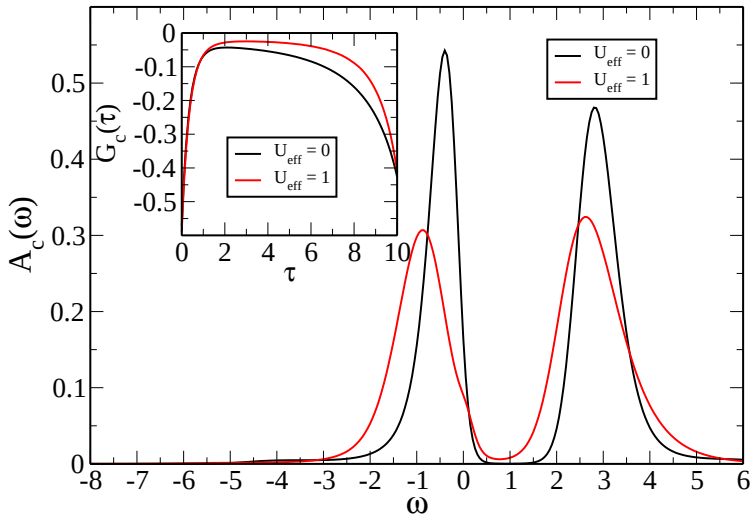

Figure 4.4: Main panel: The conduction electrons DOS for $U_{eff} = 0$ and $U_{eff} = 1$ when $V = 1.8, \beta = 10$, $\Omega_0 = 0.01$. Here, the introduction of the electron-phonon interaction has no significant influence on the DOS, which at the Fermi energy is always finite whether there is electron-phonon interaction or not. Inset: The $G_c(\tau)$ for small and large electron-phonon interaction strength.

of V are shown in Fig. 4.5, where a gap at the Fermi energy is clearly visible for $V < 0.6$. When $V > 0.6$, the Mott gap evolves into a depression which disappears completely for $V > 1.2$. Therefore the Mott MIT is present only when the electron-phonon interaction is strong enough.

4.4 Conclusion

In conclusion, using the periodic Anderson model with phonons coupled to the conduction band, and by introducing a volume and temperature dependent bulk modulus contribution to the total pressure, we find a first order phase transition which can be identified as the $\gamma \rightarrow \alpha$ volume collapse transition of Cerium. We find that this phase transition is enhanced by the presence of the electron-phonon interaction which various experiments have shown to play an important role in the volume collapse process. Moreover, we find that our model, although originally conceived with the KVC

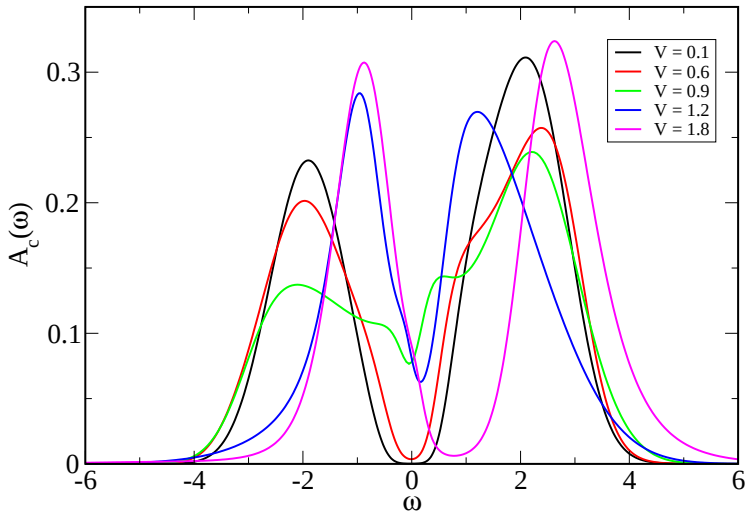

Figure 4.5: The c-electron spectral functions for $\beta = 10, \Omega_0 = 0.01, U_{eff} = 1$, at different values of V. When V is small (below 0.6), the electron-phonon interaction dominates over the Kondo screening, and the conduction electrons form a Mott insulator. When V gets large, the Kondo effect dominates over the electron-phonon interaction effect, and the conduction electrons become metallic.

scenario in mind, exhibits several interesting features of the Mott transition, e.g., a gap at the Fermi energy in the conduction electrons opens at low temperature, and this gap is proportional to the effective electron-phonon interaction, U_{eff}. Our numerical results show that this Mott transition observed in our model is probably continuous within our parameter regime.

Chapter 5

Competition Between Hybridization and the Electron-phonon Interaction in the PAM with Holstein Phonons

5.1 Introduction

The cerium volume collapse has been a long standing puzzle since its discovery more than 60 years ago [40]. At room temperature and under pressure of about 15,000 atmospheres the volume of cerium decreases by about 17%, while preserving its face-centered cubic crystal structure. This volume collapse, which is a first order iso-structural phase transition, has intrigued the physics community for a long time, and several theoretical scenarios have been proposed for its explanation. Up to now, two competing models have survived experimental scrutiny: the Mott transition scenario [46] and the Kondo volume collapse (KVC) [47] scenario.

In the Mott transition scenario, the outer shell electrons of cerium are divided into two groups, the *spd* electrons which form the conduction band and are just spectators of the volume collapse, and the $4f$ orbitals which play the central role in the $\gamma \rightarrow \alpha$ transition. This scenario assumes that the electronic properties of cerium can be captured by the Hubbard model, which is the simplest possible model including the competition between the hopping and the Coulomb repulsion between electrons. In the large volume γ phase, where the large lattice constant renders the hopping of the $4f$ from one site to its neighbor prohibitively expensive, the $4f$ electrons are assumed to be essentially localized. When the volume collapses, the lattice constant becomes smaller, thus making the hopping of the $4f$ electrons possible. Therefore, in the small volume α phase, we expect the $4f$ electrons to become delocalized. This localization-delocalization transition of the $4f$ electrons is reminiscent of the Mott metal-insulator transition in the Hubbard model [23, 24, 55, 56], and prompts Johansson [46] to propose the Mott transition scenario to explain some key aspects of the volume collapse such as the spectrum features in the γ and α phases [56].

In 1982, Allen and Martin proposed the Kondo volume collapse (KVC)[47] scenario based on the newly found exact solution of the Kondo problem using the Bethe ansatz. From the exact solution of the Kondo problem, the authors were able to obtain the explicit expression of the electronic free energy $F_K(T, J)$ as a function of the temperature T and the Kondo exchange interaction J. The Kondo temperature T_K in the α phase is much higher than that in the γ phase, due to the variation of the Kondo exchange energy J across the volume collapse transition. The authors assumed the following relation between J and unit cell volume $\mathcal{V}$: $J \propto \frac{1}{\mathcal{V}^6}$. Through this relation, the electronic free energy captures the volume dependence. The authors further introduce the mechanical energy due to the bulk modulus. Combining the electronic and the mechanical energy, the authors were able to obtain the iso-thermal pressure versus volume curves by taking the partial derivative of the free energy with respect to the volume at constant temperature. They showed that when the temperature is below some critical value T_c, the pressure versus volume curve develops a kink structure which is an indicator of the emergence of a first order phase transition. This first order transition is then identified as the $\gamma - \alpha$ transition in Cerium.

In a previous paper, we have shown that by introducing a temperature and volume dependent bulk modulus term, we can get a kink in the $p - \mathcal{V}$ diagram. Using the periodic Anderson model (PAM) with Holstein phonons, we found that the electron-phonon interaction can significantly enhance the $\gamma \rightarrow \alpha$ transition, which is consistent with the previous experimental results[52, 54]. We further studied the evolution of the conduction electron density of states (DOS), and found that this transition is actually a Mott metal-insulator transition driven by the electron-phonon interaction. Due to the electron-phonon interaction, this metal-insulator transition exhibits several features of the Mott transition[23, 24, 55], such as the opening of a gap at the Fermi energy in the conduction band electron spectral function, and the width of the gap is proportional to the effective electron-phonon interaction U_{eff}. We also noticed that this Mott transition from metal to insulator driven by the electron-phonon interaction is present only when the hybridization between the conduction electron and the localized electron is small. When the hybridization is large, the Kondo effect kicks in and the effects due to the electron-phonon interaction is strongly suppressed. This compels us to argue that there is a competition between the Kondo effect due to V and the Mott gap opening due to U_{eff}.

Here, we will study this competition effect further, by including the behavior of the $4f$ electron spectral functions and the results from the two-particle quantities, such as the charge susceptibility and the magnetic susceptibility. The evolution of the DOS of the c and f electrons with respect to the

relative strengths of V and U_{eff} also vividly illustrates this competition. The structure of the paper will be as follows. In section II, we introduce our model Hamiltonian, and give a brief introduction of the numerical methods we employed to solve this model. Section III presents the details of our results, including the c and f electron spectral functions and the two-particle quantities in different parameter regimes. We compare our results with the previous numerical renormalization group results in section IV. In section V, a schematic phase diagram summarizing our results is shown. Finally, we make our conclusion in section VI.

5.2 Model and Methods

Our model Hamiltonian is

$$\begin{aligned} \hat{H} &= \hat{H}_0 + \hat{H}_I \qquad (5.1) \\ \hat{H}_0 &= -t \sum_{\langle i,j\rangle,\sigma} (c^\dagger_{i,\sigma} c_{j,\sigma} + c^\dagger_{j,\sigma} c_{i,\sigma}) + \epsilon_f \sum_{j,\sigma} f^\dagger_{j,\sigma} f_{j,\sigma} \\ &\quad + V \sum_{i,\sigma} (c^\dagger_{i,\sigma} f_{i,\sigma} + f^\dagger_{i,\sigma} c_{i,\sigma}) + \sum_i \left(\frac{P_i^2}{2m} + \frac{1}{2} k X_i^2 \right) \\ \hat{H}_I &= U \sum_i n^f_{i,\uparrow} n^f_{i,\downarrow} + g \sum_{i,\sigma} n^c_{i,\sigma} X_i \,. \end{aligned}$$

Here, $c^\dagger_{i,\sigma}, c_{i,\sigma}(f^\dagger_{i,\sigma}, f_{i,\sigma})$ creates and destroys a $c(f)$ electron of spin σ at lattice site i, respectively. P_i and X_i are the phonon momentum and displacement operators. Here, we have used dispersionless Einstein phonons with frequency $\Omega_0 = \sqrt{k/m}$. The parameter g measures the electron-phonon interaction strength, U is the Hubbard repulsion between localized f-electrons, and V characterizes the hybridization between c- and f-electrons. From the parameters g, k, we construct the effective electron-phonon interaction strength, $U_{eff} = \frac{g^2}{2k}$. Throughout this paper and to be consistent with the experimental results, we have set $\Omega_0 = 0.01$ [86] unless otherwise specified. We also set $U = 4$, the c-electron filling number to 0.8, and the f-electron filling number to 1.0.

To solve this model, we use the dynamical mean field theory (DMFT)[69] with continuous time quantum Monte Carlo (CTQMC)[36] as our impurity solver. From the DMFT and CTQMC, we get the imaginary frequency Matsubara Green's function, from which we can extract the single-particle density of states (DOS) using the maximum entropy method(MEM)[37].

In DMFT, we map our model into a single impurity that is self-consistently embedded in an effective medium. Temporal correlations are retained, since the electrons can hop from the impurity

site to the medium and back, but spatial correlations are discarded. Nevertheless, DMFT becomes exact in the limit of infinite dimensions and accurately captures the physics of correlated electron systems even in three dimensions.

The effective medium is described by a bath Green's function, $G_0(i\omega_n)$, and the impurity site is described by the interacting Green function $G(i\omega_n)$. We use the CTQMC to solve the interacting impurity problem embedded in the bath. Once we have both $G(i\omega_n)$ and $G_0(i\omega_n)$, we use Dyson's equation to obtain the electron self-energy, that is

$$\Sigma(i\omega_n) = G_0^{-1}(i\omega_n) - G^{-1}(i\omega_n). \tag{5.2}$$

From the self energy, we calculate the lattice Green function $G_{\boldsymbol{k}}(i\omega_n)$ in momentum space. Self consistency is obtained once we impose the condition that the interacting Green's function is equal to the coarse grained momentum Green's function,

$$G(i\omega_n) = \langle G_{\boldsymbol{k}}(i\omega_n)\rangle_{\boldsymbol{k}}. \tag{5.3}$$

The DMFT+CTQMC yields the Matsubara Green's function in imaginary frequency space. However, we need to know the real-frequency Green's function to make direct comparisons with experiments. The Matsubara Green's function is related with the spectral function through the spectral representation

$$G(i\omega_n) = \int_{-\infty}^{\infty} \frac{A(\omega)}{i\omega_n - \omega} d\omega =: KA. \tag{5.4}$$

where we define the kernel function $K(i\omega_n, \omega) = \frac{1}{i\omega_n - \omega}$. The maximum entropy method enables us to calculate the spectral function from the mean value of the Matsubara Green's function and from the covariance matrix C which is calculated as

$$\begin{aligned} C_{mn} &= \frac{1}{N(N-1)} \\ &\times \sum_{i=1}^{N} \Big(G^{(i)}(i\omega_m) - \bar{G}(i\omega_m)\Big)^* \Big(G^{(i)}(i\omega_n) - \bar{G}(i\omega_n)\Big). \end{aligned} \tag{5.5}$$

Here, i is an index that enumerates the Monte Carlo bin numbers, and $\bar{G}$ is the mean value of the Matsubara Green's function. In maximum entropy method, we define a quantity $Q = \alpha S - \frac{1}{2}\chi^2$ that we try to maximize with respect to the spectral function $A(\omega)$. Here S is the entropy defined by $S = -\int d\omega A(\omega) \log A(\omega)/M(\omega)$, with $M(\omega)$ being a (usually) featureless model function and

$\chi^2 = (G - KA)^\dagger C^{-1}(G - KA)$. It can be shown that the Hessian matrix of Q with respect to $A(\omega)$ is always negative definite, and thus solution of the equation $\frac{\delta Q}{\delta A(\omega)} = 0$ gives us the $A(\omega)$ that can maximize Q, and thus can serve as our most probable spectral function given the Monte Carlo measurement results.

5.3 Results

We present the results for three parameter regimes. The first one is when the electron-phonon interaction is dominant in comparison with the hybridization. Then, we consider the case when the hybridization is comparable to the electron-phonon interaction, and finally when the hybridization dominates over the electron-phonon interaction. The competition between both interactions is noticeable in any of these three regions, and is especially obvious when the hybridization is comparable to the electron-phonon interaction.

5.3.1 Small hybridization

Fig. 5.1 illustrates the suppression of the Kondo effect due to the electron-phonon interaction for a small value of the hybridization ($V = 0.4$). When $U_{eff} = 0$ the c-electron spectral functions (top left panel of Fig. 5.1) are almost Gaussian for all the inverse temperatures displayed, while the f-electron spectral functions exhibit a Kondo resonance at low temperatures (lower left panel). Moreover, at even lower temperatures, the Kondo resonance splits, and a pseudo-gap develops[28, 97]. However, when $U_{eff} = 1$, the strong electron-phonon interaction induces a gap on the c-electron spectral function at low temperature (top right panel of Fig. 5.1). The depletion of the conduction electrons at the Fermi energy strongly suppresses the Kondo effect, and thus the Kondo peak in the f-electron spectral function is absent (bottom right panel) for all shown temperatures. Notice that when U_{eff} dominates over V, the filling number is not a single-valued function of the chemical potential at low temperature, and we are not able to explore temperatures lower than $\beta = 15$.

The competition between V and U_{eff} can also be noticed when we plot the time-integrated f-electron spin susceptibility, χ^{ff}, and the c-electron charge susceptibility, χ^{cc} (Fig. 5.2). For $V = 0.4$, the Kondo effect is pretty weak even when there are no phonons. Therefore, the f local moments are hardly screened by the conduction electrons, and χ^{ff} is large, for both $U_{eff} = 0$ and 1, which is shown in the main panel of Fig. 5.2. Although phonons do not alter significantly the f-electron spin susceptibility, they do largely influence the behavior of the c-electron charge susceptibility. The

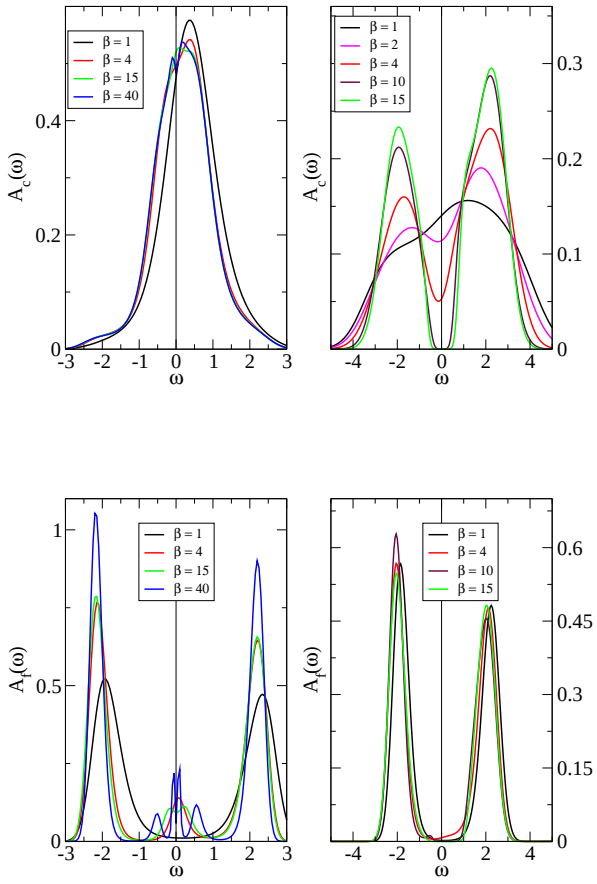

Figure 5.1: Comparison of the periodic Anderson model (PAM) and the PAM with Holstein phonons for $V = 0.4, U = 4, \Omega_0 = 0.01$. Top panels: c-electron spectral functions. Bottom panels: f-electron spectral functions. Left panels show data for the PAM ($U_{eff} = 0$) and several temperatures between $\beta = 1$ and 40. Right panels display data for $U_{eff} = 1$ and inverse temperatures between $\beta = 1$ and 15. Upper left panel: The c-electron spectral function of the PAM are almost Gaussian. Upper right panel: The electron-phonon interaction opens a Mott gap on the c-electron spectral function for $\beta > 10$. Lower left panel: A Kondo resonance develops for $\beta > 4$ in the f-electron spectral function. The Kondo resonance splits at the lowest temperatures. Lower right panel: The strong electron-phonon interaction suppresses the Kondo effect, only the two Hubbard bands appear.

inset of Fig. 5.2 displays a much larger χ^{cc} for $U_{eff} = 1$ than for $U_{eff} = 0$. This confirms that the charge fluctuations are large when the electron-phonon interaction is strong.

5.3.2 Intermediate hybridization

In this section, we set the hybridization $V = 1.2$ and still set the $U_{eff} = 1$ when we introduce the electron-phonon interactions. By doing this, we are studying the situation where the hybridization

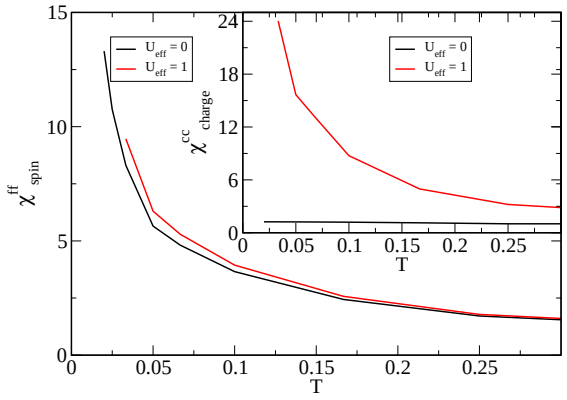

Figure 5.2: Susceptibilities versus temperature for $V = 0.4$. Main panel: The time integrated f-electron spin susceptibility. Notice that when U_{eff} increases the f-electron spin susceptibility also increases due to the reduced screening of the localized f-electrons. Inset: The c-electron charge susceptibility versus temperature. As U_{eff} increases the charge susceptibility increases since a larger U_{eff} results in stronger charge fluctuations, and thus a larger charge susceptibility.

V is comparable to U_{eff}, and thus we expect both Kondo effects and electron-phonon interaction effects to be present. When there is no electron-phonon interaction, the hybridization is strong enough to induce a hybridization gap in both the c electron spectral functions and the f electron spectral functions. When we introduce the electron-phonon interaction by setting $U_{eff} = 1$, the U_{eff} and the V begins to compete with each other, a competition that results in fine structures in both the c- and f-electron spectral functions. We see that U_{eff} weakens the hybridization gap induced by V, and V weakens the Mott gap induced by U_{eff}. The comparisons of the c and f electron spectral functions with and without electron-phonon interactions are plotted in Fig. 5.3. As shown in the figure, when there is no electron-phonon interaction, the hybridization V can easily induce a hybridization gap at relatively high temperature (The gap is already clearly visible when $\beta = 10$) in both the c and f electron spectral functions. The fact that the filling number of conduction electron is set to be 0.8 dictates the the hybridization gap does not open at the Fermi energy. When we introduce the electron-phonon interaction by setting $U_{eff} = 1$, we see a Mott gap opens in the conduction electron spectral function. However, compared to the previous section, the Mott gap opens at a much lower temperature than before. For $V = 0.4, U_{eff} = 1$, the Mott gap opens when $\beta = 10$, whereas here, the Mott gap opens when $\beta = 50$. Therefore, we see that as V increases, the Mott metal-insulator transition temperature decreases significantly.

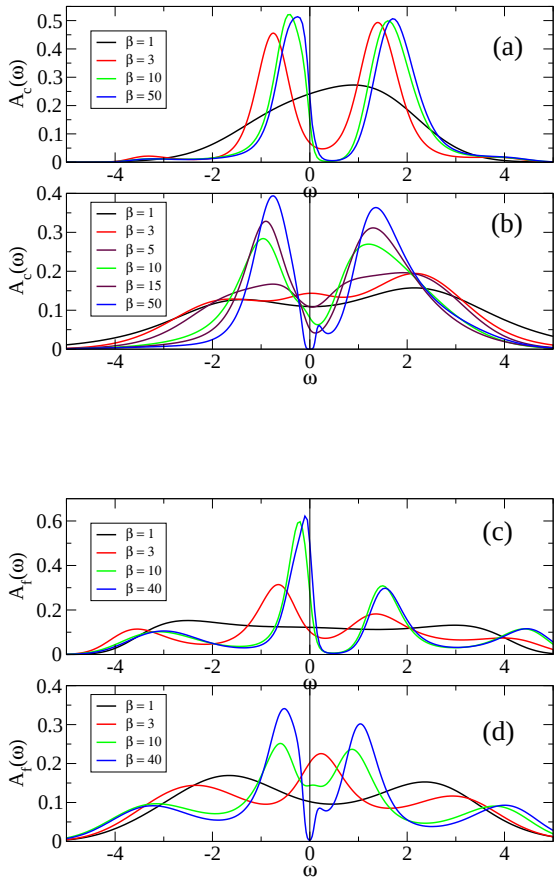

Figure 5.3: Figure panel (a): When $V = 1.2, U_{eff} = 0$, the strong hybridization induces a hybridization gap in the c electron spectral functions at low temperatures. Panel (b): When $V = 1.2, U_{eff} = 1$, the hybridization gap that is induced by V is strongly suppressed by the electron-phonon interaction. Panel (c): $V = 1.2, U_{eff} = 0$. The hybridization induces a gap slightly above the Fermi energy in the f electron spectral functions. Panel (d): $V = 1.2, U_{eff} = 1$. The hybridization effect is competing with the electron-phonon interactions.

In this parameter regime where the hybridization is comparable to the electron-phonon interaction, the competition between V and U_{eff} is more obvious than it is for $V = 0.4$. This strong competition is clearly captured by the behavior of the two-particle quantities. As shown in Fig. 5.4, when there are no phonons in the system, the f electron spin susceptibility χ^{ff} is very small. This is because for this value of V, the Kondo effect is pretty strong, and the localized f electron moments are almost fully screened by the conduction electrons. However, when $U_{eff} = 1$, the electron-phonon interaction is competing with Kondo effect, and thus the Kondo screening of the local moments by conduction electrons is significantly reduced, resulting in a much larger χ^{ff} compared to the case

when $U_{eff} = 0$. The charge fluctuations due to the electron-phonon interaction is also reflected in the c electron charge susceptibility χ^{cc}, the value of which is much larger when $U_{eff} = 1$ than when $U_{eff} = 0$. It is this strong charge fluctuation of the conduction band electrons that surpasses the Kondo effect.

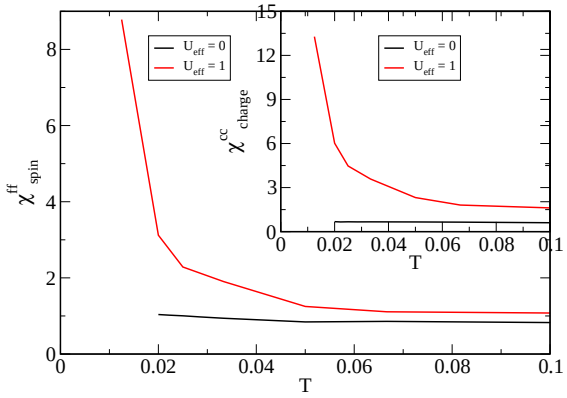

Figure 5.4: Susceptibilities versus temperature for $V = 1.2$. Main panel: The time integrated f electron spin susceptibility. Inset: The c electron charge susceptibility.

5.3.3 Large hybridization, with and without electron-phonon interaction

In this section, we will explore the region where the hybridization is strong. When hybridization is much larger than the effective electron-phonon interaction strength, the spectral functions of both c and f electrons mainly exhibit features due to the hybridization effect, and the effect due electron-phonon interaction, that is, the opening of a Mott gap at the Fermi energy, is suppressed by the hybridization effect. When we plot the spectral functions for $V = 1.8, U_{hub}$ with ($U_{eff} = 1$) and without ($U_{eff} = 0$) phonons, we find that the spectral functions do not differ from each other very much. This is because the electron-phonon interaction effect is dominated by the hybridization effect, and the presence or the absence of the electron-phonon dost not make a considerable difference. However, the electron-phohon interaction effect is still noticeable when the temperature is low enough. When $U_{eff} = 1$, a kink structure at the Fermi energy emerges in both the c electron spectral functions and f electron spectral functions at low temperature. This kink structure is due to the electron-phonon interaction which induces charge fluctuations in the conduction band electrons, since the kink becomes larger when we increase the value of U_{eff} from 0.9 to 1.1, as shown in Fig. 5.6. Moreover, from Fig. 5.6, where we plot the c electron charge susceptibilities χ^{cc}, we

see that the charge susceptibility becomes larger as U_{eff} increases. χ^{cc} is a measure of the strength of the charge fluctuations, and the monotonic increase of χ^{cc} with respect to U_{eff} corroborates our assertion that the kink in the spectral functions at the Fermi energy is due to the electron-phonon interactions.

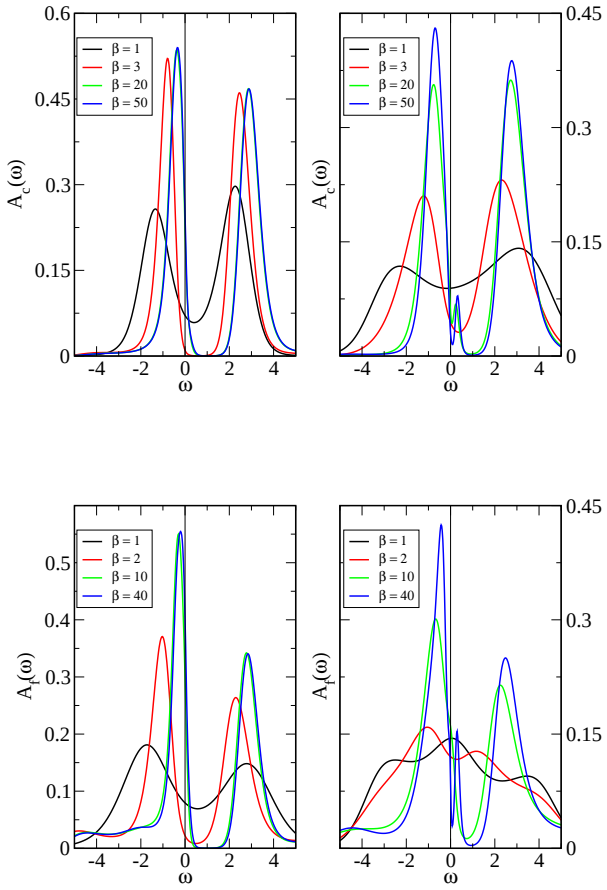

Figure 5.5: $V = 1.8, U_{hub} = 4$. Upper left panel: $U_{eff} = 0$. The strong hybridization generates a gap slightly above the Fermi energy in the c electron spectral functions. Upper right panel: c electron spectral function for $U_{eff} = 1$. Here, the hybridization dominates over electron-phonon interaction, and thus the spectral function still displays a strong hybridization gap. However, a kink structure at Fermi energy caused by U_{eff} is also visible. Lower left panel: f electron spectral function without phonons. Lower right panel: f electron spectral functions for $U_{eff} = 1$.

We further plot the f electron spin susceptibility χ^{ff} and c electron charge susceptibility χ^{cc} to study the competition between Kondo effect and electron-phonon interaction in this parameter regime. As shown in Fig. 5.7, the absence of the electron-phonon interaction renders both χ^{ff} and χ^{cc} negligibly small. This is because in the strong hybridization parameter regime, the Kondo

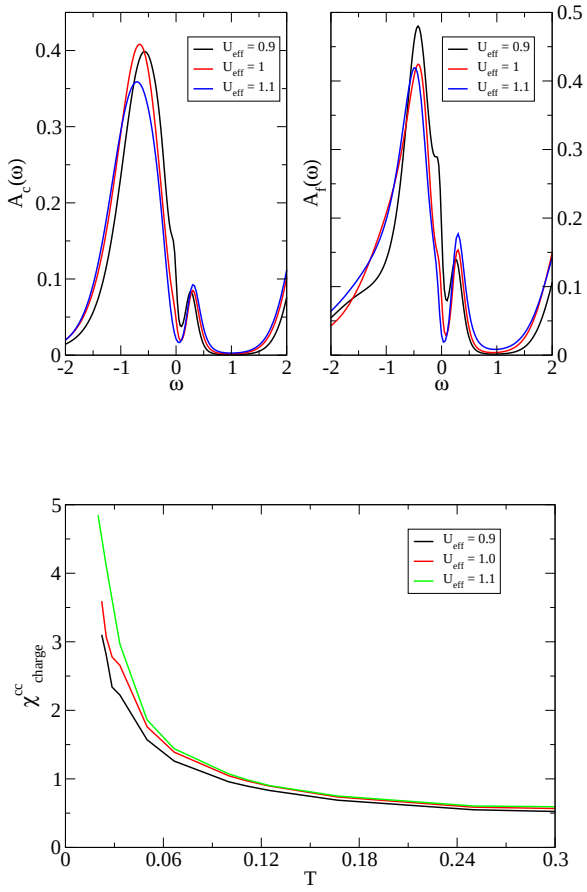

Figure 5.6: Upper left Panel: The spectral functions of c electrons for $V = 1.8, U_{hub} = 4, \beta = 40$, with different values of U_{eff}. Upper right panel: The f electron spectral functions with the same parameters as that in left panel. Lower panel: c electron charge susceptibilities versus T. χ^{cc} increases when U_{eff} gets large.

effect, when not frustrated by the electron-phonon interaction, is pretty effective in screening the local moments, thus making the χ^{ff} negligible. On the hand, when $U_{eff} = 1$, the Kondo effect is mildly suppressed by the electron-phonon interaction, and thus the χ^{ff}, which is an indicator of the presence of the localized f moments, becomes large. Moreover, the presence of the electron-phonon interaction gives rise to large charge fluctuations, and thus a larger χ^{cc}.

5.4 Comparison with NRG results

In Ref. [97], the authors measured the spectral function for f electrons in periodic Anderson model using numerical renormalization group (NRG) method at zero temperature. Here, we try to

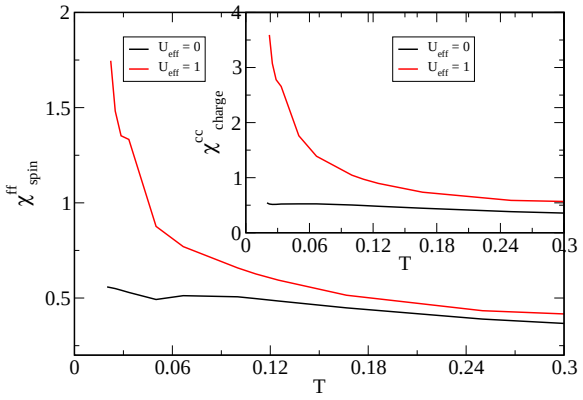

Figure 5.7: Susceptibilities versus temperature for $V = 1.8$. Main panel: The time integrated f electron spin susceptibility. Inset: The c electron charge susceptibility.

reproduce their results using QMC at finite temperature. It is found that for $n_c = 0.6, n_f = 1$ with $V^2 = 0.2, U_{hub} = 2$, when $\beta = 50$, the spectral functions of our results are in good agreement with results in Ref. [97]. The temperature evolution of the both c and f electron spectral functions are shown in Fig. 5.8. When the c filling is 0.6, the Kondo resonance in the f electron spectral function does not split into two peaks within the temperature range that we studied.

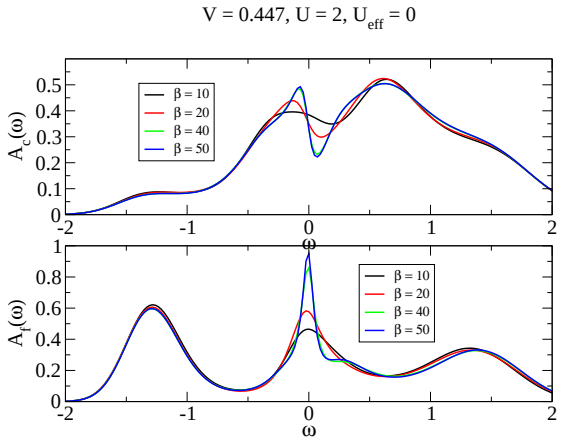

Figure 5.8: The c and f electron spectral functions for PAM with $V^2 = 0.2, U_{hub} = 2$. The c electron filling number is 0.6, and the f electron filling number is 1. The c electron spectral function develops a pseudo-gap slightly above Fermi energy and the f electron spectral function develops at Fermi energy a Kondo resonance which never splits, which is consistent with the results in Ref. [97].

5.5 Phase diagram

We have drawn a schematic phase diagram to illustrate the competition between V and U_{eff}. The phase diagram is drawn at low temperature. We have divided the phase diagram into four regions. Region I is for small V and small U_{eff}. In this region, the c electron spectral function is almost Gaussian, and the f electron spectral function displays two sharp Hubbard bands. Region II is for $U_{eff} \gg V$. Here, the electron-phonon interaction dominates over hybridization, and thus the Kondo effect is strongly suppressed. The c electron spectral function exhibits a Mott gap at the Fermi energy due to the electron-phonon interaction, and the f electron spectral function still contains two sharp Hubbard bands. Region III is for $V \gg U_{eff}$. Here, the Kondo effect dominates over electron-phonon interaction. The strong hybridization induces hybridization gaps for both c and f electron spectral functions. The Kondo resonance splits in this region at low temperature. Region IV is for $V \approx U_{eff}$. Here, the Kondo effect and the electron-phonon interaction competes with each other. The c electron spectral function displays a gap that has both Mott feature and hybridization feature. The Kondo effect can still be seen in the f electron spectral function, although the Kondo scale T_K is significantly reduced compared to the case when $U_{eff} = 0$.

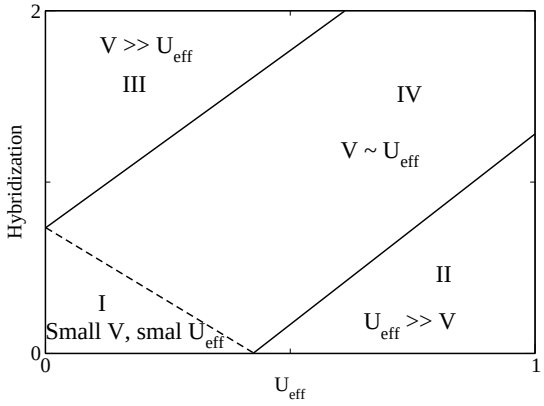

Figure 5.9: Schematic phase diagram for V vs. U_{eff}. There are four regions in the phase diagram, depending upon the ratio between V and U_{eff}. For each region, the c and f electron spectral functions are briefly depicted.

5.6 Conclusion

In this paper, we have studied the competition between the hybridization V and the electron-phonon interaction U_{eff} in our model. In the small hybridization regime, when the electron-phonon interaction is weak, the conduction c electron DOS is almost Gaussian, and the spectral function of the localized $4f$ electrons exhibits a weak Kondo peak. As the electron-phonon interaction gets stronger, the c electron spectral functions begin to develop a Mott gap, while the Kondo peak in the $4f$ electron spectral function is strongly suppressed. When the V is comparable to the U_{eff}, the competition effect between the Kondo effect and the electron-phonon effect is most obvious. In this parameter regime, both features of the Kondo effect and the electron-phonon effect are present, although reduced by each other. When $V \gg U_{eff}$, the Kondo effect dominates and the gap-opening phenomenon in the c electron spectra due to U_{eff} is absent. We make comparisons between our results obtained from QMC and the previous results obtained from NRG, and found that they are consistent. Finally, a schematic phase diagram illustrating this competition due to the variation of the relative strengths of V and U_{eff} is plotted.

Chapter 6

Two-particle Quantities

6.1 Introduction

Dynamical mean field theory (DMFT) is self-consistent in the one-particle level. As a result of this, only the phase transitions that can be described by the one-particle quantities can be explicitly seen in DMFT. For example, the Mott metal-insulator as described in Chapter 4 can be reflected by the value of the single particle density of states at the Fermi energy, and thus we can directly see the effect of this phase transition by having a critical slowing down as when approach the phase transition point. Here, the critical slowing down means that the number of iteration cycles that are required to have a convergent solution becomes very large near the critical point.

However, from the single particle Green's functions, we can also construct the two-particle Green's functions, or susceptibilities. By definition, the susceptibility is defined as the response of the systems to an external perturbing field when the external field approaches zero. When the temperature is above the transition temperature, the susceptibility is positive and well-behaved. As the temperature approaches the transition temperature from above, the susceptibility tends to increase rapidly. In DMFT, the susceptibility generally increases as $\chi \propto \frac{1}{T-T_c}$ when $T > T_c$, where T_c is the transition temperature. We can thus locate the transition point by plotting the inverse of the susceptibility versus temperature and find the point where the inverse of susceptibility becomes zero. Another way of locating the transition point is to calculate the the leading eigenvalue of the pairing matrix and find the temperature where the leading eigenvalue of the pairing matrix equals to 1. We call the eigenvalue that is closed to 1 the leading eigenvalue and the pairing matrix will be defined later. The two methods of locating the phase transition point are consistent with each other and can be used complementary evidences of a phase transition.

Although we can define the two particle Green's function and from its divergence point locate the phase transition temperature, we cannot claim that the phase transition that we find using this method really exists in the system, since the DMFT is one-particle level self-consistent and the

divergence of the two-particle quantities that we construct from the single-particle Green's function does not have an influence on the system we are studying. If we want to study the behavior of the system due to the phase transition that we found from the divergence of the susceptibility, we need to introduce the order parameter that can describe the existence of the phase, and calculate the order parameter self-consistently as a function of temperature. From the classical mean field theory, we know that above the transition temperature, the order parameter is zero and we only a have homogeneous phase. When the temperature drops below the critical value T_c, the order parameter becomes finite. By using this method, we also have a transition temperature, and this transition temperature should be the same as the transition temperature we found using the susceptibility if the theory is thermodynamically consistent. From the work of Gordon Baym and Leo P. Kadanoff, we know that a theory is thermodynamically self-consistent if the theory is Φ derivable[98]. Since the DMFT satisfies this criterion[69], we can thus find the transition temperature using either the susceptibility method or the order parameter method. However, in order to go below the transition temperature and see explicitly the effects of the phase transition, we can only use the order parameter method. On the other hand, we also go below the transition temperature without having a finite order parameter. This is like the super-cooled water case where we can still have liquid water phase even when the temperature is below zero. We can also easily frustrate the divergence of the susceptibility, and significantly reduce or even remove the phase transition temperature[13, 14] without affecting the single particle Green's function. Thus, we can say that the phase transition that is located from the two-particle Green's function is not as robust the phase transition that is found from the single-particle Green's function, and thus in many cases, we can safely go below the critical temperature which is identified from the divergence of the susceptibilities.

6.2 Bethe-Salpeter equation

In order to calculate the two-particle Green's functions, we need to use the Bethe-Salpeter equation. Like the Dyson's equation that is used to calculate the single-particle Green's function iteratively, the Bethe-Salpter equation also employs the iteration principle to calculate the two-particle Green's functions. In Dyson's equation, we use the single-particle self energy as the iteration core, and in the Bethe-Salpeter equation, we use the vertex function Γ as the iteration core. The Bethe-Salpeter

equation, which will be denoted BSE from now on, takes the form

$$\begin{aligned} \chi &= \chi_0 + \chi_0 \Gamma \chi \\ &= \chi_0 \Big(1 - \Gamma \chi_0\Big)^{-1} \end{aligned} \tag{6.1}$$

From the Eq. 6.2, we can define the pairing matrix $M = \Gamma\chi_0$. We can see that the divergence of χ is equivalent to the pairing matrix having an eigenvalue that is indistinguishable numerically from 1.

In order to find the phase transition point, we need to calculate the value of the lattice susceptibility $\chi_{\boldsymbol{k}}$. We make the assumption that the vertex function is independent of the momentum and can thus be calculated in the impurity site. The vertex function can be calculated from the Monte Carlo process using the formula $\Gamma = \chi_0^{-1} - \chi^{-1}$. Here, both χ and χ_0 are local quantities defined in the impurity site. With the vertex function, we can calculate the two-particle lattice Green functions $\chi_{\boldsymbol{k}}$ from the non-interacting lattice two-particle Green function $\chi^0_{\boldsymbol{k}}$. $\chi^0_{\boldsymbol{k}}$ can be calculated from the knowledge of the single-particle lattice Green function, which can in turn be calculated from the single-particle self energy. The self energy has already been calculated from the DMFT iteration cycles. Therefore, we can calculate the two-particle Green function following the above steps.

6.3 Frustration of the divergence

From the previous section, we can see that the lattice two-particle Green's function depends on the momentum only through the non-interacting two-particle lattice Green's function $\chi^0_{\boldsymbol{k}}$. In the single band model, $\chi^0_{\boldsymbol{q}} = \sum_{\boldsymbol{k}} G_{\boldsymbol{k}}(i\omega_n) G_{\boldsymbol{k}+\boldsymbol{q}}(i\omega_n)$, which can be further written as

$$\begin{aligned} \chi^0_{\boldsymbol{q}} &= \sum_{\boldsymbol{k}} \frac{1}{i\omega_n - \epsilon_{\boldsymbol{k}}} \frac{1}{i\omega_n - \epsilon_{\boldsymbol{k}+\boldsymbol{q}}} \\ &= \iint d\epsilon_1 d\epsilon_2 \frac{1}{i\omega_n - \epsilon_1} \frac{1}{i\omega_n - \epsilon_2} \sum_{\boldsymbol{k}} \delta(\epsilon_1 - \epsilon_{\boldsymbol{k}}) \delta(\epsilon_2 - \epsilon_{\boldsymbol{k}+\boldsymbol{q}}). \end{aligned} \tag{6.2}$$

Here, we can define the two-particle density of states (DOS) as

$$\Delta_{\boldsymbol{q}} = \sum_{\boldsymbol{k}} \delta(\epsilon_1 - \epsilon_{\boldsymbol{k}}) \delta(\epsilon_2 - \epsilon_{\boldsymbol{k}+\boldsymbol{q}}). \tag{6.3}$$

The form of the two-particle DOS depends on the dispersion relation. For the hyper-cubic lattice we are using, we have

$$\begin{aligned} \epsilon_{\boldsymbol{k}} &= t_1\epsilon_1(\boldsymbol{k}) + t_2\epsilon_2(\boldsymbol{k}) \\ \epsilon_1(\boldsymbol{k}) &= -\frac{2}{\sqrt{2D}}\sum_{n=1}^{D}\cos k_n \\ \epsilon_2(\boldsymbol{k}) &= -\frac{2}{\sqrt{2D}}\sum_{n=1}^{D}\cos 2k_n \end{aligned} \tag{6.4}$$

Now define:

$$\begin{aligned} t^2 &= t_1^2 + t_2^2 \\ t_1^{\star 2} &= \frac{t_1^2}{t^2}, t_2^{\star 2} = \frac{t_2^2}{t^2} \\ \eta_{\boldsymbol{q}} &= \frac{t_1^{\star 2}}{D}\sum_{n=1}^{D}\cos q_n + \frac{t_2^{\star 2}}{D}\sum_{n=1}^{D}\cos 2q_n \end{aligned} \tag{6.5}$$

DOS can be obtained through inverse Fourier transform

$$\Delta_{\boldsymbol{q}}(\epsilon_1,\epsilon_2) = \frac{1}{2\pi t^2\sqrt{1-\eta_{\boldsymbol{q}}^2}}\exp\Big(-\frac{\epsilon_1^2+\epsilon_2^2-2\eta_{\boldsymbol{q}}\epsilon_1\epsilon_2}{2t^2(1-\eta_{\boldsymbol{q}}^2)}\Big). \tag{6.6}$$

Therefore, all the momentum dependence of the two-particle Green's function comes from the momentum dependence of the two-particle DOS, which further comes from the single indicator $\eta_{\boldsymbol{q}}$. When $t_2 = 0$, the minimum of $\eta_{\boldsymbol{q}}$ is equal to -1 when the external momentum is equal to $(\pi, \pi, ..., \pi)$. However, when t_2 is finite, the minimum of $\eta_{\boldsymbol{q}}$ may deviate from -1, and the external momentum corresponding to the minimum may not be $(\pi, \pi, ..., \pi)$. By this, we say that the model is frustrated.

6.4 Frustration of CDW susceptibility in PAM+Holstein model

Here, we are only interested in the divergence of the lattice susceptibility, and minimization of $\eta_{\boldsymbol{q}}$ leads to maximization of lattice susceptibility. Therefore, we only use the minimum value of $\eta_{\boldsymbol{q}}$ while calculating lattice susceptibilities. For the hyper-cubic lattice that we are using, if only the nearest neighbor hopping is considered, then $\eta_{\boldsymbol{q}}$ reaches its minimum value that is -1 when lattice vector $\boldsymbol{Q} = (\pi, \pi, ..., \pi)$. However, if we also take into account the next-nearest neighbor hopping along the axis directions, then the minimum value that $\eta_{\boldsymbol{q}}$ can reach will deviate from -1, and the

maximum value that the minimum of η_q can reach is -1/2. The CDW transition temperature, which is identified when the inverse of CDW susceptibility is zero, decreases steadily as η_q shifts from -1 to -0.5. In Fig. 6.1, we plot the inverse of the hybridization susceptibility and the CDW susceptibility for different values of η_q together and see clearly that the CDW transition temperature is always higher than the hybridization critical point temperature that is identified as the point where the inverse of hybridization susceptibility extrapolates to zero.

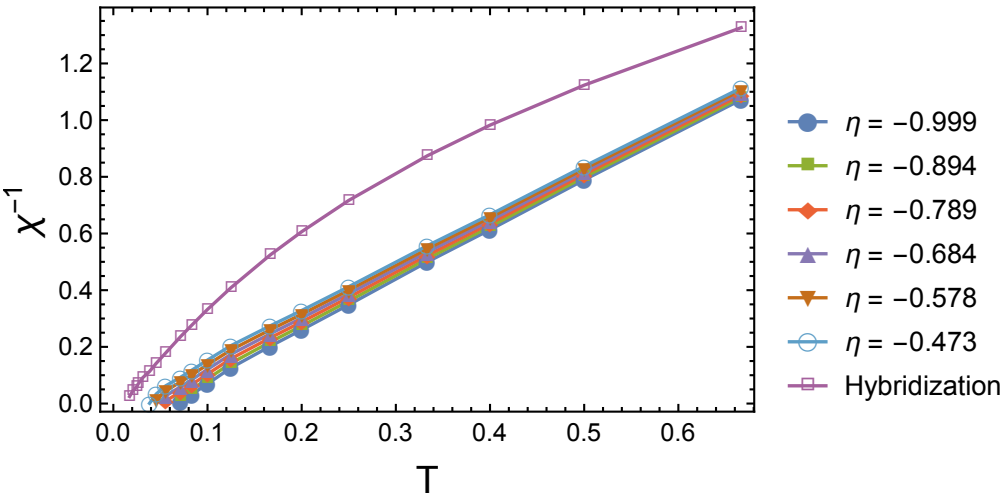

Figure 6.1: The inverse of the hybridization susceptibility and the CDW susceptibilities corresponding to different values of η_q. $U = 4, V = 0.955, U_{eff} = 1, \Omega_0 = 0.01$.

The CDW transition temperature varies as a function of η_q. We plot the transition temperature v.s. η_q in Fig. 6.2. As can be seen from Fig. 6.2, CDW transition temperature decreases as η_q

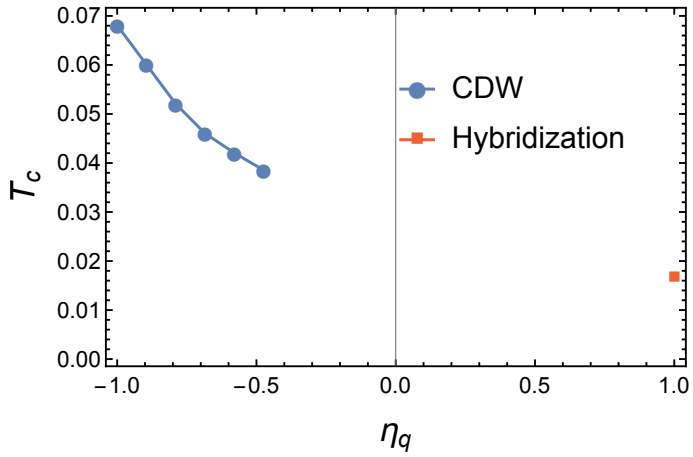

Figure 6.2: The CDW transition temperature and hybridization transition temperature versus η_q. $U = 4, V = 0.955, U_{eff} = 1, \Omega_0 = 0.01$.

shifts from -1 to -0.5. When $\eta_{\boldsymbol{q}} = -0.5$, the transition temperature is approximately $\beta = 25$, which is still much higher than the temperature corresponding to the critical point, which was identified as approximately $\beta = 60$[86].

6.5 Conclusion

We can see that the CDW susceptibility can be frustrated by introducing the next nearest neighbor hopping along the axis directions. This frustration mechanism is efficient in reducing the CDW transition temperature, but it cannot fully reduce the transition temperature to zero. Thus, we can go below the CDW transition temperature that is found when we only consider the nearest neighbor hopping. However, we need to be careful when the system temperature is much lower than the CDW transition temperature, since the CDW cannot be fully frustrated and thus its effect at extremely low temperature, especially at zero temperature, cannot be blatantly ignored.

Chapter 7

Conclusion

In conclusion, we have studied the periodic Anderson model (PAM) with Holstein phonons, and have used this model to try to elucidate the mechanism for the volume collapse observed in cerium. In order to solve this model, we have used the dynamical mean field theory (DMFT) with the continuous time quantum Monte Carlo (CTQMC) as our impurity solver.

In order to obtain the pressure-volume ($p-\mathcal{V}$) relation for cerium, we first calculate the free energy of the model using the formula $F = \int_0^N \mu dN$. To evaluate the integral numerically, we scan the chemical potential for fixed hybridization V and β, and solve the model to obtain the corresponding filing number. By plotting the chemical potential versus filling number, we can obtain the $\mu - N$ curve, and the area enclosed by this curve and the horizontal axis gives us the value of the free energy. Since we can calculate the free energy at fixed V, β, we can plot the free energy versus V for different values of β. Once we have the free energy versus V, we can calculate the electronic part of the pressure from the formula $p_e = -\frac{\partial F}{\partial \mathcal{V}}$. Besides the pressure due to the electrons, we also need to incorporate the pressure due to the bulk modulus. In order to faithfully represent the properties of the transition metals, we have taken into account of the experiential results by introducing the volume and temperature dependence of the bulk modulus. With the bulk modulus, we can obtain the mechanical part of the pressure due to the bulk modulus, which we denote as p_B. Combination of the electronic pressure and the bulk modulus pressure gives us the total pressure, which is $p = p_e + p_B$. What we found is that when we introduce the electron-phonon interaction, we can see a kink structure emerge at low temperature in the $p - \mathcal{V}$ diagram, which means we are seeing a first order phase transition. This first order phase transition can be identified as the $\gamma - \alpha$ volume collapse transition observed in cerium. However, when there is no electron-phonon interaction in our model, such a kink structure is absent. From this, we may conclude that the electron-phonon interaction can enhance the first order $\gamma - \alpha$ volume collapse phase transition. This is consistent with the experimental results and justifies our introduction of the electron-phonon interaction into our model.

We further studied the nature of the first order phase transition by plotting the evolution of the electron spectral functions with the V and the effective electron-phonon interaction strength U_{eff} as tuning parameters. When V is small, as we tune the U_{eff} from small to large, the conduction band electron spectral function evolves from an almost Gaussian to a curve with a Mott gap at the Fermi energy. This is a Mott metal-insulator transition (MIT) driven by the electron-phonon interaction. We also tried to determine the order of the metal-insulator transition by trying to obtain hysteresis loops in the $-\frac{1}{\pi}\mathrm{Im}G_c(i\pi T)$ versus U_{eff} plane. To get a hysteresis loop, we fix the chemical potential, start from a small U_{eff} when the system is metallic, run the program to obtain a convergent result, increase the U_{eff} by a small amount, and initialize the next U_{eff} from the previous U_{eff} results, continue this process until we reach a very large U_{eff} for which the system is known to be insulting, and then scan back from the large U_{eff} to the originally small U_{eff}. By completing this process, we have scanned the U_{eff} from small to large and then from large to small. Finally, we plot the $-\frac{1}{\pi}\mathrm{Im}G_c(i\pi T)$ versus U_{eff} to see if we can find any hysteresis loop which is an indicator of a first order phase transition. According to previous results, we know that for small phonon frequency Ω_0, it is currently beyond the numerical precision to tell whether the transition is first order or not. Thus, we have focused our attention on the parameter regime where Ω_0 is large. However, we found that even when the phonon frequency is pretty large, there is still no stable hysteresis loop in the $-\frac{1}{\pi}\mathrm{Im}G_c(i\pi T)$ versus U_{eff} plane. However, note that there may exist hysteresis loops at lower temperature, since previous results obtained from numerical renormalization group at zero temperature show that when the phonon frequency is larger than $0.05W$, where W is the conduction band width, there should be a first order metal-insulator transition. On example is shown in Fig. 7.1. Here, we have used a pretty large phonon frequency ($\Omega_0 = 20$), yet there is still no stable hysteresis loop in our program. This means we are either having a continuous metal-insulator transition or the temperature is not low enough and thus what we are seeing is just a smooth crossover from metal to insulator. Furthermore, when we dope the system away from half-filling, the discontinuous Mott transition would be strongly suppressed, thus making the prospect of finding a hysteresis loop even bleaker. Although the results of the large frequency regime are non-conclusive, we believe that the metal-insulator transition at small frequency limit is continuous or at most extremely weakly discontinuous. We held this belief due to the fact it is already shown that the Faclicov-Kimball model, to which the static ($\Omega_0 = 0$) Holstein model can be mapped, should show a continuous Mott transition when the filling number is non-trivial (The filling number is neither empty nor completely full). Considering these two limits, we do not anticipate to observe a first order Mott transition

in our model when the c electron filling number is set to 0.8, away from half-filling, and the bare phonon frequency is set to be 0.01, which is in close proximity to the Falicov-Kimball model.

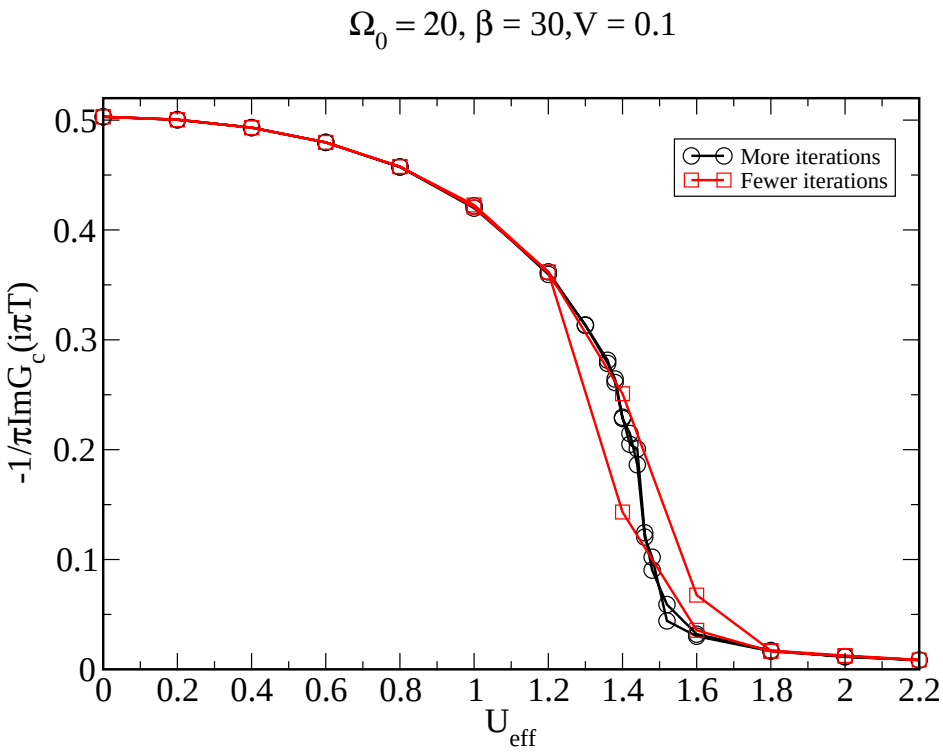

Figure 7.1: The hysteresis loop for $V = 0.1, \beta = 30, \Omega_0 = 20$. Here the phonon frequency is unphysically large, giving us an almost instantaneous attractive Hubbard model. This should be the parameter regime where it is easiest to obtain a hysteresis loop. Even for this parameter regime, a stable hysteresis loop is still non-existent. As shown in the figure, the red curve (hysteresis) was obtained when we used fewer iteration cycles in the DMFT calculation. However, once we increase the number of iterations, the original hysteresis loop shrinks to a single line within numerical error bars. This means we are either having a continuous Mott transition or a smooth crossover above the transition temperature.

We also study the evolution of the conduction electron spectral function with respect to V for fixed $U_{eff} = 1$. We found that the spectral function is metallic when V is large, and is insulating when V is small. This means we are having a metal-insulator transition when we change from the large V (small volume) regime to the small V (large volume) regime. We have already shown that the transition from the large volume phase to the small volume phase is a first order phase transition if we include the bulk modulus contribution, thus we can say that the transition exhibits several features of the Mott transition scenario, e.g., the opening of the Mott gap and the width of the Mott gap is proportional to the effective electron-phonon interaction.

We have seen that there is a competition between the hybridization and the electron-phonon interaction by studying the evolution of the conduction band electron spectral functions. This competition can be further proved if we consider the evolution of the f electron spectral functions and the two-particle quantities. From the f electron spectral functions, we found that when the hybridization is small but finite, when the $U_{eff} = 0$, the f spectral function exhibits a Kondo peak that splits at low temperature, which is consistent with the previous results for the PAM. However, when we set $U_{eff} = 1$, the Kondo peak disappears, indicating that the electron-phonon interaction can significantly reduce the hybridization effect. When the hybridization ($V = 1.2$) is comparable to $U_{eff} = 1$, both features of Kondo effect and the electron-phonon effects are present. For example, we can see the remnants of the Kondo peak in the f electron spectral function, and we can also see the remnants of the Mott gap in the conduction electron spectral function. When the hybridization is large ($V1.8$), the Kondo effect dominates over the electron-phonon interaction, and the Mott gap is absent in the c electron spectral function. The magnetic susceptibility of the f electrons can further illustrate this competition. When the $U_{eff} = 0$, the spin susceptibility is small; when the $U_{eff} = 1$, the spin susceptibility is large. This is because the electron-phonon interaction can reduce the Kondo effect, thus rendering the Kondo screening of the local f electron moments less effective. As a result, there are more local moments when there are electron-phonon interactions, and thus the f electron magnetic susceptibility is larger when $U_{eff} = 1$. This competition between the hybridization and the electron-phonon interaction is the driving force for the Mott metal-insulator transition in our model, which together with the bulk modulus contribution gives rise to the first order volume collapse transition observed in cerium.

References

[1] P. Coleman and A. J. Schofield, Nature **433**, 226 (2005).

[2] D. J. Griffiths, *Introduction to quantum mechanics* (Pearson Education India, 2005).

[3] N. W. Ashcroft, N. D. Mermin, and S. Rodriguez, *Solid state physics* (AAPT, 1978).

[4] H. K. Onnes, Commun. Phys. Lab. Univ. Leiden **12**, 1 (1911).

[5] H. Fröhlich, Phys. Rev. **79**, 845 (1950), URL `https://link.aps.org/doi/10.1103/PhysRev.79.845`.

[6] J. Bardeen, L. N. Cooper, and J. R. Schrieffer, Phys. Rev. **108**, 1175 (1957), URL `https://link.aps.org/doi/10.1103/PhysRev.108.1175`.

[7] A. A. Abrikosov, L. P. Gorkov, I. Dzyaloshinski, R. A. Silverman, and G. H. Weiss, *Methods of quantum field theory in statistical physics* (1964).

[8] N. F. Mott, Proceedings of the Physical Society. Section A **62**, 416 (1949).

[9] J. Hubbard, Proceedings of the Royal Society of London A: Mathematical, Physical and Engineering Sciences **276**, 238 (1963).

[10] E. H. Lieb and F. Y. Wu, Physical Review Letters **20**, 1445 (1968).

[11] E. H. Lieb and F. Wu, Physica A: statistical mechanics and its applications **321**, 1 (2003).

[12] W. Metzner and D. Vollhardt, Phys. Rev. Lett. **62**, 324 (1989), URL `http://link.aps.org/doi/10.1103/PhysRevLett.62.324`.

[13] E. Müller-Hartmann, Zeitschrift für Physik B Condensed Matter **74**, 507 (1989).

[14] E. Müller-Hartmann, Zeitschrift für Physik B Condensed Matter **76**, 211 (1989).

[15] M. Jarrell, Phys. Rev. Lett. **69**, 168 (1992), URL `http://link.aps.org/doi/10.1103/PhysRevLett.69.168`.

[16] J. Kondo, Progress of theoretical physics **32**, 37 (1964).

[17] L. Kouwenhoven and L. Glazman, Physics world **14**, 33 (2001).

[18] P. Anderson, Journal of Physics C: Solid State Physics **3**, 2436 (1970).

[19] K. G. Wilson, Physical review B **4**, 3174 (1971).

[20] K. G. Wilson, Rev. Mod. Phys. **47**, 773 (1975), URL `https://link.aps.org/doi/10.1103/RevModPhys.47.773`.

[21] H. R. Krishna-murthy, J. W. Wilkins, and K. G. Wilson, Phys. Rev. B **21**, 1003 (1980), URL `https://link.aps.org/doi/10.1103/PhysRevB.21.1003`.

[22] U. Schollwöck, Rev. Mod. Phys. **77**, 259 (2005), URL `https://link.aps.org/doi/10.1103/RevModPhys.77.259`.

[23] A. Georges and G. Kotliar, Phys. Rev. B **45**, 6479 (1992), URL `http://link.aps.org/doi/10.1103/PhysRevB.45.6479`.

[24] T. Pruschke, D. L. Cox, and M. Jarrell, Phys. Rev. B **47**, 3553 (1993), URL http://link.aps.org/doi/10.1103/PhysRevB.47.3553.

[25] A. Georges and W. Krauth, Physical Review B **48**, 7167 (1993).

[26] J. Freericks and V. Zlatić, Reviews of Modern Physics **75**, 1333 (2003).

[27] J. Freericks, M. Jarrell, and D. Scalapino, Physical Review B **48**, 6302 (1993).

[28] M. Jarrell, H. Akhlaghpour, and T. Pruschke, Phys. Rev. Lett. **70**, 1670 (1993), URL https://link.aps.org/doi/10.1103/PhysRevLett.70.1670.

[29] M. Jarrell, Phys. Rev. B **51**, 7429 (1995), URL http://link.aps.org/doi/10.1103/PhysRevB.51.7429.

[30] T. Maier, M. Jarrell, T. Pruschke, and M. H. Hettler, Reviews of Modern Physics **77**, 1027 (2005).

[31] M. Capone, L. de?Medici, and A. Georges, Physical Review B **76**, 245116 (2007).

[32] R. Bulla, T. Costi, and D. Vollhardt, Physical Review B **64**, 045103 (2001).

[33] J. E. Hirsch and R. M. Fye, Phys. Rev. Lett. **56**, 2521 (1986), URL https://link.aps.org/doi/10.1103/PhysRevLett.56.2521.

[34] E. Gull, A. J. Millis, A. I. Lichtenstein, A. N. Rubtsov, M. Troyer, and P. Werner, Reviews of Modern Physics **83**, 349 (2011).

[35] A. N. Rubtsov, V. V. Savkin, and A. I. Lichtenstein, Phys. Rev. B **72**, 035122 (2005), URL http://link.aps.org/doi/10.1103/PhysRevB.72.035122.

[36] F. F. Assaad and T. C. Lang, Phys. Rev. B **76**, 035116 (2007), URL http://link.aps.org/doi/10.1103/PhysRevB.76.035116.

[37] M. Jarrell and J. E. Gubernatis, Physics Reports **269**, 133 (1996).

[38] G. Kotliar and D. Vollhardt, Physics Today **57**, 53 (2004).

[39] A. Schiwek, F. Porsch, and W. Holzapfel, International Journal of High Pressure Research **22**, 407 (2002).

[40] A. W. Lawson and T.-Y. Tang, Phys. Rev. **76**, 301 (1949), URL http://link.aps.org/doi/10.1103/PhysRev.76.301.

[41] D. Parkinson, F. Simon, and F. Spedding, in *Proceedings of the Royal Society of London A: Mathematical, Physical and Engineering Sciences* (The Royal Society, 1951), vol. 207, pp. 137–155.

[42] A. Schuch and J. Sturdivant, Journal of Chemical Physics **18**, 145 (1950).

[43] J. Lock, Proceedings of the Physical Society. Section B **70**, 566 (1957).

[44] A. C. Hewson, *The Kondo problem to heavy fermions* (Cambridge university press, 1997).

[45] M. R. MacPherson, G. E. Everett, D. Wohlleben, and M. B. Maple, Phys. Rev. Lett. **26**, 20 (1971), URL https://link.aps.org/doi/10.1103/PhysRevLett.26.20.

[46] B. Johansson, Philosophical Magazine **30**, 469 (1974).

[47] J. W. Allen and R. M. Martin, Phys. Rev. Lett. **49**, 1106 (1982), URL http://link.aps.org/doi/10.1103/PhysRevLett.49.1106.

[48] N. R. James, S. Legvold, and F. H. Spedding, Phys. Rev. **88**, 1092 (1952), URL https://link.aps.org/doi/10.1103/PhysRev.88.1092.

[49] R. Beecroft and C. Swenson, Journal of Physics and Chemistry of Solids **15**, 234 (1960).

[50] E. Wuilloud, H. R. Moser, W. D. Schneider, and Y. Baer, Phys. Rev. B **28**, 7354 (1983), URL https://link.aps.org/doi/10.1103/PhysRevB.28.7354.

[51] M. E. Manley, R. J. McQueeney, B. Fultz, T. Swan-Wood, O. Delaire, E. A. Goremychkin, J. C. Cooley, W. L. Hults, J. C. Lashley, R. Osborn, et al., Phys. Rev. B **67**, 014103 (2003), URL https://link.aps.org/doi/10.1103/PhysRevB.67.014103.

[52] I.-K. Jeong, T. W. Darling, M. J. Graf, T. Proffen, R. H. Heffner, Y. Lee, T. Vogt, and J. D. Jorgensen, Phys. Rev. Lett. **92**, 105702 (2004), URL http://link.aps.org/doi/10.1103/PhysRevLett.92.105702.

[53] F. Decremps, D. Antonangeli, B. Amadon, and G. Schmerber, Phys. Rev. B **80**, 132103 (2009), URL https://link.aps.org/doi/10.1103/PhysRevB.80.132103.

[54] M. Krisch, D. Farber, R. Xu, D. Antonangeli, C. Aracne, A. Beraud, T.-C. Chiang, J. Zarestky, D. Y. Kim, E. I. Isaev, et al., Proceedings of the National Academy of Sciences **108**, 9342 (2011).

[55] M. Jarrell, Phys. Rev. Lett. **69**, 168 (1992), URL http://link.aps.org/doi/10.1103/PhysRevLett.69.168.

[56] K. Held, A. McMahan, and R. Scalettar, Phys. Rev. Lett. **87**, 276404 (2001).

[57] P. Wiegmann, Journal of Physics C: Solid State Physics **14**, 1463 (1981).

[58] N. Andrei, Physical Review Letters **45**, 379 (1980).

[59] N. Andrei, K. Furuya, and J. Lowenstein, Reviews of modern physics **55**, 331 (1983).

[60] L. Z. Liu, J. W. Allen, O. Gunnarsson, N. E. Christensen, and O. K. Andersen, Phys. Rev. B **45**, 8934 (1992), URL http://link.aps.org/doi/10.1103/PhysRevB.45.8934.

[61] W. E. Pickett, A. J. Freeman, and D. D. Koelling, Phys. Rev. B **23**, 1266 (1981), URL http://link.aps.org/doi/10.1103/PhysRevB.23.1266.

[62] B. I. Min, H. J. F. Jansen, T. Oguchi, and A. J. Freeman, Phys. Rev. B **34**, 369 (1986), URL http://link.aps.org/doi/10.1103/PhysRevB.34.369.

[63] W. L. McMillan, Phys. Rev. **167**, 331 (1968), URL http://link.aps.org/doi/10.1103/PhysRev.167.331.

[64] A. K. McMahan, K. Held, and R. T. Scalettar, Phys. Rev. B **67**, 075108 (2003), URL http://link.aps.org/doi/10.1103/PhysRevB.67.075108.

[65] A. P. Murani, Z. A. Bowden, A. D. Taylor, R. Osborn, and W. G. Marshall, Phys. Rev. B **48**, 13981 (1993), URL http://link.aps.org/doi/10.1103/PhysRevB.48.13981.

[66] A. V. Nikolaev and A. V. Tsvyashchenko, Physics-Uspekhi **55**, 657 (2012).

[67] R. Grover, I. C. Getting, and G. C. Kennedy, Phys. Rev. B **7**, 567 (1973), URL http://link.aps.org/doi/10.1103/PhysRevB.7.567.

[68] B. J. Baer, H. Cynn, V. Iota, C.-S. Yoo, and G. Shen, Phys. Rev. B **67**, 134115 (2003), URL http://link.aps.org/doi/10.1103/PhysRevB.67.134115.

[69] A. Georges, G. Kotliar, W. Krauth, and M. J. Rozenberg, Rev. Mod. Phys. **68**, 13 (1996), URL http://link.aps.org/doi/10.1103/RevModPhys.68.13.

[70] R. Bulla, T. A. Costi, and T. Pruschke, Rev. Mod. Phys. **80**, 395 (2008), URL https://link.aps.org/doi/10.1103/RevModPhys.80.395.

[71] G. D. Mahan, *Many-particle physics* (Springer Science & Business Media, 2013).

[72] P. Coleman, *Introduction to many-body physics* (Cambridge University Press, 2015).

[73] J. Skilling and R. Bryan, Monthly notices of the royal astronomical society **211**, 111 (1984).

[74] R. Bryan, European Biophysics Journal **18**, 165 (1990).

[75] K. Huang, *Statistical mechanics* (1963).

[76] K. Mikelsons, E. Khatami, D. Galanakis, A. Macridin, J. Moreno, and M. Jarrell, Phys. Rev. B **80**, 140505 (2009), URL http://link.aps.org/doi/10.1103/PhysRevB.80.140505.

[77] F. F. Assaad and T. C. Lang, Phys. Rev. B **76**, 035116 (2007), URL http://link.aps.org/doi/10.1103/PhysRevB.76.035116.

[78] K. Held, C. Huscroft, R. Scalettar, and A. McMahan, Phys. Rev. Lett. **85**, 373 (2000).

[79] C. R. Burr and S. Ehara, Phys. Rev. **149**, 551 (1966), URL http://link.aps.org/doi/10.1103/PhysRev.149.551.

[80] F. Decremps, D. Antonangeli, B. Amadon, and G. Schmerber, Phys. Rev. B **80**, 132103 (2009), URL http://link.aps.org/doi/10.1103/PhysRevB.80.132103.

[81] B. Amadon, S. Biermann, A. Georges, and F. Aryasetiawan, Phys. Rev. Lett. **96**, 066402 (2006), URL http://link.aps.org/doi/10.1103/PhysRevLett.96.066402.

[82] N. Lanatà, Y.-X. Yao, C.-Z. Wang, K.-M. Ho, J. Schmalian, K. Haule, and G. Kotliar, Phys. Rev. Lett. **111**, 196801 (2013), URL https://link.aps.org/doi/10.1103/PhysRevLett.111.196801.

[83] B. Amadon, Journal of Physics: Condensed Matter **24**, 075604 (2012).

[84] B. Amadon and A. Gerossier, Phys. Rev. B **91**, 161103 (2015), URL https://link.aps.org/doi/10.1103/PhysRevB.91.161103.

[85] B. Amadon, Phys. Rev. B **94**, 115148 (2016), URL https://link.aps.org/doi/10.1103/PhysRevB.94.115148.

[86] P. Zhang, P. Reis, K.-M. Tam, M. Jarrell, J. Moreno, F. Assaad, and A. K. McMahan, Phys. Rev. B **87**, 121102 (2013), URL http://link.aps.org/doi/10.1103/PhysRevB.87.121102.

[87] R. Podloucky and D. Glötzel, Phys. Rev. B **27**, 3390 (1983), URL http://link.aps.org/doi/10.1103/PhysRevB.27.3390.

[88] A. McMahan, C. Huscroft, R. Scalettar, and E. Pollock, Journal of Computer-Aided Materials Design **5**, 131 (1998).

[89] J. R. Schrieffer and P. A. Wolff, Phys. Rev. **149**, 491 (1966), URL http://link.aps.org/doi/10.1103/PhysRev.149.491.

[90] F. Murnaghan, Proceedings of the National Academy of Sciences **30**, 244 (1944).

[91] P. Yu, R. Wang, D. Zhao, and H. Bai, Applied Physics Letters **91**, 201911 (2007).

[92] K. Moore, L. Belhadi, F. Decremps, D. Farber, J. Bradley, F. Occelli, M. Gauthier, A. Polian, and C. Aracne-Ruddle, Acta Materialia **59**, 6007 (2011).

[93] D. Meyer, A. Hewson, and R. Bulla, Phys. Rev. Lett. **89**, 196401 (2002).

[94] Q. Si, G. Kotliar, and A. Georges, Phys. Rev. B **46**, 1261 (1992), URL https://link.aps.org/doi/10.1103/PhysRevB.46.1261.

[95] P. Werner and A. J. Millis, Phys. Rev. B **75**, 085108 (2007), URL https://link.aps.org/doi/10.1103/PhysRevB.75.085108.

[96] G. Sordi, K. Haule, and A.-M. S. Tremblay, Phys. Rev. Lett. **104**, 226402 (2010), URL https://link.aps.org/doi/10.1103/PhysRevLett.104.226402.

[97] T. Pruschke, R. Bulla, and M. Jarrell, Phys. Rev. B **61**, 12799 (2000).

[98] G. Baym and L. P. Kadanoff, Phys. Rev. **124**, 287 (1961), URL https://link.aps.org/doi/10.1103/PhysRev.124.287.

[99] M. Peskin and D. Schroeder, *An introduction to quantum field theory* (1995).

Appendix A

Calculation of the Total Energy

Here, in this appendix, we are going to show how to calculate the total energy from the knowledge of the Green function. In this chapter, the path integral formulation of the many body theory will be employed. For more details about the path integral methods used in this chapter, see Ref. [72, 99].

A.1 Path integral formulation of our model and integration out the phonons

Our model Hamiltonian in momentum space is

$$\begin{aligned}
\hat{H} &= \hat{H}_0 + \hat{H}_I \\
\hat{H}_0 &= \sum_{\boldsymbol{k},\sigma} \begin{pmatrix} \hat{c}^\dagger_{\boldsymbol{k}\sigma} & \hat{f}^\dagger_{\boldsymbol{k}\sigma} \end{pmatrix} \cdot \begin{pmatrix} \epsilon_{\boldsymbol{k}} & V \\ V & \epsilon_f \end{pmatrix} \cdot \begin{pmatrix} \hat{c}_{\boldsymbol{k}\sigma} \\ \hat{f}_{\boldsymbol{k}\sigma} \end{pmatrix} + \sum_{\boldsymbol{k}} \omega_0 \hat{a}^\dagger_{\boldsymbol{k}} \hat{a}_{\boldsymbol{k}} \\
\hat{H}_I &= \sum_{\boldsymbol{kq}\sigma} g \hat{c}^\dagger_{\boldsymbol{k}+\boldsymbol{q},\sigma} \hat{c}_{\boldsymbol{k}\sigma} \hat{\phi}_{\boldsymbol{q}} + U \sum_{\boldsymbol{kpq}} \hat{f}^\dagger_{\boldsymbol{p}\uparrow} \hat{f}_{\boldsymbol{k}\uparrow} \hat{f}^\dagger_{\boldsymbol{q}\downarrow} \hat{f}_{\boldsymbol{p}+\boldsymbol{q}-\boldsymbol{k},\downarrow} \\
\hat{\phi}_{\boldsymbol{q}} &= \hat{a}_{\boldsymbol{q}} + \hat{a}^\dagger_{-\boldsymbol{q}}
\end{aligned} \tag{A.1}$$

We are going to use the path integral method to integrate out the phonons and obtain a Hamiltonian which includes the retarded density-density interactions between the electrons. From this Hamiltonian, we can calculate the total energy of the system. With path integrals, the partition function can be written as

$$Z = \int \mathcal{D}[\bar{c}, c]\mathcal{D}[\bar{f}, f]\mathcal{D}[\bar{a}, a] e^{-S} \tag{A.2}$$

Here, S is the action which is

$$\begin{aligned} S &= \int_0^\beta d\tau \sum_{\boldsymbol{k},\sigma} \begin{pmatrix} \bar{c}_{\boldsymbol{k}\sigma} & \bar{f}_{\boldsymbol{k}\sigma} \end{pmatrix} \cdot \begin{pmatrix} \partial_\tau + \epsilon_{\boldsymbol{k}} & V \\ V & \partial_\tau + \epsilon_f \end{pmatrix} \cdot \begin{pmatrix} c_{\boldsymbol{k}\sigma} \\ f_{\boldsymbol{k}\sigma} \end{pmatrix} \\ &+ \int_0^\beta d\tau \sum_{\boldsymbol{k}} \bar{a}_{\boldsymbol{k}}(\partial_\tau + \omega_0) a_{\boldsymbol{k}} + \int_0^\beta d\tau \sum_{\boldsymbol{kq}\sigma} g \bar{c}_{\boldsymbol{k}+\boldsymbol{q},\sigma} c_{\boldsymbol{k}\sigma}(a_{\boldsymbol{q}} + \bar{a}_{-\boldsymbol{q}}) \\ &- U \int_0^\beta d\tau \sum_{\boldsymbol{kpq}} \bar{f}_{\boldsymbol{p}\uparrow} \bar{f}_{\boldsymbol{q}\downarrow} f_{\boldsymbol{k}\uparrow} f_{\boldsymbol{p}+\boldsymbol{q}-\boldsymbol{k},\downarrow} \end{aligned} \tag{A.3}$$

The part of the action that involves the phonons is

$$S_\phi = \int_0^\beta d\tau \sum_{\boldsymbol{k}} \bar{a}_{\boldsymbol{k}}(\partial_\tau + \omega_0) a_{\boldsymbol{k}} + \int_0^\beta d\tau \sum_{\boldsymbol{kq}\sigma} g \bar{c}_{\boldsymbol{k}+\boldsymbol{q},\sigma} c_{\boldsymbol{k}\sigma}(a_{\boldsymbol{q}} + \bar{a}_{-\boldsymbol{q}}) \tag{A.4}$$

Integrating out the phonons yields

$$\begin{aligned} Z_{eff} &= \int \mathcal{D}[\bar{a}, a] e^{-S_\phi} \\ &= Z_{\text{Bare\_phonons}} \exp\left(- \sum_{\boldsymbol{q},m} \bar{J}_{\boldsymbol{q},m} \frac{1}{i\nu_m - \omega_0} J_{\boldsymbol{q},m} \right) \end{aligned} \tag{A.5}$$

Here, the partition function for bare phonons is

$$Z_{\text{Bare\_phonons}} = \prod_{\boldsymbol{q}} \frac{1}{1 - e^{-\beta\omega_0}}, \tag{A.6}$$

and the current $J_{\boldsymbol{q},m}$ is defined as

$$\begin{aligned} J_{\boldsymbol{q},m} &= \beta^{-1/2} g \sum_{\boldsymbol{k},\sigma} \sum_{i\omega_n} \bar{c}_{\boldsymbol{k}-\boldsymbol{q},\sigma}(i\omega_n - i\nu_m) c_{\boldsymbol{k},\sigma}(i\omega_n) \\ &= g\beta^{-1/2} \int_0^\beta d\tau e^{i\nu_m \tau} \sum_{\boldsymbol{k},\sigma} \bar{c}_{\boldsymbol{k}-\boldsymbol{q},\sigma}(\tau) c_{\boldsymbol{k},\sigma}(\tau) \end{aligned} \tag{A.7}$$

Its conjugate is

$$\bar{J}_{\boldsymbol{q},m} = g\beta^{-1/2} \int_0^\beta d\tau e^{-i\nu_m \tau} \sum_{\boldsymbol{k}\sigma} \bar{c}_{\boldsymbol{k}\sigma}(\tau) c_{\boldsymbol{k}-\boldsymbol{q}}(\tau) \tag{A.8}$$

After integrating out the phonons, we have an effective action

$$S_{eff} = \sum_{\boldsymbol{q},m} \bar{J}_{\boldsymbol{q},m} \frac{1}{i\nu_m - \omega_0} J_{\boldsymbol{q},m} \tag{A.9}$$

An important property of $J_{\boldsymbol{q},m}$ is that $J_{-\boldsymbol{q},-m} = \bar{J}_{\boldsymbol{q},m}$. Thus, the effective action can be rewritten as

$$\begin{aligned} S_{eff} &= \sum_{\boldsymbol{q},m} \bar{J}_{\boldsymbol{q},m} \frac{1}{i\nu_m - \omega_0} J_{\boldsymbol{q},m} \\ &= \sum_{-\boldsymbol{q},-m} \bar{J}_{-\boldsymbol{q},-m} \frac{1}{-i\nu_m - \omega_0} J_{-\boldsymbol{q},-m} \\ &= \sum_{\boldsymbol{q},m} J_{\boldsymbol{q},m} \frac{1}{-i\nu_m - \omega_0} \bar{J}_{\boldsymbol{q},m} \\ &= \sum_{\boldsymbol{q},m} \bar{J}_{\boldsymbol{q},m} \frac{1}{-i\nu_m - \omega_0} J_{\boldsymbol{q},m} \\ &= \frac{1}{2} \sum_{\boldsymbol{q},m} \bar{J}_{\boldsymbol{q},m} \frac{-2\omega_0}{\omega_0^2 - (i\nu_m)^2} J_{\boldsymbol{q},m} \end{aligned} \tag{A.10}$$

Fourier transforming back to τ space, we have

$$S_{eff} = \frac{1}{2} g^2 \sum_{\boldsymbol{q}} \int_0^\beta d\tau_1 \int_0^\beta d\tau_2 \sum_{\boldsymbol{k},\sigma} \bar{c}_{\boldsymbol{k},\sigma}(\tau_1) c_{\boldsymbol{k}-\boldsymbol{q},\sigma}(\tau_1) D^0(\tau_1 - \tau_2) \sum_{\boldsymbol{p},s} \bar{c}_{\boldsymbol{p}-\boldsymbol{q},s}(\tau_2) c_{\boldsymbol{p},s}(\tau_2) \tag{A.11}$$

Here, we have introduced the bare phonon propagator in the effective action,

$$\begin{aligned} D^0(\tau_1 - \tau_2) &= \frac{1}{\beta} \sum_{i\nu_m} \frac{2\omega_0}{(i\nu_m)^2 - \omega_0^2} e^{-i\nu_m(\tau_1 - \tau_2)} \\ &= -\frac{1}{1 - e^{-\beta\omega_0}} (e^{-\omega_0|\tau_1 - \tau_2|} + e^{-(\beta - |\tau_1 - \tau_2|)\omega_0}) \end{aligned} \tag{A.12}$$

The effective action S_{eff} represents the time-retarded density-density interaction between two c electrons mediated by the exchange of a virtual phonon. This interaction differs from the instantaneous Hubbard interaction not only in that it is time-retarded, but also in that the spins of the two electrons do not have to be opposite, as required for on-site Hubbard interactions.

With this observation, the original partition function can be recast into the form

$$Z = Z_{\text{Bare\_phonons}} \int \mathcal{D}[\bar{c}, c] \mathcal{D}[\bar{f}, f] e^{-S}, \tag{A.13}$$

where, the action is

$$
\begin{aligned}
S &= \int_0^\beta d\tau \sum_{\boldsymbol{k},\sigma} \begin{pmatrix} \bar{c}_{\boldsymbol{k}\sigma} & \bar{f}_{\boldsymbol{k}\sigma} \end{pmatrix} \cdot \begin{pmatrix} \partial_\tau + \epsilon_{\boldsymbol{k}} & V \\ V & \partial_\tau + \epsilon_f \end{pmatrix} \cdot \begin{pmatrix} c_{\boldsymbol{k}\sigma} \\ f_{\boldsymbol{k}\sigma} \end{pmatrix} \\
&+ \frac{1}{2} g^2 \sum_{\boldsymbol{q}} \int_0^\beta d\tau_1 \int_0^\beta d\tau_2 \sum_{\boldsymbol{k},\sigma} \bar{c}_{\boldsymbol{k},\sigma}(\tau_1) c_{\boldsymbol{k}-\boldsymbol{q},\sigma}(\tau_1) D^0(\tau_1 - \tau_2) \sum_{\boldsymbol{p},s} \bar{c}_{\boldsymbol{p}-\boldsymbol{q},s}(\tau_2) c_{\boldsymbol{p},s}(\tau_2) \\
&- U \int_0^\beta d\tau \sum_{\boldsymbol{kpq}} \bar{f}_{\boldsymbol{p}\uparrow} \bar{f}_{\boldsymbol{q}\downarrow} f_{\boldsymbol{k}\uparrow} f_{\boldsymbol{p}+\boldsymbol{q}-\boldsymbol{k},\downarrow}
\end{aligned} \tag{A.14}
$$

A.2 The effective Hamiltonian obtained from the effective action S_{eff}

The effective Hamiltonian describing the retarded density-density electron interaction can be obtained by taking the derivative of S_{eff} with respect to β, that is,

$$
\begin{aligned}
H_{eff} &= \frac{\partial S_{eff}}{\partial \beta} \\
&= \frac{g^2}{2} \sum_{\boldsymbol{q}} \sum_{\boldsymbol{k},\sigma} \bar{c}_{\boldsymbol{k},\sigma}(0) c_{\boldsymbol{k}-\boldsymbol{q},\sigma}(0) \int_0^\beta D^0(\tau_2) \sum_{\boldsymbol{p},s} \bar{c}_{\boldsymbol{p},s}(\tau_2) c_{\boldsymbol{p}+\boldsymbol{q},s}(\tau_2) d\tau_2 \\
&+ \frac{g^2}{2} \sum_{\boldsymbol{q}} \int_0^\beta d\tau_1 \sum_{\boldsymbol{k},\sigma} \bar{c}_{\boldsymbol{k},\sigma}(\tau_1) c_{\boldsymbol{k}-\boldsymbol{q},\sigma}(\tau_1) D^0(\tau_1) \sum_{\boldsymbol{p},s} \bar{c}_{\boldsymbol{p},s}(0) c_{\boldsymbol{p}+\boldsymbol{q},s}(0) \\
&+ \frac{g^2}{2} \sum_{\boldsymbol{q}} \int_0^\beta d\tau_1 \int_0^\beta d\tau_2 \sum_{\boldsymbol{k},\sigma} \sum_{\boldsymbol{p},s} \bar{c}_{\boldsymbol{k},\sigma}(\tau_1) c_{\boldsymbol{k}-\boldsymbol{q},\sigma}(\tau_1) \frac{\partial D^0(\tau_1 - \tau_2)}{\partial \beta} \bar{c}_{\boldsymbol{p},s}(\tau_2) c_{\boldsymbol{p}+\boldsymbol{q},s}(\tau_2)
\end{aligned} \tag{A.15}
$$

Here, we have taken advantage of the fact that $c(\beta) = -c(0)$, $D^0(\tau - \beta) = D^0(\tau)$ and $D^0(-\tau) = D^0(\tau)$. In order to get the Hamiltonian in operator notation, we are to rewrite the above effective Hamiltonian as

$$
\begin{aligned}
H_{eff} &= -\frac{g^2}{2} \sum_q \sum_{k,\sigma} \sum_{p,s} \int_0^\beta d\tau_2 \bar{c}_{k,\sigma}(0) \bar{c}_{p,s}(\tau_2) D^0(\tau_2) c_{k-q,\sigma}(0) c_{p+q,s}(\tau_2) \\
&- \frac{g^2}{2} \sum_q \sum_{k,\sigma} \sum_{p,s} \int_0^\beta d\tau_1 \bar{c}_{k,\sigma}(\tau_1) \bar{c}_{p,s}(0) D^0(\tau_1) c_{k-q,\sigma}(\tau_1) c_{p+q,s}(0) \\
&- \frac{g^2}{2} \sum_q \sum_{k,\sigma} \sum_{p,s} \int_0^\beta d\tau_1 \int_0^\beta d\tau_2 \bar{c}_{k,\sigma}(\tau_1) \bar{c}_{p,s}(\tau_2) \frac{\partial D^0(\tau_1 - \tau_2)}{\partial \beta} c_{k-q,\sigma}(\tau_1) c_{p+q,s}(\tau_2)
\end{aligned} \tag{A.16}
$$

In operator notation, the effective Hamiltonian would be

$$\begin{aligned}\hat{H}_{eff} &= -\frac{g^2}{2}\sum_q\sum_{k,\sigma}\sum_{p,s}\int_0^\beta d\tau_2 \hat{c}^\dagger_{k,\sigma}(0)\hat{c}^\dagger_{p,s}(\tau_2)D^0(\tau_2)\hat{c}_{k-q,\sigma}(0)\hat{c}_{p+q,s}(\tau_2) \\ &- \frac{g^2}{2}\sum_q\sum_{k,\sigma}\sum_{p,s}\int_0^\beta d\tau_1 \hat{c}^\dagger_{k,\sigma}(\tau_1)\hat{c}^\dagger_{p,s}(0)D^0(\tau_1)\hat{c}_{k-q,\sigma}(\tau_1)\hat{c}_{p+q,s}(0) \\ &- \frac{g^2}{2}\sum_q\sum_{k,\sigma}\sum_{p,s}\int_0^\beta d\tau_1\int_0^\beta d\tau_2 \hat{c}^\dagger_{k,\sigma}(\tau_1)\hat{c}^\dagger_{p,s}(\tau_2)\frac{\partial D^0(\tau_1-\tau_2)}{\partial\beta}\hat{c}_{k-q,\sigma}(\tau_1)\hat{c}_{p+q,s}(\tau_2)\end{aligned} \tag{A.17}$$

It turns out that this effective Hamiltonian is useless to us, since we cannot obtain the equation of motion from this Hamiltonian. Actually, when we integrate out the phonons to obtain a retarded interaction between electrons, we obtain a system that cannot be described by a Hamiltonian. Path integral formulation is just designed to deal with this case. Therefore, we will use the path integral method to derive the equation of the motion. But before we start using that method, we first need to show that the two methods can yield the same results when the system has both the Hamiltonian formulation and the path integral formulation.This is the subject of the next section.

A.3 Schwinger-Dyson equation method for the derivation of the equation of motion for a simplified Holstein model

Schwinger-Dyson equation is a method that furnishes us with the equation of motion of a system represented in path integrals. To see this, let us consider this simplified Holstein model.

$$\hat{H} = \epsilon\hat{c}^\dagger\hat{c} + \omega\hat{a}^\dagger\hat{a} + g\hat{c}^\dagger\hat{c}(\hat{a}+\hat{a}^\dagger) \tag{A.18}$$

The action for this model is

$$S = \int_0^\beta d\tau\Big(\bar{c}(\partial_\tau+\epsilon)c + \bar{a}(\partial_\tau+\omega)a + g\bar{c}c(a+\bar{a})\Big) \tag{A.19}$$

Definition of electron Green function is

$$\begin{aligned}G(\tau'-\tau) &= -\langle T\hat{c}(\tau')\hat{c}^\dagger(\tau)\rangle \\ &= -\frac{1}{Z}\int\mathcal{D}[\bar{c},c]\mathcal{D}[\bar{a},a]c(\tau')\bar{c}(\tau)e^{-S}\end{aligned} \tag{A.20}$$

Now we are going to derive the equation of motion for the electron's Green function using both operator notation and path integral formulation, and show that these two methods yield identical result.

A.3.1 Operator formulation

Take the derivative of Green function with respect to imaginary time, we have

$$\frac{\partial G(\tau',\tau)}{\partial \tau'} = -\delta(\tau'-\tau) + \epsilon\langle T\hat{c}(\tau')\hat{c}^\dagger(\tau)\rangle + g\langle T\hat{c}(\tau')\hat{\phi}(\tau')\hat{c}^\dagger(\tau)\rangle \tag{A.21}$$

That is,

$$(\partial_{\tau'} + \epsilon)G(\tau',\tau) = -\delta(\tau'-\tau) + g\langle T\hat{c}(\tau')\hat{\phi}(\tau')\hat{c}^\dagger(\tau)\rangle \tag{A.22}$$

A.3.2 Path integral formulation

For the derivation of equation of motion in the path integral formulation, we are to use the Schwinger-Dyson method. In this method, the Grassmann numbers c and $\bar{c}$ are replaced with the shifted ones, that is,

$$\begin{aligned} c \to c' &= c + \delta c, \\ \bar{c} \to \bar{c}' &= \bar{c} + \delta\bar{c}, \end{aligned} \tag{A.23}$$

and everything is expanded to first order in δc and $\delta\bar{c}$. Consider this quantity,

$$\int \mathcal{D}[\bar{c},c]\mathcal{D}[\bar{a},a]\bar{c}(\tau)e^{-S[\bar{c},c;\bar{a},a]} = \int \mathcal{D}[\bar{c}',c']\mathcal{D}[\bar{a},a]\bar{c}'(\tau)e^{-S[\bar{c}',c';\bar{a},a]} \tag{A.24}$$

The action S represented in $\bar{c}', c'$ is

$$\begin{aligned} S[\bar{c}',c';\bar{a},a] &= S[\bar{c},c;\bar{a},a] \\ &+ \int_0^\beta d\tau\Big(\delta\bar{c}(\partial_\tau+\epsilon)c + \bar{c}(\partial_\tau+\epsilon)\delta c + g\delta\bar{c}c(a+\bar{a}) + g\bar{c}\delta c(a+\bar{a})\Big) \\ &=: S[\bar{c},c;\bar{a},a] + \delta S \end{aligned} \tag{A.25}$$

Thus, we have (we have taken advantage of the fact that $\mathcal{D}[\bar{c},c]=\mathcal{D}[\bar{c}',c']$)

$$\begin{aligned}\int \mathcal{D}[\bar{c},c]\mathcal{D}[\bar{a},a]\bar{c}(\tau)e^{-S[\bar{c},c;\bar{a},a]} &= \int \mathcal{D}[\bar{c},c]\mathcal{D}[\bar{a},a](\bar{c}(\tau)+\delta\bar{c}(\tau))e^{-S[\bar{c},c;\bar{a},a]-\delta S} \\ &= \int \mathcal{D}[\bar{c},c]\mathcal{D}[\bar{a},a](\bar{c}(\tau)+\delta\bar{c}(\tau))e^{-S}(1-\delta S) \\ &= \int \mathcal{D}[\bar{c},c]\mathcal{D}[\bar{a},a]\bar{c}(\tau)e^{-S[\bar{c},c;\bar{a},a]}+\int \mathcal{D}[\bar{c},c]\mathcal{D}[\bar{a},a]e^{-S}(\delta\bar{c}(\tau)-\bar{c}(\tau)\delta S)\end{aligned} \tag{A.26}$$

So we have the Schwinger-Dyson equation

$$0=\int \mathcal{D}[\bar{c},c]\mathcal{D}[\bar{a},a]e^{-S}(\delta\bar{c}(\tau)-\bar{c}(\tau)\delta S) \tag{A.27}$$

In order to get the equation of motion for Green function, we set $\delta c=0$, and thus

$$\begin{aligned}&\delta\bar{c}(\tau)-\bar{c}(\tau)\delta S \\ =\;& \delta\bar{c}(\tau)-\bar{c}(\tau)\int_0^\beta d\tau'(\delta\bar{c}(\partial_{\tau'}+\epsilon)c+g\delta\bar{c}c(a+\bar{a})) \\ =\;& \int_0^\beta d\tau'\Big(\delta(\tau'-\tau)\delta\bar{c}(\tau')-\delta\bar{c}(\tau')(\partial_{\tau'}+\epsilon)c(\tau')\bar{c}(\tau)-g\delta\bar{c}(\tau')c(\tau')(a+\bar{a})\bar{c}(\tau)\Big)\end{aligned} \tag{A.28}$$

Plug this back into the Schwinger-Dyson equation, we have

$$\begin{aligned}&\int_0^\beta d\tau'\Bigg[\delta(\tau-\tau')-(\partial_{\tau'}+\epsilon)\frac{1}{Z}\int \mathcal{D}[\bar{c},c]\mathcal{D}[\bar{a},a]e^{-S}c(\tau')\bar{c}(\tau) \\ -\;& g\frac{1}{Z}\int \mathcal{D}[\bar{c},c]\mathcal{D}[\bar{a},a]e^{-S}c(\tau')\phi(\tau')\bar{c}(\tau)\Bigg]\delta\bar{c}(\tau')=0\end{aligned} \tag{A.29}$$

Since this equation holds for any $\delta\bar{c}$, we thus, from the definition of Green function in path integral formulation, have

$$(\partial_{\tau'}+\epsilon)G(\tau',\tau)-g\langle T\hat{c}(\tau')\hat{\phi}(\tau')\hat{c}^\dagger(\tau)\rangle=-\delta(\tau-\tau') \tag{A.30}$$

This is identically the same with the equation of motion that was derived using operator notation.

A.4 Schwinger-Dyson equation for simplified Holstein model: with phonons integrated out

The advantage of Schwinger-Dyson equation method for derivation of equation of motion for Green function is that all we need is the action, rather than the Hamiltonian. Sometimes, the system can be only represented using path integral formulation, but not Hamiltonian. In this case, the Schwinger-Dyson equation is the only method available for the derivation of equation of motion. One such case when the system can be only represented in path integrals is the Holstein model with phonons integrated out, resulting in a time-retarded electronic density interactions. As already stated, the simplified Holstein model is represented by the action

$$S = \int_0^\beta d\tau \bar{c}(\tau)(\partial_\tau + \epsilon)c(\tau) + S_\phi, \tag{A.31}$$

where S_ϕ is the part of the action for phonons, that is,

$$S_\phi = \int_0^\beta d\tau \Big(\bar{a}(\partial_\tau + \omega)a + g\bar{c}c(a + \bar{a}) \Big) \tag{A.32}$$

The partition function for this model is

$$\begin{aligned} Z &= \int \mathcal{D}[\bar{c}, c]\mathcal{D}[\bar{a}, a]e^{-S} \\ &= Z_\phi \int \mathcal{D}[\bar{c}, c]e^{-S_{eff}} \end{aligned} \tag{A.33}$$

Here, Z_ϕ is the partition function for bare phonons, that is, $Z_\phi = \left(1 - e^{-\beta\omega}\right)^{-1}$, and S_{eff} is the effective action obtained after integrating out the phonons. The full expression for the effective action is

$$S_{eff} = \int_0^\beta d\tau \bar{c}(\partial_\tau + \epsilon)c + \frac{1}{2}g^2 \int_0^\beta d\tau_1 \int_0^\beta d\tau_2 \bar{c}(\tau_1)c(\tau_1)D^0(\tau_1 - \tau_2)\bar{c}(\tau_2)c(\tau_2) \tag{A.34}$$

Define a quantity that is invariant under the transformation $c \to c' = c + \delta c, \bar{c} \to \bar{c}' + \delta\bar{c}'$, that is,

$$\int \mathcal{D}[\bar{c}, c]e^{-S_{eff}[\bar{c},c]}\bar{c}(\tau) = \int \mathcal{D}[\bar{c}', c']e^{-S_{eff}[\bar{c}',c']}\bar{c}'(\tau) \tag{A.35}$$

From this equation, after expanding to first order, we have

$$0 = \int \mathcal{D}[\bar{c}, c] e^{-S_{eff}[\bar{c},c]} (-\delta S_{eff} \bar{c}(\tau) + \delta\bar{c}(\tau)) \tag{A.36}$$

If we set $\delta c = 0$ and notice that $D^0(\tau_1 - \tau_2) = D^0(\tau_2 - \tau_1)$, then the variation for the action is

$$\delta S_{eff} = \int_0^\beta d\tau \delta\bar{c}(\partial_\tau + \epsilon)c + g^2 \int_0^\beta d\tau_1 \int_0^\beta d\tau_2 \delta\bar{c}(\tau_1)c(\tau_1)D^0(\tau_1 - \tau_2)\bar{c}(\tau_2)c(\tau_2) \tag{A.37}$$

Thus we have

$$\begin{aligned} & \delta\bar{c}(\tau) - \delta S_{eff}\bar{c}(\tau) \qquad (A.38) \\ = & \int_0^\beta d\tau' \delta\bar{c}(\tau') \left[\delta(\tau - \tau') - (\partial_{\tau'} + \epsilon)c(\tau')\bar{c}(\tau) - g^2 c(\tau')\bar{c}(\tau) \int_0^\beta d\tau_2 D^0(\tau' - \tau_2)\bar{c}(\tau_2)c(\tau_2) \right] \end{aligned}$$

It is required that Equation [A.36] should hold for any variation $\delta\bar{c}$, thus we have the equation of motion for Green function as

$$\begin{aligned} & (\partial_{\tau'} + \epsilon)G(\tau', \tau) \qquad (A.39) \\ - & g^2 \frac{1}{Z} \int \mathcal{D}[\bar{c}, c] e^{-S_{eff}} \left[c(\tau')\bar{c}(\tau) \int_0^\beta d\tau_2 D^0(\tau' - \tau_2)\bar{c}(\tau_2)c(\tau_2) \right] = -\delta(\tau' - \tau) \end{aligned}$$

For the above equation of motion, if we set $\tau = 0, \tau' = 0^-$, then we have the expectation value of the interaction energy as

$$\begin{aligned} & g^2 \frac{1}{Z} \int \mathcal{D}[\bar{c}, c] e^{-S_{eff}} \left[\bar{c}(0)c(0) \int_0^\beta d\tau_2 D^0(\tau_2)\bar{c}(\tau_2)c(\tau_2) \right] \qquad (A.40) \\ = & -(\partial_{\tau'} + \epsilon)G(\tau') \Big|_{\tau'=0^-} - \delta(0^-) \\ = & \frac{1}{\beta} \sum_{i\omega_n} \Sigma(i\omega_n)G(i\omega_n)e^{i\omega_n 0^+} \end{aligned}$$

A.5 Schwinger-Dyson method for derivation of equation of motion for periodic Anderson model with electron-phonon interactions

The model that we are studying, the periodic Anderson model with electron-phonon interactions, with the phonons being integrated out, is represented by this effective action

$$\begin{aligned} S &= \int_0^\beta d\tau \sum_{\boldsymbol{k},\sigma} \begin{pmatrix} \bar{c}_{\boldsymbol{k}\sigma} & \bar{f}_{\boldsymbol{k}\sigma} \end{pmatrix} \cdot \begin{pmatrix} \partial_\tau + \epsilon_{\boldsymbol{k}} & V \\ V & \partial_\tau + \epsilon_f \end{pmatrix} \cdot \begin{pmatrix} c_{\boldsymbol{k}\sigma} \\ f_{\boldsymbol{k}\sigma} \end{pmatrix} \\ &+ \frac{1}{2} g^2 \sum_{\boldsymbol{q}} \sum_{\boldsymbol{k},\sigma} \sum_{\boldsymbol{p},s} \int_0^\beta d\tau_1 \int_0^\beta d\tau_2 \bar{c}_{\boldsymbol{k},\sigma}(\tau_1) c_{\boldsymbol{k}-\boldsymbol{q},\sigma}(\tau_1) D^0(\tau_1 - \tau_2) \bar{c}_{\boldsymbol{p}-\boldsymbol{q},s}(\tau_2) c_{\boldsymbol{p},s}(\tau_2) \\ &- U \int_0^\beta d\tau \sum_{\boldsymbol{kpq}} \bar{f}_{\boldsymbol{p}\uparrow} \bar{f}_{\boldsymbol{q}\downarrow} f_{\boldsymbol{k}\uparrow} f_{\boldsymbol{p}+\boldsymbol{q}-\boldsymbol{k},\downarrow} \end{aligned} \tag{A.41}$$

Consider the transformation of the variables,

$$\begin{aligned} c_{k,\sigma}(\tau) &\to c'_{k,\sigma}(\tau) = c_{k,\sigma}(\tau) + \delta c_{k,\sigma}(\tau) \\ \bar{c}_{k,\sigma}(\tau) &\to \bar{c}'_{k,\sigma}(\tau) = \bar{c}_{k,\sigma}(\tau) + \delta \bar{c}_{k,\sigma}(\tau) \\ f_{k,\sigma}(\tau) &\to f'_{k,\sigma}(\tau) = f_{k,\sigma}(\tau) + \delta f_{k,\sigma}(\tau) \\ \bar{f}_{k,\sigma}(\tau) &\to \bar{f}'_{k,\sigma}(\tau) = \bar{f}_{k,\sigma}(\tau) + \delta \bar{f}_{k,\sigma}(\tau) \end{aligned} \tag{A.42}$$

With this transformation, the action becomes $S[\bar{c}, c; \bar{f}, f] \to S[\bar{c}', c'; \bar{f}', f'] = S[\bar{c}, c; \bar{f}, f] + \delta S$. Define a quantity that is invariant under this transformation,

$$\begin{aligned} & \int \mathcal{D}[\bar{c}, c] \mathcal{D}[\bar{f}, f] e^{-S[\bar{c}, c; \bar{f}, f]} \Big(\bar{c}_{k,\sigma}(\tau), \bar{f}_{k,\sigma}(\tau) \Big) \\ = & \int \mathcal{D}[\bar{c}', c'] \mathcal{D}[\bar{f}', f'] e^{-S[\bar{c}', c'; \bar{f}', f']} \Big(\bar{c}'_{k,\sigma}(\tau), \bar{f}'_{k,\sigma}(\tau) \Big) \\ = & \int \mathcal{D}[\bar{c}, c] \mathcal{D}[\bar{f}, f] e^{-S[\bar{c}, c; \bar{f}, f] - \delta S} \Big(\bar{c}_{k,\sigma}(\tau) + \delta \bar{c}_{k,\sigma}(\tau), \bar{f}_{k,\sigma}(\tau) + \delta \bar{f}_{k,\sigma}(\tau) \Big) \end{aligned} \tag{A.43}$$

After expanding to first order, we have

$$0 = \int \mathcal{D}[\bar{c}, c] \mathcal{D}[\bar{f}, f] e^{-S} \Big(\delta \bar{c}_{k,\sigma}(\tau) - \delta S \bar{c}_{k,\sigma}(\tau), \delta \bar{f}_{k,\sigma}(\tau) - \delta S \bar{f}_{k,\sigma}(\tau) \Big) \tag{A.44}$$

Here, the variation of action is

$$
\begin{aligned}
\delta S &= \int_0^\beta d\tau \sum_{\boldsymbol{k},\sigma} \begin{pmatrix} \delta\bar{c}_{\boldsymbol{k}\sigma} & \delta\bar{f}_{\boldsymbol{k}\sigma} \end{pmatrix} \cdot \begin{pmatrix} \partial_\tau + \epsilon_{\boldsymbol{k}} & V \\ V & \partial_\tau + \epsilon_f \end{pmatrix} \cdot \begin{pmatrix} c_{\boldsymbol{k}\sigma} \\ f_{\boldsymbol{k}\sigma} \end{pmatrix} \\
&+ \int_0^\beta d\tau \sum_{\boldsymbol{k},\sigma} \begin{pmatrix} \bar{c}_{\boldsymbol{k}\sigma} & \bar{f}_{\boldsymbol{k}\sigma} \end{pmatrix} \cdot \begin{pmatrix} \partial_\tau + \epsilon_{\boldsymbol{k}} & V \\ V & \partial_\tau + \epsilon_f \end{pmatrix} \cdot \begin{pmatrix} \delta c_{\boldsymbol{k}\sigma} \\ \delta f_{\boldsymbol{k}\sigma} \end{pmatrix} \\
&+ \frac{g^2}{2} \sum_q \sum_{k,\sigma} \sum_{p,s} \int_0^\beta d\tau_1 \int_0^\beta d\tau_2 \Big[\bar{c}_{k,\sigma}(\tau_1) \delta c_{k-q,\sigma}(\tau_1) D^0(\tau_1 - \tau_2) \bar{c}_{p-q,s}(\tau_2) c_{p,s}(\tau_2) \\
&+ \delta\bar{c}_{k,\sigma}(\tau_1) c_{k-q,\sigma}(\tau_1) D^0(\tau_1 - \tau_2) \bar{c}_{p-q,s}(\tau_2) c_{p,s}(\tau_2) \\
&+ \bar{c}_{k,\sigma}(\tau_1) c_{k-q,\sigma}(\tau_1) D^0(\tau_1 - \tau_2) \bar{c}_{p-q,s}(\tau_2) \delta c_{p,s}(\tau_2) \\
&+ \bar{c}_{k,\sigma}(\tau_1) c_{k-q,\sigma}(\tau_1) D^0(\tau_1 - \tau_2) \delta\bar{c}_{p-q,s}(\tau_2) c_{p,s}(\tau_2) \Big] \\
&- U \sum_{pqk} \int_0^\beta d\tau \Big[\delta\bar{f}_{p,\uparrow} \bar{f}_{q,\downarrow} f_{k,\uparrow} f_{p+q-k,\downarrow} + \bar{f}_{p,\uparrow} \delta\bar{f}_{q,\downarrow} f_{k,\uparrow} f_{p+q-k,\downarrow} \\
&+ \bar{f}_{p,\uparrow} \bar{f}_{q,\downarrow} f_{k,\uparrow} \delta f_{p+q-k,\downarrow} + \bar{f}_{p,\uparrow} \bar{f}_{q,\downarrow} \delta f_{k,\uparrow} f_{p+q-k,\downarrow} \Big]
\end{aligned}
\tag{A.45}
$$

We have two independent equations, which are

$$
\begin{aligned}
\int \mathcal{D}[\bar{c},c]\mathcal{D}[\bar{f},f] e^{-S} \Big[\delta\bar{c}_{k,\sigma}(\tau) - \delta S \bar{c}_{k,\sigma}(\tau) \Big] = 0 \\
\int \mathcal{D}[\bar{c},c]\mathcal{D}[\bar{f},f] e^{-S} \Big[\delta\bar{f}_{k,\sigma}(\tau) - \delta S \bar{f}_{k,\sigma}(\tau) \Big] = 0
\end{aligned}
\tag{A.46}
$$

For the first equation, we can set $\delta c = 0, \delta f = 0, \delta \bar{f} = 0$, and then we have

$$
\begin{aligned}
& \delta \bar{c}_{k,\sigma}(\tau) - \delta S \bar{c}_{k,\sigma}(\tau) \qquad (A.47)\\
= \;& \delta \bar{c}_{k,\sigma}(\tau) - \int_0^\beta d\tau' \sum_{k',\sigma'} \begin{pmatrix} \delta \bar{c}_{k',\sigma'}(\tau') & 0 \end{pmatrix} \begin{pmatrix} \partial_{\tau'} + \epsilon_{k'} & V \\ V & \partial_{\tau'} + \epsilon_f \end{pmatrix} \begin{pmatrix} c_{k',\sigma'}(\tau') \bar{c}_{k,\sigma}(\tau) \\ f_{k',\sigma'}(\tau') \bar{c}_{k,\sigma}(\tau) \end{pmatrix} \\
- \;& \frac{g^2}{2} \sum_q \sum_{k',\sigma'} \sum_{p,s} \int_0^\beta d\tau_1 \int_0^\beta d\tau_2 \Big[\delta \bar{c}_{k',\sigma'}(\tau_1) c_{k'-q,\sigma'}(\tau_1) D^0(\tau_1 - \tau_2) \bar{c}_{p-q,s}(\tau_2) c_{p,s}(\tau_2) \bar{c}_{k,\sigma}(\tau) \\
+ \;& \bar{c}_{k',\sigma'}(\tau_1) c_{k'-q,\sigma'}(\tau_1) D^0(\tau_1 - \tau_2) \delta \bar{c}_{p-q,s}(\tau_2) c_{p,s}(\tau_2) \bar{c}_{k,\sigma}(\tau) \Big] \\
= \;& \delta \bar{c}_{k,\sigma}(\tau) - \int_0^\beta d\tau' \sum_{k',\sigma'} \Big[\delta \bar{c}_{k',\sigma'}(\tau') \Big((\partial_{\tau'} + \epsilon_{k'}) c_{k',\sigma'}(\tau') \bar{c}_{k,\sigma}(\tau) + V f_{k',\sigma'}(\tau') \bar{c}_{k,\sigma}(\tau) \Big) \Big] \\
- \;& \frac{g^2}{2} \sum_q \sum_{k',\sigma'} \sum_{p,s} \int_0^\beta d\tau_1 \int_0^\beta d\tau_2 \Big[\delta \bar{c}_{k',\sigma'}(\tau_1) c_{k'-q,\sigma'}(\tau_1) D^0(\tau_1 - \tau_2) \bar{c}_{p-q,s}(\tau_2) c_{p,s}(\tau_2) \bar{c}_{k,\sigma}(\tau) \\
+ \;& \delta \bar{c}_{k',\sigma'}(\tau_1) c_{k'+q,\sigma'}(\tau_1) D^0(\tau_1 - \tau_2) \bar{c}_{p,s}(\tau_2) c_{p-q,s}(\tau_2) \bar{c}_{k,\sigma}(\tau) \Big] \\
= \;& \int_0^\beta d\tau' \sum_{k',\sigma'} \delta \bar{c}_{k',\sigma'}(\tau') \Big[\delta_{k,k'} \delta_{\sigma,\sigma'} \delta(\tau - \tau') - \Big((\partial_{\tau'} + \epsilon_{k'}) c_{k',\sigma'}(\tau') \bar{c}_{k,\sigma}(\tau) + V f_{k',\sigma'}(\tau') \bar{c}_{k,\sigma}(\tau) \Big) \\
+ \;& \frac{g^2}{2} \sum_q \sum_{p,s} \int_0^\beta d\tau_2 \Big[\bar{c}_{k,\sigma}(\tau) c_{k'-q,\sigma'}(\tau') D^0(\tau' - \tau_2) \bar{c}_{p,s}(\tau_2) c_{p+q,s}(\tau_2) \\
+ \;& \bar{c}_{k,\sigma}(\tau) c_{k'+q,\sigma'}(\tau') D^0(\tau' - \tau_2) \bar{c}_{p,s}(\tau_2) c_{p-q,s}(\tau_2) \Big] \Big] \\
= \;& \int_0^\beta d\tau' \sum_{k',\sigma'} \delta \bar{c}_{k',\sigma'}(\tau') \Big[\delta_{k,k'} \delta_{\sigma,\sigma'} \delta(\tau - \tau') - \Big((\partial_{\tau'} + \epsilon_{k'}) c_{k',\sigma'}(\tau') \bar{c}_{k,\sigma}(\tau) + V f_{k',\sigma'}(\tau') \bar{c}_{k,\sigma}(\tau) \Big) \\
- \;& g^2 \sum_q \sum_{p,s} \int_0^\beta d\tau_2 \Big[c_{k'-q,\sigma'}(\tau') \bar{c}_{k,\sigma}(\tau) D^0(\tau' - \tau_2) \bar{c}_{p,s}(\tau_2) c_{p+q,s}(\tau_2) \Big] \Big]
\end{aligned}
$$

Plug this into the path integral, we have the equation

$$
\begin{aligned}
& -\Big\langle g^2 \sum_q \sum_{p,s} \int_0^\beta d\tau_2 \Big[c_{k'-q,\sigma'}(\tau') \bar{c}_{k,\sigma}(\tau) D^0(\tau' - \tau_2) \bar{c}_{p,s}(\tau_2) c_{p+q,s}(\tau_2) \Big] \Big\rangle \qquad (A.48)\\
= \;& -\delta_{k,k'} \delta_{\sigma,\sigma'} \delta(\tau' - \tau) - \Big[(\partial_{\tau'} + \epsilon_{k'}) G^{cc}_{k,\sigma;k',\sigma'}(\tau' - \tau) + V G^{fc}_{k,\sigma;k',\sigma'}(\tau' - \tau) \Big]
\end{aligned}
$$

For the second equation, we can set $\delta f = 0, \delta c = 0, \delta \bar{c} = 0$, and then we have

$$
\begin{aligned}
& \delta \bar{f}_{k,\sigma}(\tau) - \delta S \bar{f}_{k,\sigma}(\tau) \qquad (A.49)\\
= \; & \delta \bar{f}_{k,\sigma}(\tau) - \int_0^\beta d\tau' \sum_{k',\sigma'} \begin{pmatrix} 0 & \delta \bar{f}_{k',\sigma'}(\tau') \end{pmatrix} \begin{pmatrix} \partial_{\tau'} + \epsilon_{k'} & V \\ V & \partial_{\tau'} + \epsilon_f \end{pmatrix} \begin{pmatrix} c_{k',\sigma'}(\tau') \bar{f}_{k,\sigma}(\tau) \\ f_{k',\sigma'}(\tau') \bar{f}_{k,\sigma}(\tau) \end{pmatrix} \\
- \; & U \sum_{pqk'} \int_0^\beta d\tau' \Big[\delta \bar{f}_{p,\uparrow} \bar{f}_{q,\downarrow} f_{k',\uparrow} f_{p+q-k',\downarrow} \bar{f}_{k,\sigma}(\tau) + \bar{f}_{p,\uparrow} \delta \bar{f}_{q,\downarrow} f_{k',\uparrow} f_{p+q-k',\downarrow} \bar{f}_{k,\sigma}(\tau) \Big] \\
= \; & \delta \bar{f}_{k,\sigma}(\tau) - \sum_{k',\sigma'} \int_0^\beta d\tau' \delta \bar{f}_{k',\sigma'}(\tau') \Big[V c_{k',\sigma'}(\tau') \bar{f}_{k,\sigma}(\tau) + (\partial_{\tau'} + \epsilon_f) f_{k',\sigma'}(\tau') \bar{f}_{k,\sigma}(\tau) \Big] \\
- \; & U \sum_{k'qp} \int_0^\beta d\tau' \Big[\delta \bar{f}_{k',\uparrow} \bar{f}_{q,\downarrow} f_{p,\uparrow} f_{k'+q-p,\downarrow} \bar{f}_{k,\sigma}(\tau) - \delta \bar{f}_{k',\downarrow} \bar{f}_{p,\uparrow} f_{q,\uparrow} f_{p+k'-q,\downarrow} \bar{f}_{k,\sigma}(\tau) \Big] \\
= \; & \sum_{k',\sigma'} \int_0^\beta d\tau' \delta \bar{f}_{k',\sigma'}(\tau') \Bigg[\delta_{k,k'} \delta_{\sigma,\sigma'} \delta(\tau - \tau') - \Big(V c_{k',\sigma'}(\tau') \bar{f}_{k,\sigma}(\tau) + (\partial_{\tau'} + \epsilon_f) f_{k',\sigma'}(\tau') \bar{f}_{k,\sigma}(\tau) \Big) \\
+ \; & U \sum_{pq} \Big(\delta_{\sigma',\uparrow} \bar{f}_{k,\sigma}(\tau) \bar{f}_{q,\downarrow} f_{p,\uparrow} f_{k'+q-p,\downarrow} + \delta_{\sigma',\downarrow} \bar{f}_{p,\uparrow} \bar{f}_{k,\sigma}(\tau) f_{q,\uparrow} f_{p+k'-q,\downarrow} \Big) \Bigg]
\end{aligned}
$$

Plug this into the path integral, we have

$$
\begin{aligned}
& \Big\langle U \sum_{pq} \Big(\delta_{\sigma',\uparrow} \bar{f}_{k,\sigma}(\tau) \bar{f}_{q,\downarrow} f_{p,\uparrow} f_{k'+q-p,\downarrow} + \delta_{\sigma',\downarrow} \bar{f}_{p,\uparrow} \bar{f}_{k,\sigma}(\tau) f_{q,\uparrow} f_{p+k'-q,\downarrow} \Big) \Big\rangle \qquad (A.50)\\
= \; & -\delta_{k,k'} \delta_{\sigma,\sigma'} \delta(\tau' - \tau) - \Big[V G^{cf}_{k,\sigma;k',\sigma'}(\tau' - \tau) + (\partial_{\tau'} + \epsilon_f) G^{ff}_{k,\sigma;k',\sigma'}(\tau' - \tau) \Big]
\end{aligned}
$$

Combining the above two equations together, we have the matrix equation

$$
\begin{aligned}
& \begin{pmatrix} E^g_{k,\sigma;k',\sigma'}(\tau',\tau) & \phi \\ \tilde{\phi} & E^U_{k,\sigma;k',\sigma'}(\tau',\tau) \end{pmatrix} \qquad (A.51)\\
= \; & \begin{pmatrix} -\delta_{k,k'} \delta_{\sigma,\sigma'} \delta(\tau' - \tau) & 0 \\ 0 & -\delta_{k,k'} \delta_{\sigma,\sigma'} \delta(\tau' - \tau) \end{pmatrix} \\
- \; & \begin{pmatrix} \partial_{\tau'} + \epsilon_{k'} & V \\ V & \partial_{\tau'} + \epsilon_f \end{pmatrix} \begin{pmatrix} G^{cc}_{k,\sigma;k',\sigma'}(\tau' - \tau) & G^{cf}_{k,\sigma;k',\sigma'}(\tau' - \tau) \\ G^{fc}_{k,\sigma;k',\sigma'}(\tau' - \tau) & G^{ff}_{k,\sigma;k',\sigma'}(\tau' - \tau) \end{pmatrix}
\end{aligned}
$$

Here, in the above equation, we have defined two quantities

$$E^g_{k,\sigma;k',\sigma'}(\tau',\tau) = -\Big\langle g^2 \sum_q \sum_{p,s} \int_0^\beta d\tau_2 \Big[c_{k'-q,\sigma'}(\tau')\bar{c}_{k,\sigma}(\tau) D^0(\tau'-\tau_2)\bar{c}_{p,s}(\tau_2)c_{p+q,s}(\tau_2)\Big]\Big\rangle$$

$$E^U_{k,\sigma;k',\sigma'}(\tau',\tau) = \Big\langle U \sum_{pq} \Big(\delta_{\sigma',\uparrow}\bar{f}_{k,\sigma}(\tau)\bar{f}_{q,\downarrow}f_{p,\uparrow}f_{k'+q-p,\downarrow} + \delta_{\sigma',\downarrow}\bar{f}_{p,\uparrow}\bar{f}_{k,\sigma}(\tau)f_{q,\uparrow}f_{p+k'-q,\downarrow}\Big)\Big\rangle$$

If we set $k = k', \sigma = \sigma', \tau = 0, \tau' = 0^-$ in Equation [A.51], then we have

$$\begin{aligned}
& \begin{pmatrix} E^g_{k,\sigma} & \phi \\ \tilde{\phi} & E^U_{k,\sigma} \end{pmatrix} \qquad (A.52)\\
= & \begin{pmatrix} -\delta(0^-) & 0 \\ 0 & -\delta(0^-) \end{pmatrix} \\
- & \begin{pmatrix} \partial_{\tau'}+\epsilon_k & V \\ V & \partial_{\tau'}+\epsilon_f \end{pmatrix} \begin{pmatrix} G^{cc}_{k,\sigma}(0^-) & G^{cf}_{k,\sigma}(0^-) \\ G^{fc}_{k,\sigma}(0^-) & G^{ff}_{k,\sigma}(0^-) \end{pmatrix} \\
= & \begin{pmatrix} -\delta(0^-) & 0 \\ 0 & -\delta(0^-) \end{pmatrix} \\
- & \frac{1}{\beta}\sum_{i\omega_n} \begin{pmatrix} \partial_{\tau'}+\epsilon_k & V \\ V & \partial_{\tau'}+\epsilon_f \end{pmatrix} \begin{pmatrix} G^{cc}_{k,\sigma}(i\omega_n) & G^{cf}_{k,\sigma}(i\omega_n) \\ G^{fc}_{k,\sigma}(i\omega_n) & G^{ff}_{k,\sigma}(i\omega_n) \end{pmatrix} e^{-i\omega_n\tau'}\Big|_{\tau'=0^-} \\
= & \begin{pmatrix} -\delta(0^-) & 0 \\ 0 & -\delta(0^-) \end{pmatrix} \\
- & \frac{1}{\beta}\sum_{i\omega_n} \begin{pmatrix} -i\omega_n+\epsilon_k & V \\ V & -i\omega_n+\epsilon_f \end{pmatrix} \begin{pmatrix} G^{cc}_{k,\sigma}(i\omega_n) & G^{cf}_{k,\sigma}(i\omega_n) \\ G^{fc}_{k,\sigma}(i\omega_n) & G^{ff}_{k,\sigma}(i\omega_n) \end{pmatrix} e^{i\omega_n 0^+} \\
= & \begin{pmatrix} -\delta(0^-) & 0 \\ 0 & -\delta(0^-) \end{pmatrix} + \frac{1}{\beta}\sum_{i\omega_n} \Big(G^0_k(i\omega_n)\Big)^{-1} G_{k,\sigma}(i\omega_n)e^{i\omega_n 0^+} \\
= & \begin{pmatrix} -\delta(0^-) & 0 \\ 0 & -\delta(0^-) \end{pmatrix} + \frac{1}{\beta}\sum_{i\omega_n} \Big(G^{-1}_{k,\sigma}(i\omega_n) + \Sigma_{k,\sigma}(i\omega_n)\Big) G_{k,\sigma}(i\omega_n)e^{i\omega_n 0^+} \\
= & -\delta(0^-)\mathbb{I}_{2\times 2} + \frac{1}{\beta}\sum_{i\omega_n}\mathbb{I}_{2\times 2}e^{i\omega_n 0^+} + \frac{1}{\beta}\sum_{i\omega_n}\Sigma_{k,\sigma}(i\omega_n)G_{k,\sigma}(i\omega_n)e^{i\omega_n 0^+} \\
= & \frac{1}{\beta}\sum_{i\omega_n}\Sigma_{k,\sigma}(i\omega_n)G_{k,\sigma}(i\omega_n)e^{i\omega_n 0^+}
\end{aligned}$$

Therefore, the total potential energy is

$$
\begin{aligned}
E_V &= \frac{1}{2}\sum_{k,\sigma}\mathrm{Tr}\begin{pmatrix} E^g_{k,\sigma} & \phi \\ \tilde{\phi} & E^U_{k,\sigma} \end{pmatrix} \\
&= \frac{1}{2}\frac{1}{\beta}\sum_{i\omega_n}\sum_{k,\sigma}\mathrm{Tr}\Big(\Sigma_{k,\sigma}(i\omega_n)G_{k,\sigma}(i\omega_n)\Big)e^{i\omega_n 0^+}
\end{aligned}
\tag{A.53}
$$

A.6 Total energy for periodic Anderson model with electron-phonon interactions

In the previous section, we have shown how to calculate the potential energy in periodic Anderson model (PAM) with electron-phonon interactions. In order to obtain the total energy of the system, it is also necessary to calculate the kinetic energy. The calculation of kinetic energy is pretty straightforward. The only thing that calls for special attention is that high-frequency conditioning is indispensable while summing over all the Matsubara frequencies.

A.6.1 Numerical calculation of kinetic energy

First define some variables that are useful for expressing the Green function.

$$
\begin{aligned}
\alpha_n &= i\omega_n - (\epsilon_f - \mu) - \Sigma^{ff} \\
\beta_n &= i\omega_n + \mu - \Sigma^{cc} \\
\gamma_n &= \beta_n - \frac{(V + \Sigma^{cf})(V + \Sigma^{fc})}{\alpha_n}
\end{aligned}
\tag{A.54}
$$

The kinetic energy is

$$
\begin{aligned}
E_{kinetic} &= \frac{1}{\beta}\mathrm{Tr}\sum_{\boldsymbol{k},\sigma,i\omega_n}\begin{pmatrix}\epsilon_{\boldsymbol{k}} & V\\ V & \epsilon_f\end{pmatrix}\begin{pmatrix}G^{cc}_{\boldsymbol{k},\sigma}(i\omega_n) & G^{cf}_{\boldsymbol{k},\sigma}(i\omega_n)\\ G^{fc}_{\boldsymbol{k},\sigma}(i\omega_n) & G^{ff}_{\boldsymbol{k},\sigma}(i\omega_n)\end{pmatrix} \\
&= \frac{2}{\beta}\mathrm{Tr}\sum_{\boldsymbol{k},i\omega_n}\begin{pmatrix}\epsilon_{\boldsymbol{k}} & V\\ V & \epsilon_f\end{pmatrix}\begin{pmatrix}G^{cc}_{\boldsymbol{k}}(i\omega_n) & G^{cf}_{\boldsymbol{k}}(i\omega_n)\\ G^{fc}_{\boldsymbol{k}}(i\omega_n) & G^{ff}_{\boldsymbol{k}}(i\omega_n)\end{pmatrix} \\
&= \frac{2}{\beta}\mathrm{Tr}\sum_{\boldsymbol{k},i\omega_n}\begin{pmatrix}\epsilon_{\boldsymbol{k}} & V\\ V & \epsilon_f\end{pmatrix}\begin{pmatrix}\frac{1}{\gamma_n-\epsilon_{\boldsymbol{k}}} & \frac{V+\Sigma^{cf}}{\alpha_n}\frac{1}{\gamma_n-\epsilon_{\boldsymbol{k}}}\\ \frac{V+\Sigma^{fc}}{\alpha_n}\frac{1}{\gamma_n-\epsilon_{\boldsymbol{k}}} & \frac{1}{\alpha_n}\frac{\beta_n-\epsilon_{\boldsymbol{k}}}{\gamma_n-\epsilon_{\boldsymbol{k}}}\end{pmatrix} \\
&= \frac{2}{\beta}\sum_{\boldsymbol{k},i\omega_n}\left(\frac{\epsilon_{\boldsymbol{k}}}{\gamma_n-\epsilon_{\boldsymbol{k}}}+\frac{V+\Sigma^{fc}}{\alpha_n}\frac{V}{\gamma_n-\epsilon_{\boldsymbol{k}}}+\frac{V+\Sigma^{cf}}{\alpha_n}\frac{V}{\gamma_n-\epsilon_{\boldsymbol{k}}}+\frac{\epsilon_f}{\alpha_n}\frac{\beta_n-\epsilon_{\boldsymbol{k}}}{\gamma_n-\epsilon_{\boldsymbol{k}}}\right) \\
&= \frac{2}{\beta}\sum_{\boldsymbol{k},i\omega_n}\frac{\epsilon_{\boldsymbol{k}}}{\gamma_n-\epsilon_{\boldsymbol{k}}}+\frac{2}{\beta}\sum_{i\omega_n}\left(V\overline{G}^{fc}(i\omega_n)+V\overline{G}^{cf}(i\omega_n)+\epsilon_f\overline{G}^{ff}(i\omega_n)\right)
\end{aligned}
\tag{A.55}
$$

The first term in the kinetic energy is

$$
\sum_{\boldsymbol{k}}\frac{\epsilon_{\boldsymbol{k}}}{\gamma_n-\epsilon_{\boldsymbol{k}}}=\int_{-\infty}^{\infty}d\epsilon\frac{\epsilon}{\gamma_n-\epsilon}\rho(\epsilon), \tag{A.56}
$$

and $\rho(\epsilon)$ is the one-particle density of states which, for infinite dimensional hyper-cubic lattice, is

$$
\rho(\epsilon)=\frac{1}{\sqrt{2\pi}t}e^{-\frac{\epsilon^2}{2t^2}}. \tag{A.57}
$$

In order to have the best possible result, we need to apply the high-frequency conditioning to the summation in the calculation of kinetic energy. We are to evaluate the summations analytically with the assumptions that the self-energy is zero. Thus, we have a summation like this:

$$
\frac{1}{\beta}\sum_{i\omega_n}\frac{1}{\gamma_n-\epsilon},\gamma_n=i\omega_n+\mu-\frac{V^2}{i\omega_n+\mu-\epsilon_f} \tag{A.58}
$$

In order to get a physically meaningful result, we need to introduce a convergence factor in the summation. That is,

$$
\begin{aligned}
&\frac{1}{\beta}\sum_{i\omega_n}\frac{e^{i\omega_n 0^+}}{\gamma_n-\epsilon} \\
=\ &\frac{1}{\beta}\sum_{i\omega_n}\frac{i\omega_n+\mu-\epsilon_f}{(i\omega_n+\mu-\epsilon)(i\omega_n+\mu-\epsilon_f)-V^2}e^{i\omega_n 0^+}
\end{aligned}
\tag{A.59}
$$

Consider this contour integral.

$$\oint_{z=Re^{i\theta}} \frac{(z+\mu-\epsilon_f)e^{z0^+}}{(z+\mu-\epsilon)(z+\mu-\epsilon_f)-V^2}\frac{1}{e^{\beta z}+1}dz \tag{A.60}$$

It can be shown that the integral on the outer circle $z = Re^{i\theta}$ is zero, as $R \to \infty$. From Cauchy's theorem, we have

$$\begin{aligned}
&\oint_{z=Re^{i\theta}} = 0 = \oint_{z=z_+ +\delta e^{i\theta}} + \oint_{z=z_- +\delta e^{i\theta}} + \sum_{i\omega_n} \oint_{z=i\omega_n+\delta e^{i\theta}}, \\
&z_\pm = -\mu + \frac{1}{2}(\epsilon + \epsilon_f \pm \sqrt{\Delta}), \Delta = (\epsilon-\epsilon_f)^2 + 4V^2
\end{aligned} \tag{A.61}$$

$$\begin{aligned}
\oint_{z=z_+ +\delta e^{i\theta}} &= 2\pi i \frac{\frac{1}{2}(\epsilon-\epsilon_f+\sqrt{\Delta})}{\sqrt{\Delta}}\frac{1}{e^{\beta z_+}+1} \\
\oint_{z=z_- +\delta e^{i\theta}} &= 2\pi i \frac{\frac{1}{2}(\epsilon-\epsilon_f-\sqrt{\Delta})}{-\sqrt{\Delta}}\frac{1}{e^{\beta z_-}+1} \\
\oint_{z=i\omega_n+\delta e^{i\theta}} &= -\frac{2\pi i}{\beta}\frac{1}{\gamma_n-\epsilon}
\end{aligned} \tag{A.62}$$

Therefore, we have

$$\begin{aligned}
&\frac{1}{\beta}\sum_{i\omega_n}\frac{e^{i\omega_n 0^+}}{\gamma_n-\epsilon} = \frac{\frac{1}{2}(\epsilon-\epsilon_f+\sqrt{\Delta})}{\sqrt{\Delta}}\frac{1}{e^{\beta z_+}+1} + \frac{\frac{1}{2}(\epsilon-\epsilon_f-\sqrt{\Delta})}{-\sqrt{\Delta}}\frac{1}{e^{\beta z_-}+1}, \\
&z_\pm = -\mu + \frac{1}{2}(\epsilon+\epsilon_f \pm \sqrt{\Delta}), \Delta = (\epsilon-\epsilon_f)^2 + 4V^2, \\
&\gamma_n = i\omega_n + \mu - \frac{V^2}{i\omega_n+\mu-\epsilon_f}
\end{aligned} \tag{A.63}$$

Another term that requires high-frequency conditioning is the summation over $G^{ff}(i\omega_n)$. Here, we have

$$\frac{1}{\beta}\sum_{i\omega_n} G_0^{ff}(i\omega_n)e^{i\omega_n 0^+} = \frac{1}{\beta}\sum_{i\omega_n}\frac{i\omega_n+\mu-\epsilon}{(i\omega_n+\mu-\epsilon_f)(i\omega_n+\mu-\epsilon)-V^2}e^{i\omega_n 0^+} \tag{A.64}$$

Consider this contour integral.

$$\oint_{z=Re^{i\theta}} \frac{(z+\mu-\epsilon)e^{z0^+}}{(z+\mu-\epsilon_f)(z+\mu-\epsilon)-V^2}\frac{1}{e^{\beta z}+1}dz \tag{A.65}$$

Similarly, we have

$$\oint_{z=Re^{i\theta}} = 0 = \oint_{z=z_+ +\delta e^{i\theta}} + \oint_{z=z_- +\delta e^{i\theta}} + \sum_{i\omega_n} \oint_{z=i\omega_n+\delta e^{i\theta}}, \tag{A.66}$$
$$z_\pm = -\mu + \frac{1}{2}(\epsilon + \epsilon_f \pm \sqrt{\Delta}), \Delta = (\epsilon - \epsilon_f)^2 + 4V^2$$

$$\begin{aligned}
\oint_{z=z_+ +\delta e^{i\theta}} &= 2\pi i \frac{\frac{1}{2}(-\epsilon + \epsilon_f + \sqrt{\Delta})}{\sqrt{\Delta}} \frac{1}{e^{\beta z_+} + 1} \\
\oint_{z=z_- +\delta e^{i\theta}} &= 2\pi i \frac{\frac{1}{2}(-\epsilon + \epsilon_f - \sqrt{\Delta})}{-\sqrt{\Delta}} \frac{1}{e^{\beta z_-} + 1} \\
\oint_{z=i\omega_n+\delta e^{i\theta}} &= \frac{2\pi i}{-\beta} \frac{i\omega_n + \mu - \epsilon}{(i\omega_n + \mu - \epsilon_f)(i\omega_n + \mu - \epsilon) - V^2}
\end{aligned} \tag{A.67}$$

Therefore, we have the summation formula

$$\begin{aligned}
& \frac{1}{\beta} \sum_{i\omega_n} G_0^{ff} e^{i\omega_n 0^+} \\
= \quad & \frac{1}{\beta} \sum_{i\omega_n} \frac{i\omega_n + \mu - \epsilon}{(i\omega_n + \mu - \epsilon_f)(i\omega_n + \mu - \epsilon) - V^2} e^{i\omega_n 0^+} \\
= \quad & \frac{\frac{1}{2}(-\epsilon + \epsilon_f + \sqrt{\Delta})}{\sqrt{\Delta}} \frac{1}{e^{\beta z_+} + 1} + \frac{\frac{1}{2}(-\epsilon + \epsilon_f - \sqrt{\Delta})}{-\sqrt{\Delta}} \frac{1}{e^{\beta z_-} + 1}
\end{aligned} \tag{A.68}$$

With the introduction of high-frequency conditioning, the formula for the calculation of kinetic energy needs to be modified. We are going to use the fully interacting Green function and here the self energy dependence of the variables $\alpha_n, \beta_n, \gamma_n$ is restored. That is,

$$\begin{aligned}
\alpha_n &= i\omega_n - (\epsilon_f - \mu) - \Sigma^{ff} \\
\beta_n &= i\omega_n + \mu - \Sigma^{cc} \\
\gamma_n &= \beta_n - \frac{(V + \Sigma^{cf})(V + \Sigma^{fc})}{\alpha_n}
\end{aligned} \tag{A.69}$$

With these notations, the kinetic energy is

$$\begin{aligned}
E_{kinetic} &= \frac{2}{\beta} \sum_{\boldsymbol{k}, i\omega_n} \left(\frac{\epsilon_{\boldsymbol{k}}}{\gamma_n - \epsilon_{\boldsymbol{k}}} + \frac{V + \Sigma^{fc}}{\alpha_n} \frac{V}{\gamma_n - \epsilon_{\boldsymbol{k}}} + \frac{V + \Sigma^{cf}}{\alpha_n} \frac{V}{\gamma_n - \epsilon_{\boldsymbol{k}}} + \frac{\epsilon_f}{\alpha_n} \frac{\beta_n - \epsilon_{\boldsymbol{k}}}{\gamma_n - \epsilon_{\boldsymbol{k}}} \right) \\
&= \frac{2}{\beta} \sum_{\boldsymbol{k}, i\omega_n} \frac{\epsilon_{\boldsymbol{k}}}{\gamma_n - \epsilon_{\boldsymbol{k}}} + \frac{2}{\beta} \sum_{\boldsymbol{k}, i\omega_n} \frac{\epsilon_f}{\alpha_n} \frac{\beta_n - \epsilon_{\boldsymbol{k}}}{\gamma_n - \epsilon_{\boldsymbol{k}}} + \frac{2V}{\beta} \sum_{i\omega_n} \left(\overline{G}^{fc}(i\omega_n) + \overline{G}^{cf}(i\omega_n) \right) \\
&= \int_{-\infty}^{\infty} d\epsilon \rho(\epsilon) \frac{2}{\beta} \sum_{i\omega_n} \frac{\epsilon}{\gamma_n - \epsilon} + \int_{-\infty}^{\infty} d\epsilon \rho(\epsilon) \frac{2}{\beta} \sum_{i\omega_n} \frac{\epsilon_f}{\alpha_n} \frac{\beta_n - \epsilon}{\gamma_n - \epsilon} + \frac{2V}{\beta} \sum_{i\omega_n} \left(\overline{G}^{fc}(i\omega_n) + \overline{G}^{cf}(i\omega_n) \right)
\end{aligned} \tag{A.70}$$

To apply high-frequency conditioning, we are to make the following replacements:

$$\begin{aligned}
\frac{1}{\beta}\sum_{i\omega_n}\frac{1}{\gamma_n-\epsilon} &\rightarrow \frac{1}{\beta}\sum_{i\omega_n}\frac{1}{\gamma_n-\epsilon} \\
&+ \left(\frac{\frac{1}{2}(\epsilon-\epsilon_f+\sqrt{\Delta})}{\sqrt{\Delta}}\frac{1}{e^{\beta z_+}+1}+\frac{\frac{1}{2}(\epsilon-\epsilon_f-\sqrt{\Delta})}{-\sqrt{\Delta}}\frac{1}{e^{\beta z_-}+1}-\frac{1}{\beta}\sum_{i\omega_n}G_0^{cc}(i\omega_n)\right) \\
\frac{1}{\beta}\sum_{i\omega_n}\frac{1}{\alpha_n}\frac{\beta_n-\epsilon}{\gamma_n-\epsilon} &\rightarrow \frac{1}{\beta}\sum_{i\omega_n}\frac{1}{\alpha_n}\frac{\beta_n-\epsilon}{\gamma_n-\epsilon} \\
&+ \left(\frac{\frac{1}{2}(-\epsilon+\epsilon_f+\sqrt{\Delta})}{\sqrt{\Delta}}\frac{1}{e^{\beta z_+}+1}+\frac{\frac{1}{2}(-\epsilon+\epsilon_f-\sqrt{\Delta})}{-\sqrt{\Delta}}\frac{1}{e^{\beta z_-}+1}-\frac{1}{\beta}\sum_{i\omega_n}G_0^{ff}(i\omega_n)\right)
\end{aligned} \tag{A.71}$$

Here, we have made the following definitions:

$$\begin{aligned}
z_\pm &= -\mu+\frac{1}{2}(\epsilon+\epsilon_f\pm\sqrt{\Delta}), \\
\Delta &= (\epsilon-\epsilon_f)^2+4V^2.
\end{aligned} \tag{A.72}$$

A.6.2 Numerical calculation of potential energy

Now with both kinetic energy and potential energy, we can calculate the total energy of the system. The total energy of the system can be written compactly as

$$\begin{aligned}
E &= E_{kinetic}+E_V \\
&= \frac{1}{\beta}\sum_{k,\sigma,i\omega_n}\mathrm{Tr}\left[\left(\tilde{\epsilon}_k+\frac{1}{2}\tilde{\Sigma}_{k,\sigma}(i\omega_n)\right)\tilde{G}_{k,\sigma}(i\omega_n)\right]e^{i\omega_n 0^+}
\end{aligned} \tag{A.73}$$

Here, $\tilde{\epsilon}_k, \tilde{\Sigma}_{k,\sigma}(i\omega_n), \tilde{G}_{k,\sigma}(i\omega_n)$ are all 2×2 matrices, which are defined as

$$\begin{aligned}
\tilde{\epsilon}_k &= \begin{pmatrix} \epsilon_{\boldsymbol{k}} & V \\ V & \epsilon_f \end{pmatrix} \\
\tilde{\Sigma}_{k,\sigma}(i\omega_n) &= \begin{pmatrix} \Sigma^{cc}_{k,\sigma}(i\omega_n) & \Sigma^{cf}_{k,\sigma}(i\omega_n) \\ \Sigma^{fc}_{k,\sigma}(i\omega_n) & \Sigma^{ff}_{k,\sigma}(i\omega_n) \end{pmatrix} \\
\tilde{G}_{k,\sigma}(i\omega_n) &= \begin{pmatrix} G^{cc}_{k,\sigma}(i\omega_n) & G^{cf}_{k,\sigma}(i\omega_n) \\ G^{fc}_{k,\sigma}(i\omega_n) & G^{ff}_{k,\sigma}(i\omega_n) \end{pmatrix}
\end{aligned} \tag{A.74}$$

To calculate the numerical value of the potential energy, we also need high frequency conditioning.

The high frequency behavior of self-energy in DMFT is known to be

$$\begin{pmatrix} \Sigma^{cc}_{k,\sigma}(i\omega_n) & \Sigma^{cf}_{k,\sigma}(i\omega_n) \\ \Sigma^{fc}_{k,\sigma}(i\omega_n) & \Sigma^{ff}_{k,\sigma}(i\omega_n) \end{pmatrix} \to \begin{pmatrix} a + \frac{b}{\omega_n^2} + \frac{ic}{\omega_n} & 0 \\ 0 & a' + \frac{b'}{\omega_n} + \frac{ic'}{\omega_n} \end{pmatrix} \tag{A.75}$$

It is already shown that the potential energy is

$$\begin{aligned} E_V &= \frac{1}{2\beta} \sum_{k,\sigma,i\omega_n} \mathrm{Tr}\Big[\tilde{\Sigma}_{k,\sigma}(i\omega_n)\tilde{G}_{k,\sigma}(i\omega_n)\Big] e^{i\omega_n 0^+} \\ &= \frac{1}{\beta} \sum_{k} \sum_{n=-\infty}^{\infty} \mathrm{Tr}\Big[\tilde{\Sigma}_{k}(i\omega_n)\tilde{G}_{k}(i\omega_n)\Big] e^{i\omega_n 0^+} \end{aligned} \tag{A.76}$$

Next we will only focus on the summation over frequencies. The frequency summation is

$$
\begin{aligned}
S_k &= \frac{1}{\beta}\sum_{n=-\infty}^{\infty}\mathrm{Tr}\Big[\tilde{\Sigma}_k(i\omega_n)\tilde{G}_k(i\omega_n)\Big]e^{i\omega_n 0^+} \qquad (A.77)\\
&= \frac{1}{\beta}\sum_{n=-N}^{N}\mathrm{Tr}\Big[\tilde{\Sigma}_k(i\omega_n)\tilde{G}_k(i\omega_n)\Big]e^{i\omega_n 0^+}\\
&+ \frac{1}{\beta}\sum_{n=-\infty}^{-N-1}\mathrm{Tr}\Big[\tilde{\Sigma}_k(i\omega_n)\tilde{G}_k(i\omega_n)\Big]e^{i\omega_n 0^+} + \frac{1}{\beta}\sum_{n=N+1}^{\infty}\mathrm{Tr}\Big[\tilde{\Sigma}_k(i\omega_n)\tilde{G}_k(i\omega_n)\Big]e^{i\omega_n 0^+}\\
&\approx \frac{1}{\beta}\sum_{n=-N}^{N}\mathrm{Tr}\Big[\tilde{\Sigma}_k(i\omega_n)\tilde{G}_k(i\omega_n)\Big]e^{i\omega_n 0^+}\\
&+ \frac{1}{\beta}\sum_{n=-\infty}^{-N-1}\mathrm{Tr}\left[\begin{pmatrix} a & 0\\ 0 & a'\end{pmatrix}\begin{pmatrix} G_k^{cc(0)}(i\omega_n) & G_k^{cf(0)}(i\omega_n)\\ G_k^{fc(0)}(i\omega_n) & G_k^{ff(0)}(i\omega_n)\end{pmatrix}\right]e^{i\omega_n 0^+}\\
&+ \frac{1}{\beta}\sum_{n=N+1}^{\infty}\mathrm{Tr}\left[\begin{pmatrix} a & 0\\ 0 & a'\end{pmatrix}\begin{pmatrix} G_k^{cc(0)}(i\omega_n) & G_k^{cf(0)}(i\omega_n)\\ G_k^{fc(0)}(i\omega_n) & G_k^{ff(0)}(i\omega_n)\end{pmatrix}\right]e^{i\omega_n 0^+}\\
&= \frac{1}{\beta}\sum_{n=-N}^{N}\mathrm{Tr}\Big[\tilde{\Sigma}_k(i\omega_n)\tilde{G}_k(i\omega_n)\Big]e^{i\omega_n 0^+}\\
&+ \frac{1}{\beta}\sum_{n=-\infty}^{\infty}\mathrm{Tr}\left[\begin{pmatrix} a & 0\\ 0 & a'\end{pmatrix}\begin{pmatrix} G_k^{cc(0)}(i\omega_n) & G_k^{cf(0)}(i\omega_n)\\ G_k^{fc(0)}(i\omega_n) & G_k^{ff(0)}(i\omega_n)\end{pmatrix}\right]e^{i\omega_n 0^+}\\
&- \frac{1}{\beta}\sum_{n=-N}^{N}\mathrm{Tr}\left[\begin{pmatrix} a & 0\\ 0 & a'\end{pmatrix}\begin{pmatrix} G_k^{cc(0)}(i\omega_n) & G_k^{cf(0)}(i\omega_n)\\ G_k^{fc(0)}(i\omega_n) & G_k^{ff(0)}(i\omega_n)\end{pmatrix}\right]e^{i\omega_n 0^+}\\
&= \frac{1}{\beta}\sum_{n=-N}^{N}\mathrm{Tr}\Big[\tilde{\Sigma}_k(i\omega_n)\tilde{G}_k(i\omega_n)\Big]e^{i\omega_n 0^+}\\
&+ \frac{1}{\beta}\sum_{n=-\infty}^{\infty}\Big(aG_k^{cc(0)}(i\omega_n) + a'G_k^{ff(0)}(i\omega_n)\Big)e^{i\omega_n 0^+} - \frac{1}{\beta}\sum_{n=-N}^{N}\Big(aG_k^{cc(0)}(i\omega_n) + a'G_k^{ff(0)}(i\omega_n)\Big)e^{i\omega_n 0^+}
\end{aligned}
$$

The potential energy is thus

$$
\begin{aligned}
E_V &= \sum_k S_k \qquad (A.78)\\
&= \frac{1}{\beta}\sum_{n=-N}^{N} \mathrm{Tr}\Big[\tilde{\Sigma}(i\omega_n)\tilde{G}(i\omega_n)\Big]\\
&+ a\int_{-\infty}^{\infty} d\epsilon\rho(\epsilon)\left(\frac{\frac{1}{2}(\epsilon-\epsilon_f+\sqrt{\Delta})}{\sqrt{\Delta}}\frac{1}{e^{\beta z_+}+1}+\frac{\frac{1}{2}(\epsilon-\epsilon_f-\sqrt{\Delta})}{-\sqrt{\Delta}}\frac{1}{e^{\beta z_-}+1}\right)\\
&+ a'\int_{-\infty}^{\infty} d\epsilon\rho(\epsilon)\left(\frac{\frac{1}{2}(-\epsilon+\epsilon_f+\sqrt{\Delta})}{\sqrt{\Delta}}\frac{1}{e^{\beta z_+}+1}+\frac{\frac{1}{2}(-\epsilon+\epsilon_f-\sqrt{\Delta})}{-\sqrt{\Delta}}\frac{1}{e^{\beta z_-}+1}\right)\\
&- \frac{1}{\beta}\sum_{n=-N}^{N}\Big(aG^{cc(0)}(i\omega_n)+a'G^{ff(0)}(i\omega_n)\Big)
\end{aligned}
$$

Here, we have made the following definitions:

$$
\begin{aligned}
z_\pm &= -\mu+\frac{1}{2}(\epsilon+\epsilon_f\pm\sqrt{\Delta}), \qquad (A.79)\\
\Delta &= (\epsilon-\epsilon_f)^2+4V^2.
\end{aligned}
$$

Appendix B

Maximum Entropy Method

Maximum entropy method is widely used to extract the density of states (DOS) from the knowledge of Matsubara Green function, whether be it in imaginary time space or imaginary frequency space. It is a method that is based upon Bayesian analysis, and can give us the best possible inference given incomplete information. A detailed review of this method is already available in [37]. Here, I will give only a brief introduction

B.1 Algorithm description

In this section, I will briefly describe the method of extracting the DOS from the imaginary frequency Matsubara Green function. The spectral function, which is proportional to the DOS, is related with the Green function through

$$\begin{aligned} G(i\omega_n) &= \int_{-\infty}^{\infty} d\omega \frac{A(\omega)}{i\omega_n - \omega} \\ &:= KA(i\omega_n) \end{aligned} \tag{B.1}$$

Here, $\omega_n = \frac{(2n+1)\pi}{\beta}$ is a discrete variable, and ω is a continuous variable, K is the kernel function, and KA is a short-hand notation for the integration over ω. From the above equation, we can easily determine the value of $G(i\omega_n)$ once we know the spectral function $A(\omega)$. However, in reality, what we know is the imaginary frequency Green function, which can be computed from quantum Monte Carlo simulation, and what we want to extract is the spectral function that allows us to compare our numerical results with experiments. Direct inversion of Equation [B.1] is not viable, since the rapid decrease of the spectral function at large frequency region renders the Green function insensitive to the details of the spectral function. Thus, infinitely many spectral functions may correspond to a single Green function. In order to solve this conundrum, maximum entropy (MaxEnt) method is devised. In the framework of MaxEnt, what we get is not the precise density of states corresponding to a Matsubara Green function, rather, it the most probable DOS that can be obtained from the

existing incomplete and noisy information. In order to do this, we will use Bayesian inference, within which framework, our search of the most probable DOS can be formulated as, how to maximize the probability of getting some spectral function given the knowledge of the imaginary frequency Green function? This probability can be denoted as $p(A|\bar{G})$, and according to the Bayesian inference, we have the relation

$$p(A|\bar{G}) = \frac{p(A)p(\bar{G}|A)}{p(\bar{G})} \tag{B.2}$$

According to [37], $p(A) = \exp(\alpha S)$, and $p(\bar{G}|A) = \exp(-\frac{1}{2}\chi^2)$. From these, we define a quantity Q,

$$Q = \alpha S - \frac{1}{2}\chi^2. \tag{B.3}$$

It is clear that maximization of the probability $p(A|\bar{G})$ is equivalent to maximization of Q. Here, α is a real number that is introduced for annealing purpose, S is the entropy, and χ^2 is the difference between the actual value of Green function and the expected value of Green function. This formula can be understood as a generalization of the least square method. When α is zero, maximization of Q is equivalent to minimization of the difference between the real data and the fitted data. When $\alpha \to \infty$, Q is dominated by entropy, and the maximization of Q is precisely the maximization of entropy. We can interpret the α as temperature, and the $\frac{1}{2}\chi^2$ as the energy. With these interpretations, Q can be interpreted as the negative free energy. Thus, maximization of Q is just the minimization of the free energy. The entropy is defined as

$$S = -\int_{-\infty}^{\infty} d\omega A(\omega) \log \frac{A(\omega)}{D(\omega)}, \tag{B.4}$$

where, $D(\omega)$ is the default model, and χ^2 is defined as

$$\chi^2 \quad = \quad (\bar{G} - KA)^\dagger C^{-1} (\bar{G} - KA) \tag{B.5}$$

In order to understand this formula, some explanation of the Monte Carlo process is needed. The Matsubara Green function G is obtained from Monte Carlo measurements. In order to eliminate the correlations between two successive measurements, we have binned the data. Assume that we want to make 1000 measurements. We will not make these measurements all at once. Rather, we will

make, say 20 measurements in bin one, and another 20 measurements in bin two, etc, until finally we have 20 measurements in bin 50. We average the 20 measured Green functions in bin one, and call it $G^{(1)}$, and similarly in bin two, we get $G^{(2)}$, etc, until we get $G^{(50)}$. The $\bar{G}$ that appears in Equation [B.5] is the average of these 50 bin Green functions. That is, $G = \frac{1}{N}\sum_{i=1}^{N} G^i$, here N is the bin number. From the binned Green functions, we can calculate the covariance matrix C. The definition of the covariance matrix is

$$C_{mn} = \frac{1}{N(N-1)} \sum_{i=1}^{N} \Big(G^{(i)}(i\omega_m) - \bar{G}(i\omega_m) \Big)^* \Big(G^{(i)}(i\omega_n) - \bar{G}(i\omega_n) \Big) \tag{B.6}$$

From the definition, we see that the covariance matrix describes the correlations between adjacent Matsubara frequencies. It is easy to show that the matrix C is Hermitian, that is, $C^\dagger = C$. For sake of the simplicity of notations, we will denote $\xi = \bar{G} - KA$. Since ξ is a complex vector, we can rewrite it as $\xi = \xi_R + i\xi_I$. Here, ξ_R and ξ_I are the real and imaginary part of the vector ξ, respectively. In a similar fashion, the inverse of the covariance matrix can also be rewritten as $C^{-1} = C_R^{-1} + iC_I^{-1}$. With these notations, Equation [B.5] can be recast into the form

$$\begin{aligned} \chi^2 &= \xi_R^T C_R^{-1} \xi_R + \xi_I^T C_R^{-1} \xi_I \\ &= \begin{pmatrix} \xi_R^T & \xi_I^T \end{pmatrix} \begin{pmatrix} C_R^{-1} & 0 \\ 0 & C_R^{-1} \end{pmatrix} \begin{pmatrix} \xi_R \\ \xi_I \end{pmatrix} \end{aligned} \tag{B.7}$$

However, before we can do any numerical calculation, some more work still need to be done. Generally, the covariance matrix may possess exceedingly small eigenvalues, and thus, the covariance matrix may not be invertible. In order to avoid this problem, we will rotate the covariance into its diagonal form, and discard these exceedingly small eigenvalues. We know that C_R is the a real symmetric matrix, thus, it is easy to find an orthogonal matrix U that can rotate C_R^{-1} into a diagonal

matrix. That is, we can rewrite Equation [B.7] as

$$\begin{aligned}
\chi^2 &= \begin{pmatrix} \xi_R^T & \xi_I^T \end{pmatrix} \begin{pmatrix} U\Lambda^{-1}U^T & 0 \\ 0 & U\Lambda^{-1}U^T \end{pmatrix} \begin{pmatrix} \xi_R \\ \xi_I \end{pmatrix} \\
&= \begin{pmatrix} \xi_R^T U & \xi_I^T U \end{pmatrix} \begin{pmatrix} \Lambda^{-1} & 0 \\ 0 & \Lambda^{-1} \end{pmatrix} \begin{pmatrix} U^T\xi_R \\ U^T\xi_I \end{pmatrix} \\
&= \begin{pmatrix} \tilde{\xi}_R^T & \tilde{\xi}_I^T \end{pmatrix} \begin{pmatrix} \Lambda^{-1} & 0 \\ 0 & \Lambda^{-1} \end{pmatrix} \begin{pmatrix} \tilde{\xi}_R \\ \tilde{\xi}_I \end{pmatrix} \\
&= \tilde{\xi}^T \begin{pmatrix} \Lambda^{-1} & 0 \\ 0 & \Lambda^{-1} \end{pmatrix} \tilde{\xi}
\end{aligned} \tag{B.8}$$

Here,

$$\begin{aligned}
\tilde{\xi}_R &= U^T\xi_R \\
&= U^T G_R - U^T K_R A \\
&= \tilde{G}_R - \tilde{K}_R A, \\
\tilde{\xi}_I &= U^T\xi_I \\
&= U^T G_I - U^T K_I A \\
&= \tilde{G}_I - \tilde{K}_I A, \\
\tilde{\xi} &= \begin{pmatrix} \tilde{\xi}_R \\ \tilde{\xi}_I \end{pmatrix}
\end{aligned} \tag{B.9}$$

The diagonal matrix Λ may contain exceedingly small eigenvalues, and thus its inverse may diverge. In order to avoid this kind of singularity, we should discard these exceedingly small eigenvalues. To do this, we will cut off the matrix Λ. After the cut off, the dimension of the matrix would become smaller, and we denote this new matrix as Λ_c. Similarly, the matrix U and the vector $\tilde{\xi}$ will also be cut off, and we denote the new matrix and vector as U_c and $\tilde{\xi}_c$.

Now we can write Q as (Here, and from now on, for sake of simplicity, the subscript c has been removed. It should be understood that the matrices and vectors that appear in the formula below

are all truncated matrices and vectors.)

$$\begin{aligned} Q &= \alpha S - \frac{1}{2}\chi^2 \\ &= \alpha S - \frac{1}{2}\tilde{\xi}_R^T \Lambda^{-1} \tilde{\xi}_R - \frac{1}{2}\tilde{\xi}_I^T \Lambda^{-1} \tilde{\xi}_I \end{aligned} \tag{B.10}$$

In the maximum entropy method, we will calculate the extremal values for Q, and the extremum is obtained by setting the gradient of Q to zero, that is, $\nabla_A Q = 0$. The gradient of Q with respect to $A(\omega_i)$ is (Here, the originally continuous variable ω has been discretized, and the index i is used to enumerate the discretized ω.)

$$\begin{aligned} f(A(\omega_i)) &= \frac{\delta Q}{\delta A(\omega_i)} \\ &= -\alpha\Big(1 + \log\frac{A(\omega_i)}{D(\omega_i)}\Big)\Delta\omega \\ &+ \sum_{nm} \tilde{K}_R(\omega_n, \omega_i)\Delta\omega(\Lambda^{-1})_{nm}\Big(\tilde{G}_R - \tilde{K}_R A\Big)_m \\ &+ \sum_{nm} \tilde{K}_I(\omega_n, \omega_i)\Delta\omega(\Lambda^{-1})_{nm}\Big(\tilde{G}_I - \tilde{K}_I A\Big)_m \end{aligned} \tag{B.11}$$

We will use Newton's method to calculate the roots of the equation $f(A(\omega_i)) = 0$. In Newton's method, we are to solve the iteration equation

$$A_{n+1}(\omega_i) = A_n(\omega_i) - \sum_j (J^{-1})_{ij} f(A_n(\omega_j)). \tag{B.12}$$

Here, we have defined the Jacobian matrix as

$$\begin{aligned} J_{ij} &= \frac{\delta f(A(\omega_i))}{\delta A(\omega_j)} \\ &= \frac{\delta^2 Q}{\delta A(\omega_i)\delta A(\omega_j)} \\ &= -\alpha\Delta\omega\frac{\delta_{ij}}{A(\omega_i)} \\ &\quad - \sum_{nm} \tilde{K}_R(\omega_n, \omega_i)\Delta\omega(\Lambda^{-1})_{nm}\tilde{K}_R(\omega_m, \omega_j)\Delta\omega \\ &\quad - \sum_{nm} \tilde{K}_I(\omega_n, \omega_i)\Delta\omega(\Lambda^{-1})_{nm}\tilde{K}_I(\omega_m, \omega_j)\Delta\omega \end{aligned} \tag{B.13}$$

It is easy to see that the Jaocbian matrix is actually the Hessian matrix for the function Q, with $A(\omega_i)$ as the variables. Moreover, the matrix J is negative definite, which guarantees that we can

always find the maximum for the function Q. Thus, we can rewrite the Equation [B.12] as

$$-J\Big(A_{n+1}(\omega) - A_n(\omega)\Big) = f(A_n(\omega)) \tag{B.14}$$

Since $-J$ is positive definite, we can use conjugate gradient method to solve the above equation. The calculate of the inverse of Jaocbian matrix is not recommended for the solution of Equation [B.12] because of the instability of inverting matrices. The rule of thumb for the numerical solution of linear systems is that, you should avoid inverting matrices whenever possible. As a result of this, we adopt the conjugate gradient method for the solution of Equation [B.12]. The conjugate gradient method is fully described in wikipedia and will not be repeated here. The pseudocode for this method is displayed in Fig. [B.1].

The algorithm is detailed below for solving **Ax** = **b** where **A** is a real, symmetric, positive-definite matrix. The input vector $\mathbf{x}_0$ can be an approximate initial solution or **0**. It is a different formulation of the exact procedure described above.

$\mathbf{r}_0 := \mathbf{b} - \mathbf{A}\mathbf{x}_0$
$\mathbf{p}_0 := \mathbf{r}_0$
$k := 0$
repeat
  $\alpha_k := \dfrac{\mathbf{r}_k^\mathsf{T}\mathbf{r}_k}{\mathbf{p}_k^\mathsf{T}\mathbf{A}\mathbf{p}_k}$
  $\mathbf{x}_{k+1} := \mathbf{x}_k + \alpha_k\mathbf{p}_k$
  $\mathbf{r}_{k+1} := \mathbf{r}_k - \alpha_k\mathbf{A}\mathbf{p}_k$
  if r_{k+1} **is sufficiently small then exit loop**
  $\beta_k := \dfrac{\mathbf{r}_{k+1}^\mathsf{T}\mathbf{r}_{k+1}}{\mathbf{r}_k^\mathsf{T}\mathbf{r}_k}$
  $\mathbf{p}_{k+1} := \mathbf{r}_{k+1} + \beta_k\mathbf{p}_k$
  $k := k + 1$
end repeat
The result is $\mathbf{x}_{k+1}$

Figure B.1: The pseudocode for conjugate gradient algorithm. From wikipedia.

When I run the program, I start from a very large α value. As has been noted above, we can interpret the α as temperature. Maximization of Q, which is equivalent to the minimization of "free energy", is easier to do at high temperature. It can be seen from the definition of Q that when $\alpha \to \infty$, the extremal values of Q will coincide with the extremal values of S. Setting the gradient

of entropy to zero, we have

$$\frac{\delta S}{\delta A(\omega)} = -1 - \log \frac{A(\omega)}{D(\omega)} = 0 \tag{B.15}$$

Solving the above equation, we have $A(\omega) = e^{-1}D(\omega)$. Therefore, when α is very large, the spectral function we have should be very similar to the default model. I have used the Gaussian as the default model, and run the program by initializing the initial spectral function at small α from the calculated spectral function at large α. By doing this, we can get relatively smooth spectral functions free from the spurious features, such as the sharp peaks that do not correspond to any energy scales in the original model.

B.2 DOS results

I am going to use the python program that I developed to calculate the DOS from the knowledge of imaginary frequency Green function. In order to test if the program is correct, I assume that we have a spectral function, which is

$$A(\omega) = \frac{1}{2}N(\omega, -2.1, 0.4) + \frac{1}{2}N(\omega, 1.2, 0.5). \tag{B.16}$$

Here, $N(\omega, \mu, \sigma)$ means a normal distribution with mean value μ and standard deviation σ. From this spectral function, I can calculate the imaginary frequency Green function. I further added Gaussian noise to the Green function, and from the Green function, I extract the spectral function, and compare the calculated spectral function with the original spectral function. The comparison is shown in Fig. B.2.

It can be seen that the calculated result is almost the same as the original spectral function. Therefore, the program can generate the correct spectral function from the knowledge of the imaginary frequency Green function. However, it should be noted that the program is not guaranteed to give the correct spectral function. I have also tested the program for the spectral functions that possess rather special features, such as a sharp peak. In that case, the program cannot resolve the sharp peak. Considering that we are using the program to extract spectra from the Green functions that are generated from Monte Carlo simulation, we do not expect to have very sharp features in the spectral function. Actually, when there are too many sharp features in our spectral function result, we almost always suspect these are spurious features that can be removed when we anneal

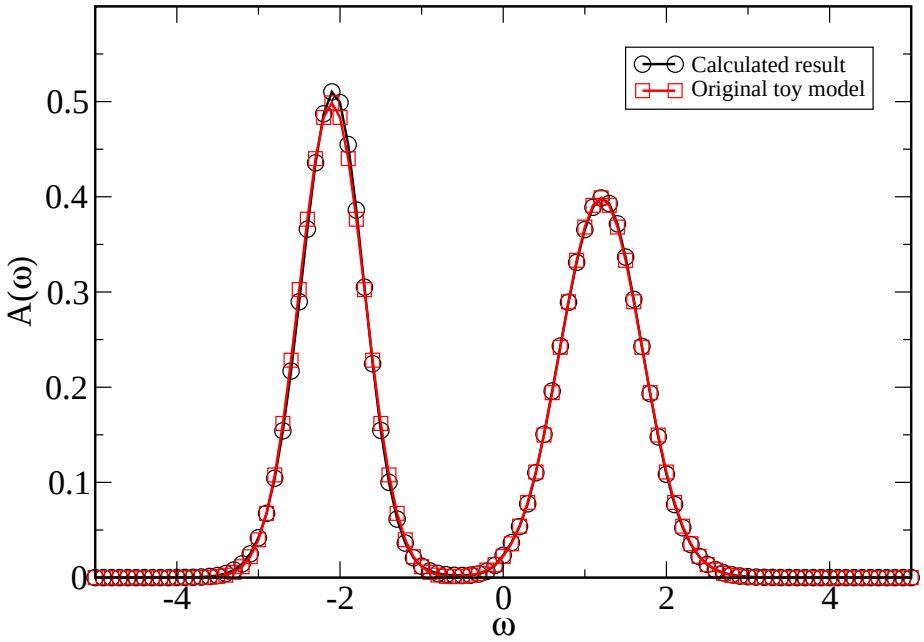

Figure B.2: Comparison of the calculated spectral function with the original known spectral function. The calculated result and the original test model are almost the same, which provides a sound vindication of the program.

the system. Here, by anneal the system, I mean we run program from high temperature to low temperature, and use the output from the high temperature as the input for the low temperature. Our experience is that when we introduce this annealing in temperature, the spurious features disappear, leaving us with a relatively smooth spectral function. Therefore, it is not a serious drawback of the program that it cannot resolve the very sharp features of the spectral function.

B.3 Program implementation of the algrithom

Throughout the thesis, I have been using Mark Jarrell's Fortran code to calculate the DOS. However, I have also written a python code myself. I have tested my program against Mark's program, and they give consistent results. My program for the implementation of the max entropy algorithm can be found through the link: `https://github.com/PrimerLi/maxEntLambda`

Appendix C

Bethe-Salpeter Equation for the Two-band Model

The Bethe-Salpeter equation can be used to calculate the two-particle quantities, such as the charge and magnetic susceptibility. The Bethe-Salpeter equation for one-band has already been well known, and here we will present the derivation of the Bethe-Salpeter equation for the two-band model. Our two band model Hamiltonian is:

$$\hat{H} = \hat{H}_0 + \hat{H}_{\text{int}} + \hat{H}_{\text{ext}} \tag{C.1}$$

Here, the bare Hamiltonian is:

$$\hat{H}_0 = \sum_{\boldsymbol{k},\sigma} \begin{pmatrix} \hat{c}^\dagger_{\boldsymbol{k}\sigma} & \hat{f}^\dagger_{\boldsymbol{k}\sigma} \end{pmatrix} \begin{pmatrix} \epsilon_{\boldsymbol{k}} & V \\ V & \epsilon_f \end{pmatrix} \begin{pmatrix} \hat{c}_{\boldsymbol{k}\sigma} \\ \hat{f}_{\boldsymbol{k}\sigma} \end{pmatrix}, \tag{C.2}$$

and the coupling of particles to external field is described by $\hat{H}_{\text{ext}}$:

$$\hat{H}_{\text{ext}} = \sum_{\boldsymbol{k},\sigma} \begin{pmatrix} \hat{c}^\dagger_{\boldsymbol{k}\sigma} & \hat{f}^\dagger_{\boldsymbol{k}\sigma} \end{pmatrix} \begin{pmatrix} h^{11}_{\boldsymbol{k}\sigma} & h^{12}_{\boldsymbol{k}\sigma} \\ h^{21}_{\boldsymbol{k}\sigma} & h^{22}_{\boldsymbol{k}\sigma} \end{pmatrix} \begin{pmatrix} \hat{c}_{\boldsymbol{k}\sigma} \\ \hat{f}_{\boldsymbol{k}\sigma} \end{pmatrix} \tag{C.3}$$

The interaction of particles is incorporated in $\hat{H}_{\text{int}}$, which may include the retarded density-density interaction mediated by electron-phonon coupling.

To avoid cluttered notation, in this section, we will leave out the momentum dependence, and only focus on the spins and frequencies. Thus, the partition function without momentum dependence of this Hamiltonian is :

$$Z = \int \mathcal{D}[\bar{c}, c]\mathcal{D}[\bar{f}, f]e^{-S}, \tag{C.4}$$

and the action is:

$$
\begin{aligned}
S &= \int_0^\beta d\tau \sum_\sigma \begin{pmatrix} \bar{c}_\sigma(\tau) & \bar{f}_\sigma(\tau) \end{pmatrix} \begin{pmatrix} \partial_\tau + \epsilon_c & V \\ V & \partial_\tau + \epsilon_f \end{pmatrix} \begin{pmatrix} c_\sigma(\tau) \\ f_\sigma(\tau) \end{pmatrix} \\
&+ \frac{1}{\beta} \iint_0^\beta d\tau_1 d\tau_2 \sum_\sigma \begin{pmatrix} \bar{c}_\sigma(\tau_1) & \bar{f}_\sigma(\tau_1) \end{pmatrix} \begin{pmatrix} h_\sigma^{11}(\tau_1-\tau_2) & h_\sigma^{12}(\tau_1-\tau_2) \\ h_\sigma^{21}(\tau_1-\tau_2) & h_\sigma^{22}(\tau_1-\tau_2) \end{pmatrix} \begin{pmatrix} c_\sigma(\tau_2) \\ f_\sigma(\tau_2) \end{pmatrix} \\
&+ S_{\text{int}}
\end{aligned} \tag{C.5}
$$

If we Fourier transform both c and f, that is,

$$
\begin{aligned}
c_\sigma(\tau) &= \frac{1}{\sqrt{\beta}} \sum_{i\omega_n} c_\sigma(i\omega_n) e^{-i\omega_n \tau} \\
f_\sigma(\tau) &= \frac{1}{\sqrt{\beta}} \sum_{i\omega_n} f_\sigma(i\omega_n) e^{-i\omega_n \tau},
\end{aligned} \tag{C.6}
$$

and assume that the external field has the property that $h(\tau+\beta) = -h(\tau)$, then action becomes:

$$
\begin{aligned}
S &= \sum_{i\omega_n,\sigma} \begin{pmatrix} \bar{c}_\sigma(i\omega_n) & \bar{f}_\sigma(i\omega_n) \end{pmatrix} \begin{pmatrix} -i\omega_n + \epsilon_c & V \\ V & -i\omega_n + \epsilon_f \end{pmatrix} \begin{pmatrix} c_\sigma(i\omega_n) \\ f_\sigma(i\omega_n) \end{pmatrix} \\
&+ \sum_{i\omega_n,\sigma} \begin{pmatrix} \bar{c}_\sigma(i\omega_n) & \bar{f}_\sigma(i\omega_n) \end{pmatrix} \begin{pmatrix} h_\sigma^{11}(i\omega_n) & h_\sigma^{12}(i\omega_n) \\ h_\sigma^{21}(i\omega_n) & h_\sigma^{22}(i\omega_n) \end{pmatrix} \begin{pmatrix} c_\sigma(i\omega_n) \\ f_\sigma(i\omega_n) \end{pmatrix} \\
&+ S_{\text{int}}
\end{aligned} \tag{C.7}
$$

In the derivation of the above formula, use has been made of this integral:

$$
\frac{1}{\beta} \int_0^\beta d\tau_1 \int_0^\beta d\tau_2 e^{i\omega_n \tau_1} e^{-i\omega_m \tau_2} h(\tau_1 - \tau_2) = \delta_{nm} \int_0^\beta d\tau e^{i\omega_n \tau} h(\tau) \tag{C.8}
$$

Differentiation with respect to external field once gives us the one particle Green function as:

$$
\begin{aligned}
-\frac{\delta}{\delta h_\sigma^{\alpha\beta}(i\omega_n)} \log Z &= \frac{1}{Z} \int \mathcal{D}[\bar{c},c]\mathcal{D}[\bar{f},f] e^{-S} \bar{c}_\sigma^\alpha(i\omega_n) c_\sigma^\beta(i\omega_n) \\
&= \langle T \hat{c}_\sigma^{\dagger\alpha} \hat{c}_\sigma^\beta \rangle \\
&= G_\sigma^{\beta\alpha}(i\omega_n)
\end{aligned} \tag{C.9}
$$

Differentiation with respect to external field twice gives us the two-particle Green function as:

$$\begin{aligned} -\frac{\delta}{\delta h^{\gamma\delta}_{\sigma'}(i\omega_{n'})}\frac{\delta \log Z}{\delta h^{\alpha\beta}_{\sigma}(i\omega_n)} &= \frac{\delta G^{\beta\alpha}_{\sigma}(i\omega_n)}{\delta h^{\gamma\delta}_{\sigma'}(i\omega_{n'})} \\ &= -\langle T\hat{c}^{\dagger\gamma}_{\sigma'}\hat{c}^{\delta}_{\sigma'}\hat{c}^{\dagger\alpha}_{\sigma}\hat{c}^{\beta}_{\sigma}\rangle + \langle T\hat{c}^{\dagger\gamma}_{\sigma'}\hat{c}^{\delta}_{\sigma'}\rangle\langle T\hat{c}^{\dagger\alpha}_{\sigma}\hat{c}^{\beta}_{\sigma}\rangle \end{aligned} \tag{C.10}$$

Thus, we see that differentiation of one-particle Green function with respect to external field once will yield the two-particle Green function. Assume the one particle Green function is :

$$G^{-1}_{\sigma}(i\omega_n) = B_{\sigma}(i\omega_n) = i\omega_n\mathbb{I} - \begin{pmatrix} \epsilon_c & V \\ V & \epsilon_f \end{pmatrix} - \Sigma_{\sigma}(i\omega_n) - h_{\sigma}(i\omega_n) \tag{C.11}$$

Taking the functional derivative of one particle Green function with respect to h gives:

$$\begin{aligned} \chi^{\alpha\beta\delta\gamma}(i\omega_n, i\omega_{n'}) &= \frac{\delta G^{\beta\alpha}_{\sigma}(i\omega_n)}{\delta h^{\gamma\delta}_{\sigma'}(i\omega_{n'})} \\ &= \delta_{\sigma\sigma'}\delta_{nn'}G^{\beta\gamma}_{\sigma}(i\omega_n)G^{\delta\alpha}_{\sigma}(i\omega_n) \\ &+ G^{\beta a}_{\sigma}(i\omega_n)G^{b\alpha}_{\sigma}(i\omega_n)\frac{\delta\Sigma^{ab}_{\sigma}(i\omega_n)}{\delta G^{cd}_{\sigma''}(i\omega_{n''})}\frac{\delta G^{cd}_{\sigma''}(i\omega_{n''})}{\delta h^{\gamma\delta}_{\sigma'}(i\omega_{n'})} \end{aligned} \tag{C.12}$$

Two particle Green function appears on both sides of this equation, and thus we get an iterative equation for two particle Green function.

Feynman diagram representation for this equation is shown in Fig (C.1).

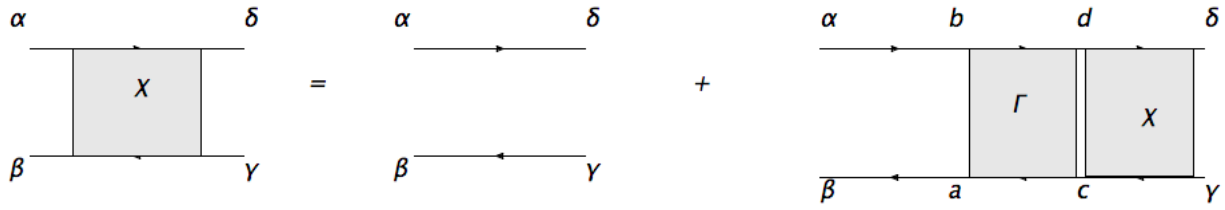

Figure C.1: Feynman diagram representation for Bethe-Salpeter equation.

C.1 Magnetic susceptibility

To study magnetic susceptibility, we should set external field like this:

$$h_{\sigma} = \sigma h \tag{C.13}$$

Then action becomes:

$$
\begin{aligned}
S &= \sum_{i\omega_n,\sigma} \begin{pmatrix} \bar{c}_\sigma(i\omega_n) & \bar{f}_\sigma(i\omega_n) \end{pmatrix} \begin{pmatrix} -i\omega_n+\epsilon_c & V \\ V & -i\omega_n+\epsilon_f \end{pmatrix} \begin{pmatrix} c_\sigma(i\omega_n) \\ f_\sigma(i\omega_n) \end{pmatrix} \\
&+ \sum_{i\omega_n,\sigma} \sigma \begin{pmatrix} \bar{c}_\sigma(i\omega_n) & \bar{f}_\sigma(i\omega_n) \end{pmatrix} \begin{pmatrix} h^{11}(i\omega_n) & h^{12}(i\omega_n) \\ h^{21}(i\omega_n) & h^{22}(i\omega_n) \end{pmatrix} \begin{pmatrix} c_\sigma(i\omega_n) \\ f_\sigma(i\omega_n) \end{pmatrix} \\
&+ S_{\text{int}}
\end{aligned}
\tag{C.14}
$$

Take functional derivative of free energy with respect to external field once, and we get:

$$
-\frac{\delta \log Z}{\delta h^{\alpha\beta}(i\omega_n)} = \sum_\sigma \sigma G_\sigma^{\beta\alpha}(i\omega_n) \tag{C.15}
$$

With a further functional derivative, we get the two-particle Green function as:

$$
\begin{aligned}
-\frac{\delta}{\delta h^{\gamma\delta}(i\omega_{n'})}\frac{\delta \log Z}{\delta h^{\alpha\beta}(i\omega_n)} &= \frac{\delta}{\delta h^{\gamma\delta}(i\omega_{n'})}\sum_\sigma \sigma G_\sigma^\beta(i\omega_n) \\
&= -\sum_{\sigma\sigma'} \sigma\sigma' \langle T\hat{c}_{\sigma'}^{\dagger\gamma}\hat{c}_{\sigma'}^{\delta}\hat{c}_\sigma^{\dagger\alpha}\hat{c}_\sigma^\beta\rangle + \sum_{\sigma'}\sigma'\langle T\hat{c}_{\sigma'}^{\dagger\gamma}\hat{c}_{\sigma'}^\delta\rangle \sum_\sigma \sigma\langle T\hat{c}_\sigma^{\dagger\alpha}\hat{c}_\sigma^\beta\rangle
\end{aligned}
\tag{C.16}
$$

One particle Green function with presence of external magnetic field is:

$$
G_\sigma^{-1}(i\omega_n) = B_\sigma(i\omega_n) = i\omega_n \mathbb{I} - \begin{pmatrix} \epsilon_c & V \\ V & \epsilon_f \end{pmatrix} - \Sigma_\sigma(i\omega_n) - \sigma h(i\omega_n) \tag{C.17}
$$

Differentiation of magnetization with respect to external magnetic field is:

$$
\begin{aligned}
\frac{\delta}{\delta h^{\gamma\delta}(i\omega_{n'})}\sum_\sigma \sigma G_\sigma^{\beta\alpha}(i\omega_n) &= \sum_\sigma \sigma^2 G_\sigma^{\beta\gamma}(i\omega_n)G_\sigma^{\delta\alpha}(i\omega_n)\delta_{nn'} \\
&+ \sum_\sigma \sigma G_\sigma^{\beta a}(i\omega_n)G_\sigma^{b\alpha}(i\omega_n)\frac{\delta\Sigma_\sigma^{ab}(i\omega_n)}{\delta G_{\sigma''}^{cd}(i\omega_{n''})}\frac{\delta G_{\sigma''}^{cd}(i\omega_{n''})}{\delta h^{\gamma\delta}(i\omega_{n'})}
\end{aligned}
\tag{C.18}
$$

It is already shown that

$$
\begin{aligned}
&\frac{\delta}{\delta h^{\gamma\delta}(i\omega_{n'})}\sum_\sigma \sigma G_\sigma^{\beta\alpha}(i\omega_n) \\
&= -\sum_{\sigma\sigma'} \sigma\sigma' \langle T\hat{c}_{\sigma'}^{\dagger\gamma}\hat{c}_{\sigma'}^{\delta}\hat{c}_\sigma^{\dagger\alpha}\hat{c}_\sigma^\beta\rangle + \sum_{\sigma'}\sigma'\langle T\hat{c}_{\sigma'}^{\dagger\gamma}\hat{c}_{\sigma'}^\delta\rangle \sum_\sigma \sigma\langle T\hat{c}_\sigma^{\dagger\alpha}\hat{c}_\sigma^\beta\rangle \\
&= \sum_{\sigma\sigma'} \sigma\sigma' \chi^{\alpha\beta\delta\gamma}_{\sigma'\sigma'\sigma\sigma}(i\omega_n, i\omega_{n'})
\end{aligned}
\tag{C.19}
$$

Therefore, we have the Bethe-Salpeter equation for magnetic susceptibility:

$$\begin{aligned}\frac{\delta\sum_\sigma \sigma G_\sigma^{\beta\alpha}(i\omega_n)}{\delta h^{\gamma\delta}(i\omega_{n'})} &= \sum_{\sigma\sigma'}\sigma\sigma'\chi^{\alpha\beta\delta\gamma}_{\sigma'\sigma'\sigma\sigma}(i\omega_n,i\omega_{n'}) \\ &= \delta_{nn'}\sum_\sigma G_\sigma^{\beta\gamma}(i\omega_n)G_\sigma^{\delta\alpha}(i\omega_n) \\ &+ \sum_{\sigma\sigma'}\sigma G_\sigma^{\beta a}(i\omega_n)G_\sigma^{b\alpha}(i\omega_n)\sigma''\frac{\delta\Sigma_\sigma^{ab}(i\omega_n)}{\delta G^{cd}_{\sigma''}(i\omega_{n''})}\sigma'\sigma''\chi^{dc\delta\gamma}_{\sigma'\sigma'\sigma''\sigma''}(i\omega_{n''},i\omega_{n'})\end{aligned} \tag{C.20}$$

If we define

$$\begin{aligned}\Gamma^{ab}_{cd,z}(i\omega_n,i\omega_{n'}) &\doteq \frac{\delta\Sigma^{ab}_\uparrow(i\omega_n)}{\delta G^{cd}_\downarrow(i\omega_{n'})} - \frac{\delta\Sigma^{ab}_\downarrow(i\omega_n)}{\delta G^{cd}_\uparrow(i\omega_{n'})} \\ \chi_z^{\alpha\beta\delta\gamma}(i\omega_n,i\omega_{n'}) &\doteq \chi^{\alpha\beta\delta\gamma}_{\uparrow\uparrow\uparrow\uparrow}(i\omega_n,i\omega_{n'}) - \chi^{\alpha\beta\delta\gamma}_{\uparrow\uparrow\downarrow\downarrow}(i\omega_n,i\omega_{n'}) \\ \chi_0^{\alpha\beta\delta\gamma}(i\omega_n) &\doteq G^{\beta\gamma}(i\omega_n)G^{\delta\alpha}(i\omega_n),\end{aligned} \tag{C.21}$$

and sum over all spin indices, then we get the Bethe-Salpeter equation for magnetic susceptibility:

$$\chi_z^{\alpha\beta\delta\gamma}(i\omega_n,i\omega_{n'}) = \delta_{nn'}\chi_0^{\alpha\beta\delta\gamma}(i\omega_n) + \chi_0^{\alpha\beta ba}(i\omega_n)\Gamma^{ab}_{cd,z}(i\omega_n,i\omega_{n''})\chi_z^{dc\delta\gamma}(i\omega_{n''},i\omega_{n'}) \tag{C.22}$$

C.2 Charge susceptibility

In the case of charge susceptibility, the external field is independent of spin indices, that is, $h_\sigma = h$. For this external field, action is:

$$\begin{aligned}S &= \sum_{i\omega_n,\sigma}\begin{pmatrix}\bar{c}_\sigma(i\omega_n) & \bar{f}_\sigma(i\omega_n)\end{pmatrix}\begin{pmatrix}-i\omega_n+\epsilon_c & V \\ V & -i\omega_n+\epsilon_f\end{pmatrix}\begin{pmatrix}c_\sigma(i\omega_n) \\ f_\sigma(i\omega_n)\end{pmatrix} \\ &+ \sum_{i\omega_n,\sigma}\begin{pmatrix}\bar{c}_\sigma(i\omega_n) & \bar{f}_\sigma(i\omega_n)\end{pmatrix}\begin{pmatrix}h^{11}(i\omega_n) & h^{12}(i\omega_n) \\ h^{21}(i\omega_n) & h^{22}(i\omega_n)\end{pmatrix}\begin{pmatrix}c_\sigma(i\omega_n) \\ f_\sigma(i\omega_n)\end{pmatrix} \\ &+ S_{\text{int}}\end{aligned} \tag{C.23}$$

Thus, the functional derivative of free energy with respect to external field is:

$$\begin{aligned} -\frac{\delta \log Z}{\delta h^{\alpha\beta}(i\omega_n)} &= \sum_\sigma G_\sigma^{\beta\alpha}(i\omega_n) \\ -\frac{\delta}{\delta h^{\gamma\delta}(i\omega_{n'})}\frac{\delta \log Z}{\delta h^{\alpha\beta}(i\omega_n)} &= \frac{\delta}{\delta h^{\gamma\delta}(i\omega_{n'})}\sum_\sigma G_\sigma^{\beta\alpha}(i\omega_n) \\ &= -\sum_{\sigma\sigma'}\langle T\hat{c}_{\sigma'}^{\dagger\gamma}\hat{c}_{\sigma'}^{\delta}\hat{c}_{\sigma}^{\dagger\alpha}\hat{c}_{\sigma}^{\beta}\rangle + \sum_{\sigma'}\langle T\hat{c}_{\sigma'}^{\dagger\gamma}\hat{c}_{\sigma'}^{\delta}\rangle\sum_\sigma\langle T\hat{c}_{\sigma}^{\dagger\alpha}\hat{c}_{\sigma}^{\beta}\rangle \\ &= \sum_{\sigma\sigma'}\chi^{\alpha\beta\delta\gamma}_{\sigma'\sigma'\sigma\sigma}(i\omega_n, i\omega_{n'}) \end{aligned} \tag{C.24}$$

One particle Green function with presence of external charge field is:

$$G_\sigma^{-1}(i\omega_n) = B_\sigma(i\omega_n) = i\omega_n\mathbb{I} - \begin{pmatrix} \epsilon_c & V \\ V & \epsilon_f \end{pmatrix} - \Sigma_\sigma(i\omega_n) - h(i\omega_n) \tag{C.25}$$

Similarly, we have Bethe-Salpeter equation for charge susceptibility:

$$\begin{aligned} \frac{\delta\sum_\sigma G^{\beta\alpha}(i\omega_n)}{\delta h^{\gamma\delta}(i\omega_{n'})} &= \sum_{\sigma\sigma'}\chi^{\alpha\beta\delta\gamma}_{\sigma'\sigma'\sigma\sigma}(i\omega_n, i\omega_{n'}) \\ &= \delta_{nn'}\sum_\sigma G_\sigma^{\beta\gamma}(i\omega_n)G_\sigma^{\delta\alpha}(i\omega_n) \\ &= \sum_{\sigma\sigma'} G_\sigma^{\beta a}(i\omega_n)G_\sigma^{b\alpha}(i\omega_n)\frac{\delta\Sigma_\sigma^{ab}(i\omega_n)}{\delta G^{cd}_{\sigma''}(i\omega_{n''})}\chi^{dc\delta\gamma}_{\sigma'\sigma'\sigma''\sigma''}(i\omega_{n''}, i\omega_{n'}) \end{aligned} \tag{C.26}$$

Define:

$$\begin{aligned} \chi_C^{\alpha\beta\delta\gamma}(i\omega_n, i\omega_{n'}) &\doteq \chi^{\alpha\beta\delta\gamma}_{\uparrow\uparrow\uparrow\uparrow}(i\omega_n, i\omega_{n'}) + \chi^{\alpha\beta\delta\gamma}_{\uparrow\uparrow\downarrow\downarrow}(i\omega_n, i\omega_{n'}) \\ \Gamma^{ab}_{cd,C}(i\omega_n, i\omega_{n'}) &\doteq \frac{\delta\Sigma^{ab}_\uparrow(i\omega_n)}{\delta G^{cd}_\uparrow(i\omega_{n'})} + \frac{\delta\Sigma^{ab}_\downarrow(i\omega_n)}{\delta G^{cd}_\uparrow(i\omega_{n'})} \end{aligned} \tag{C.27}$$

Then Bethe-Salpeter equation for charge susceptibility in its final form is:

$$\chi_C^{\alpha\beta\delta\gamma}(i\omega_n, i\omega_{n'}) = \delta_{nn'}\chi_0^{\alpha\beta\delta\gamma}(i\omega_n) + \chi_0^{\alpha\beta ba}(i\omega_n)\Gamma^{ab}_{cd,C}(i\omega_n, i\omega_{n''})\chi_C^{dc\delta\gamma}(i\omega_{n''}, i\omega_{n'}) \tag{C.28}$$

Vita

Enzhi Li was born in a small village in Sheqi, Henan province in China. With the support, guidance and encouragements of his parents, he went to Nanjing University of Astronautics and Aeronautics in 2005, and went to LSU to pursue his doctorate degree in physics in 2011.